

INFLUENCE OF IRRIGATION ON SOIL MOISTURE AND EVAPORATION BASED ON SENTINEL-1 BACKSCATTER OBSERVATIONS AND AN EVAPORATION RETRIEVAL MODEL

Number of words: 23.217

Baris Oztas

Studentnumber: 02205682

Academic promoters: Prof. dr. Diego Miralles & Prof. dr. Davide Cammarano

Master's Dissertation submitted to Ghent University in partial fulfilment of the requirements for the degree of International Master of Science in Soils and Global Change.

Academic Year: 2023 — 2024

Copyright Clause

The author and the promoters give the permission to use this master dissertation for consultation and to copy parts of it for personal use. Every other use is subject to the copyright laws, more specifically the source must be extensively stated when using from this thesis.

Ghent, June 7, 2024

The promoters:

The author:

Prof. dr. Diego Miralles

Baris Oztas

Prof. dr. Davide Cammarano

Acknowledgements

First and foremost, I would like to thank my promoter, Diego Miralles, for giving me the opportunity to join the amazing H-CEL (Hydro-Climate Extremes Lab) research group during my Master's studies. I also thank Davide Cammarano for accepting the role of co-promoter for my thesis. My deepest appreciation goes to Oscar Manuel Baez-Villanueva for being not only a perfect supervisor but also a friend. I cannot stress enough how deeply indebted I am to Hans Lievens for his unofficial yet invaluable supervision. Their expertise, willingness to always make time for my endless questions, even at very short notice, and all the critiques and questions they raised were invaluable. This work would not have been possible without their support and guidance. I also extend my sincere thanks to Olivier Bonte, Irina Petrova, and Akash Koppa for all the discussions and perspectives they provided during my research. It was an amazing experience to get to know and work with you.

Next, I extend my heartfelt thanks to my IMSOGLO classmates Mete, Carmen, Gaël, Malaika, and Gaby for being incredible friends over the past two years. Starting a new life in a new country, far from friends and family, was challenging, but your companionship made everything much easier. I feel incredibly fortunate to have met such wonderful people like you. Musa, Kamil, and Siamak, I cannot explain how grateful I am for your friendship, support, and the times we spent together climbing in the mountains, which were the most beautiful moments of my life without a doubt. I must also express my heartfelt gratitude and love to my dear friends Cagatay, Ilgin, Semin, and Yusuf (aka *Numerical Guys*) for their friendship over the last seven years. Despite the time and distance that have separated us, I continue to feel the strength of our bond and friendship. I eagerly look forward to the day when we can reunite and share a glass of raki together once more. I also want to extend my thanks to my former housemates, Mumtaz and Japon. I am grateful not only for the wonderful times we shared at Daire 5, 1 and 27 but also for the video calls over the past two years that have kept me sane. I am eagerly looking forward to reuniting and having *fun* like the old days.

Finally, and most importantly, I would like to thank my mother, Dilek Öztaş, and my sister, Esin Karadağ, for their endless support and encouragement. Without your love and belief in me, this journey would not have been possible. I must express my deepest gratitude to my father, Hasan Öztaş. The strength I have drawn from knowing you will always stand by me and support me is beyond words. I am incredibly fortunate to have you as my father; none of this would have been possible without you. İyi ki ailemsiniz!

Barış Öztaş – Ghent, June 2, 2024

List of Acronyms

AMSR-E	The Advanced Microwave Scanning Radiometer-Earth Observation System
AMSR2	The Advanced Microwave Scanning Radiometer 2
ASCAT	Advanced Scatterometer
AVHRR	Advanced Very High Resolution Radiometer
CCI	Climate Change Initiative
CORINE	Coordination of Information on the Environment
DA	data assimilation
dB	decibel
DGU	Dynamic Gaussian Upscaling
DISPATCH	DISaggregation based on a Physical And Theoretical scale CHange
DTE	Digital Twin Earth
E	evaporation
EnKF	Ensemble Kalman Filter
ERA5-Land	ECMWF ReAnalysis v5-Land
ERS-1/2	European Remote Sensing 1/2
ESA	European Space Agency
ESM	Earth System Model
FAO	The Food and Agriculture Organization of the United Nations
FWHM	Full Width at Half Maximum
GLC2000	Global Land Cover 2000
GLEAM	Global Land Evaporation Amsterdam Model
GRACE	The Gravity Recovery and Climate Experiment
IPE	Instituto Pirenaico de Ecologia
IQR	interquartile range
ISMN	International Soil Moisture Network
IW	Interferometric Wide
LAI	leaf area index
LPRM	Land Parameter Retrieval Model
LSM	land surface model
MERIS	The Medium Resolution Imaging Spectrometer
MERRA-2	The Modern-Era Retrospective analysis for Research and Applications - version 2
MODIS	Moderate Resolution Imaging Spectroradiometer

MSE	Mean Square Error
MW	microwave
NDVI	normalized difference vegetation index
OL	Open Loop
R	Pearson's correlation coefficient
RCM	Regional Climate Model
RMSE	Root Mean Square Error
RS	remote sensing
RT1	First-Order Radiative Transfer Model
RTM	radiative transfer model
SAR	synthetic aperture radar
SM	soil moisture
SMAP	Soil Moisture Active Passive
SMAP/S-1	Soil Moisture Active Passive/Sentinel-1
SMOS	Soil Moisture and Ocean Salinity
SNAP	Sentinel Application Platform
SWE	snow water equivalent
TB	brightness temperature
TIR	thermal infrared
TMI	TRMM Microwave Imager
TRF	Trust Region Reflective
TRMM	The Tropical Rainfall Measuring Mission
TU Wien	Vienna University of Technology
USGS	United States Geological Survey
VIS-NIR	visible and near-infrared
VOD	vegetation optical depth
VV	Vertical-Vertical
WCM	Water Cloud Model
XMS-CAT	Institut cartografic i Geologic de Catalunya

Contents

Copyright Clause	i
Acknowledgements	ii
List of Acronyms	iii
Contents	vi
List of Figures	viii
List of Tables	ix
Abstract	x
1 Introduction	1
1.1 Objectives of the research	3
2 Literature review	4
2.1 Soil moisture	4
2.1.1 Soil moisture estimation and measurements	4
2.1.2 Soil moisture from space	5
2.2 Evaporation	7
2.2.1 Evaporation estimation and measurements	7
2.2.2 Evaporation from space	9
2.3 Irrigation estimation and measurement	10
2.3.1 Irrigation from space	10
2.3.2 Data assimilation and irrigation	13
3 Materials and methods	16
3.1 Study area – Ebro Basin	16
3.2 Global Land Evaporation Amsterdam Model	18
3.2.1 Interception module	19
3.2.2 Soil water balance module	19
3.2.3 Potential evaporation module	20
3.2.4 Stress module	21
3.3 Sentinel-1 SAR backscatter	23
3.4 Data assimilation	25
3.4.1 Forward operator	25
3.4.2 Calibration of Water Cloud Model	26
3.4.3 Ensemble Kalman Filter	28
3.4.4 Ensemble generation	30
3.5 Experiment setups	30
4 Results and discussion	32

4.1	Evaluation of the forward operator	32
4.1.1	Calibration of Water Cloud Model	32
4.1.2	Backscatter simulations	35
4.2	Evaluation of data assimilation impact on soil moisture and evaporation estimates	38
4.2.1	Basin-scale soil moisture and evaporation simulations	39
4.2.2	In-situ comparison	47
5	Conclusion and future research perspectives	49
5.1	Conclusion	49
5.2	Future research perspectives	50
	References	52
A	Appendix A: An example time series from a forest grid-cell	70
B	Appendix B: Anomalies of DA-A with respect to OL run	70

List of Figures

3.1	Ebro Basin boundaries, irrigated areas, Ebro river, ISMN sites, and digital elevation map. Long-term (2016–2021) mean annual precipitation and temperature values over Ebro Basin computed from forcing dataset is shown in subplots. The size of the ISMN site symbols is directly proportional to the length of the data record.	17
3.2	Ebro Basin CORINE land cover types.	18
3.3	Overview of GLEAM modules and their respective forcings. Modified from Martens et al. (2017).	20
3.4	Stress function implemented in GLEAM for vegetated fractions. High range of VOD (left) [0.27-0.47]; Small range VOD (right) [0.38-0.40]. Retrieved from Martens et al. (2017).	21
3.5	Resampling of Sentinel-1 images with simple bilinear resampling and DGU method highlighting polluted pixels over an agricultural area in England. © IEEE. Modified and reprinted from Bauer-Marschallinger et al. (2019).	24
3.6	FAO Phenology Start and End of Season datasets used to flag irrigated areas with respect to their growing season. Irrigated areas are highlighted.	28
4.1	Fitted WCM parameter boxplots based on land cover type. The boxes represent the first (Q1) and third (Q3) quartiles, while the solid line within the box represents the median (second quartile; Q2). The whiskers of the boxplots represent values within the interquartile range (IQR; $Q3 - Q1$) between $Q1 - 1.5IQR$ and $Q3 + 1.5IQR$. Outliers are not shown. The number of grid-cell belonging to each land cover type is indicated at the top of the boxplots.	32
4.2	Fitted WCM parameters over the Ebro Basin. Highlighted areas represent irrigated croplands. Case B is shown for the highlighted areas.	33
4.3	Difference in the fitted WCM parameters. The differences in parameters are presented as Case B minus Case A.	35
4.4	(left) Temporal correlation and RMSE of simulated backscatter over the Ebro Basin for DA-B. (right) The difference in performance between two DA experiments. Irrigated areas are highlighted.	36
4.5	Boxplots of temporal correlation and RMSE between simulated and observed backscatter by land cover type. The number of grid-cells belonging to each land cover type is indicated at the top of the boxplots.	37
4.6	Long-term mean Sentinel-1 observations and DA-B simulations over the Ebro Basin, as well as the difference between them. The difference between simulated backscatter from the two DA experiments is also provided.	38
4.7	Spatial distribution of ensemble standard deviations averaged over the period 2016–2021 for DA-B. Irrigated areas are highlighted.	39
4.8	(top) Long-term (2016–2021) seasonal E_p estimates over the Ebro Basin as derived from GLEAM, (bottom) boxplots of long-term (2016–2021) seasonal evaporative demand estimates categorized by land cover type.	40

4.9	(left) Long-term (2016–2021) mean SM and total annual E estimates over the Ebro Basin from GLEAM OL run, (right) long-term (2016–2021) anomalies of DA-B with respect to Open Loop (OL) run. Irrigated areas are highlighted. . . .	41
4.10	Simulated GLEAM total annual E boxplots from different experiments based on land cover type.	41
4.11	DA impact on SM and E estimates with respect to OL. Outliers are shown. The number of grid-cells that belongs to each land cover is indicated on top of the boxplots.	42
4.12	(top) MAM season, (bottom) JJA season, (left) GLEAM OL SM and E estimates, (right) DA-B anomalies with respect OL run. Irrigated areas are highlighted. .	44
4.13	DA and OL difference on SM and E estimates during growing season over irrigated areas.	45
4.14	Example time series (2019–2021) from an irrigated grid-cell. (top) LAI observations, (middle) OL and DA SM and daily E estimates as well as the the simulated and observed backscatter, (bottom) daily SM increments to the GLEAM top layer soil moisture. Selected grid-cell longitude: -1.21 latitude: 41.85	45
4.15	Relationship of SM and LAI with simulated backscatter based on different WCM parameterization. Parameters are from the same grid-cell in Figure 4.14. Selected grid-cell longitude: -1.21 latitude: 41.85	46
4.16	Example time series (2019–2021) from an irrigated grid-cell. (top) LAI observations, (middle) OL and DA SM and daily E estimates as well as the the simulated and observed backscatter, (bottom) daily SM increments to the GLEAM top layer soil moisture. Selected grid-cell longitude: -1.45 latitude: 41.96	46
4.17	Relationship of SM and LAI with simulated backscatter based on different WCM parameterization. Parameters are from the same grid-cell in Figure 4.16. Selected grid-cell longitude: -1.45 latitude: 41.96	47
4.18	Temporal correlation between daily <i>in-situ</i> SM and GLEAM first layer SM. . .	48
A.1	Example time series (2016–2021) from a forest grid-cell. (top) LAI observations, (middle) OL and DA SM and daily E estimates as well as the the simulated and observed backscatter, (bottom) daily SM increments to the GLEAM top layer soil moisture. Selected grid-cell longitude: -0.81 latitude: 42.32. WCM Parameters: $A=0.00$, $B=0.00$, $C=-10.52$ dB, $D=4.286$ dB/m ³ m ⁻³	70
B.1	(left) Long-term (2016–2021) mean SM and total annual E estimates over the Ebro Basin from GLEAM OL run, (right) long-term (2016–2021) anomalies of DA-A with respect to OL run. Irrigated areas are highlighted.	70

List of Tables

2.1	Specifications of global SM retrieval products.	7
3.1	<i>In-situ</i> soil moisture sites with their respective land cover and data availability.	19
3.2	GLEAM forcing datasets and their characteristics.	22
3.3	Water Cloud Model calibration parameter upper, lower boundary and initial values.	27
3.4	Forcing and state variable perturbation characteristics.	30
4.1	Detailed comparison of backscatter simulations over different land cover types.	37
4.2	Detailed comparison of the observation forecast variability for different land covers.	38
4.3	Temporal correlation of daily <i>in-situ</i> SM with OL and DA experiment SM estimates.	47

Abstract

Irrigation stands out as a primary driver influencing water dynamics over agricultural regions. Satellite observations only indirectly relate to irrigation, and disentangling irrigation's effects on transpiration and soil moisture (SM) from space is challenging. This study addresses these challenges with two primary objectives: (1) to enable forward simulation of Sentinel-1 backscatter to be used in data assimilation (DA) and (2) to capture the influences of irrigation on SM and evaporation (E) through DA.

The calibration results of the forward operator and forward simulations of Sentinel-1 backscatter revealed that vegetation significantly influences scattering mechanisms over cultivated areas. Comparing Sentinel-1 backscatter observations and forward simulations showed satisfactory performance (mean $R = 0.618$, mean RMSE = 0.617 dB). For the second objective, DA impacts were analyzed, highlighting seasonal differences in E and SM estimates. During summer, DA increased water availability over most of the region that leads to increase in seasonal E, while the impact was minimal in other seasons. In the Ebro Basin, anthropogenic-management practices (i.e., inter and intra-annual crop dynamics) complicated backscatter dynamics, which could not be fully explained with a single WCM parameter set per grid-cell. Despite these challenges, data assimilation of Sentinel-1 data improved soil moisture estimates across various land cover types (average daily SM correlation $R = 0.778$, 13 *in-situ* stations), with a modest overall improvement (mean $\Delta R = +0.005$).

The resulting 1km daily SM and E GLEAM dataset has the potential to be used for water and agricultural management applications. Conclusions have also highlighted the ongoing challenges and future research directions in DA over irrigated areas.

ChatGPT is utilized for improving Python codes (i.e., improving the codes that produced figures), \LaTeX formatting, and English language and grammar of the dissertation.

1 Introduction

Throughout history, agriculture has played a crucial role in shaping society and fostering the development of civilization as we understand it today. It forms the basis of our food supply and ensures nutrition for the global population. Currently, agricultural land occupies almost one-third of the global land area, excluding Antarctica and inland waters, amounting to 4.8 billion hectares (FAO, 2023). With the world population expected to reach 9.7 billion by 2050, along with rising consumption rates, agriculture will face significant challenges in the 21st century (United Nations, 2022). Although the population is projected to increase by around 20%, food demand is expected to double by 2050 (Tilman et al., 2002).

Rainfed agriculture is the dominant agricultural production system worldwide, accounting for 80% of the total cultivated area, yet irrigated agriculture supplies 40% of global food production (Brocca et al., 2018; FAO, 2022). Therefore, irrigated agriculture is essential for ensuring food security and supporting economic development, particularly in arid and semi-arid regions (FAO, 2022). For instance, the Mediterranean region, characterized by agriculture as a significant portion of its overall production and employment structure, illustrates the importance of irrigation (Piecuch & Paluch, 2016).

Currently, irrigated agriculture is responsible for 70% of global freshwater withdrawal (FAO, 2018b). Because of this, irrigated agriculture, particularly in semi-arid and arid regions, exerts substantial pressure on water resources and is vulnerable to the impacts of climate change (Duarte et al., 2021). Studies have shown that poor water management practices, such as uncontrolled expansion of irrigated agriculture and increased water abstraction in arid and semi-arid regions, can significantly affect water availability, groundwater level, river discharge, environmental degradation, and biodiversity (Duarte et al., 2021; Jeppesen et al., 2020; Yılmaz et al., 2021).

Due to anthropogenic climate change, the number of warm days and nights, as well as the frequency of extreme heat have doubled since 1970s (Barriopedro et al., 2023). Additionally, the Mediterranean region is recognized as a hot spot for climate change, where the occurrence of heat extremes is expected to substantially increase in the future (Bağçacı et al., 2021; Zachariadis, 2016). Changes in precipitation patterns and rising water scarcity over the next decades will further constrain water availability for irrigated agriculture, potentially impacting food production (Fader et al., 2016; Iglesias et al., 2011; IPCC, 2014).

Given these challenges, it is imperative to adopt better water management strategies to quantify risks and develop proactive mitigation strategies related to the negative impacts of climate change on water resources (Elnashar & Elyamany, 2023). Fully characterizing the hydrological cycle over irrigated regions is essential for better managing water for agricultural purposes and evaluating the impact of irrigation on soil moisture (SM) and evaporation (E) dynamics (Alter et al., 2015; Brocca et al., 2018; Dari et al., 2022). Despite irrigation being a primary factor influencing the hydrological cycle in anthropogenic regions, irrigation practices are rarely monitored, and the precise amount and timing of irrigation are generally unknown.

Monitoring irrigation using in-situ observations over large domains for extended periods remains challenging due to the technical constraints of deploying monitoring systems on a large scale. Due to these constraints, there is a lack of comprehensive in-situ data at relevant temporal and spatial scales (Brocca et al., 2018). Monitoring irrigation in time and space using remote sensing (RS) from space also faces constraints as satellite observations cannot directly estimate irrigation amounts. Although combining RS data with *in-situ* observations could improve monitoring efforts over large areas and offer a complementary approach, this approach is also hindered by the scarcity of in-situ data, limiting the evaluation of the reliability and accuracy of remote sensing products (Brocca et al., 2018; Dari et al., 2023).

Historically, satellite observations have been employed to monitor key hydrological variables such as SM and E. While SM can be effectively monitored using microwave (MW) sensors at high temporal resolution (Dorigo et al., 2021a; Tang et al., 2009), E cannot be directly sensed using RS sensors because it lacks a distinct electromagnetic signature (Holmes, 2019). Thus, E retrieval algorithms often rely on observations of meteorological and biophysical variables to derive E estimates, such as in the case of Global Land Evaporation Amsterdam Model (GLEAM) (Martens et al., 2017; Miralles et al., 2011), which is used in this thesis.

Until now, coarse-scale MW sensors such as Soil Moisture Active Passive (SMAP), Soil Moisture and Ocean Salinity (SMOS), and Advanced Scatterometer (ASCAT) have demonstrated their ability to observe temporal SM dynamics globally in a consistent way; however, they lack the spatial resolution needed to disentangle the irrigation practices that often occur at finer resolutions (Bauer-Marschallinger et al., 2019). Similar to SM retrievals, E retrieval products and algorithms also show potential for use in measuring global E. However, most of the current global E retrieval products do not consider the influence of irrigation due to their coarse spatial resolution, limiting their suitability for agricultural applications and water management practices over anthropogenic basins (Jahromi et al., 2022).

Sentinel-1 mission stands out as a valuable satellite constellation for monitoring hydrological cycles with greater precision due to its high-resolution capabilities. Since the launch of the first satellite in 2014, the Sentinel-1 mission has been effectively utilized for tracking small-scale hydrological phenomena such as irrigation and floods, providing critical data for these studies (Gruber et al., 2013; Twele et al., 2016; Uddin et al., 2019; Wagner et al., 2009). Recent studies have employed high-resolution Sentinel-1 data in the context of irrigation in two ways: first, through SM retrievals, and second, by assimilating Sentinel-1 backscatter into land surface models (LSMs) to improve their estimates. Studies by Bauer-Marschallinger et al. (2019), Dari et al. (2023), Jalilvand et al. (2021), Quast et al. (2023), and Zappa et al. (2021, 2022) have shown that Sentinel-1 SM retrievals can capture SM variability due to irrigation practices over agricultural domains. On the other hand, recent studies have also highlighted the potential of assimilating Sentinel-1 backscatter data for quantifying irrigation and its influence on SM and vegetation state variables (e.g., leaf area index (LAI)) using several data assimilation (DA) techniques such as Ensemble Kalman Filter (EnKF) and particle filter approaches (Modanesi et al., 2021, 2022; Ouaadi et al., 2021).

At coarser scales previous studies have shown the potential of assimilating direct observations of active radar backscatter from ASCAT and passive brightness temperature (TB) from SMOS into GLEAM for improving the estimates of E and SM globally (Lievens et al., 2017a; Martens et al., 2016). Moreover, a recent study by Rains et al. (2022) has also shown the potential of assimilating Sentinel-1 backscatter into GLEAM at the point scale to improve SM estimates. The recent availability of high-resolution Sentinel-1 observations alongside other high-resolution RS datasets like net radiation (Rains et al., 2024), land surface temperature, and precipitation, presents a unique opportunity to address the limitations of capturing the influence of irrigation on SM and E estimates using GLEAM.

1.1 Objectives of the research

Given the importance of addressing the limitations of capturing the influence of irrigation on SM and E estimates through modeling and RS, this study has two key objectives: (1) to enable forward simulation of Sentinel-1 backscatter by coupling radiative transfer model (RTM), GLEAM, and LAI observations, and (2) to develop a DA method that updates SM estimates to account for irrigation and provide the associated SM and E uncertainties. Specifically, these objectives will be achieved through utilizing the Water Cloud Model (WCM) as the forward operator and EnKF as the DA approach. By achieving these objectives, this study will generate high-resolution (1km) daily SM and E estimates over the Ebro Basin in Spain, addressing the knowledge gaps regarding the influence of irrigation on SM and E estimates over anthropogenic basins, thereby making the results more useful for agricultural and water management applications.

2 Literature review

This section presents the literature review to highlight the focus of the master’s dissertation and the path towards fulfilling the goal of developing a DA framework to account for irrigation in the SM and E estimates of GLEAM. Sections 2.1 and 2.2 address the theory, specifications, advantages, and disadvantages of global SM and E retrieval products. Moreover, Section 2.3 discusses different approaches regarding the quantification of irrigation from space, the determination of the spatial extent of irrigated areas, and how data from RS have been utilized in the context of DA, demonstrating their advantages for improving estimates of key hydrological variables.

2.1 Soil moisture

In this section, a comparison between active and passive MW sensors and their respective frequency bands will be conducted, as shown in Table 2.1. Examining these products and their respective advantages and disadvantages provides a context for understanding the efficiency and limitations of different sensors for monitoring SM. Compared to previous MW satellite missions, Sentinel-1 observations, due to the nature of the Sentinel-1 sensor, are more sensitive to surface geometry and vegetated conditions. This is a crucial consideration when assimilating Sentinel-1 MW observations, as changes in surface conditions and vegetation must be accounted for to accurately update SM estimates. By examining the SM retrieval products, their methodologies, and their performance, this section aims to gain a comprehensive understanding of how Sentinel-1 backscatter data can be effectively utilized and integrated into GLEAM. This background knowledge will help identify potential challenges and advantages in using Sentinel-1, guiding the development of more accurate and reliable SM assimilation techniques.

2.1.1 Soil moisture estimation and measurements

SM refers to the water stored in the unsaturated part of the soil, typically measured in terms of volume or weight. Despite constituting a very small portion ($<0.05\%$) of the total amount of global fresh water, it is one of the key hydrological variables that controls the movement of water among various Earth system components such as land, atmosphere, and vegetation (Dorigo et al., 2021a; Li et al., 2021; Shiklomanov, 1998). It also plays a crucial role in physical and biological processes such as rainfall partitioning, water storage, and terrestrial E (Kerr, 2007; Martens et al., 2018b; Qing et al., 2023). For instance, SM has a substantial role in driving ecosystem dynamics through plant-available water, highlighting its relevance in the terrestrial carbon cycle (Dorigo et al., 2017). In addition, recent studies have highlighted the feedback between SM and the atmosphere, indicating that dry soils can contribute to increased heat accumulation, leading to the development of extreme air temperatures (Miralles et al., 2014; Quesada et al., 2012).

Therefore, knowledge of SM at relevant spatio-temporal scales is fundamental for water man-

agement and various climate-related research sectors (e.g., validations of Earth System Models (ESMs) and Regional Climate Models (RCMs), identifying the role of SM in temperature variability and heatwaves, etc.) (Dorigo et al., 2017). The most conventional approach for measuring soil water content relies on gravimetry; i.e., soil weight loss due to the removal of water with heat. This method is precise; however, it is not possible to derive temporally continuous measurements at larger scales (Gardner, 2018; Mane et al., 2024).

On the other hand, SM has also been monitored using ground-based sensors based on the principle of dielectric contrast between liquid water and soil at the field scale for better temporal coverage compared to gravimetric methods (Yang, 2019). Another method to measure SM content is utilizing naturally occurring cosmic rays, which interact with soil particles through neutrons, with wetter soil resulting in more neutron absorption or slowing (Kodama et al., 1985). This method enables the determination of average SM over a horizontal footprint of hundreds of meters to a depth of tens of centimeters (Zreda et al., 2012). Despite the availability of large-scale *in-situ* SM networks such as International Soil Moisture Network (ISMN), OzNet, FLUXNET, and AmeriFlux, they are sparsely distributed, lacking adequate spatial and temporal coverage and consistency for detailed Earth system assessments (Dorigo et al., 2017, 2021b; Pastorello et al., 2020; Smith et al., 2012). Therefore, RS-based SM monitoring is useful to mitigate the limitations of *in-situ* monitoring (Dorigo et al., 2017).

2.1.2 Soil moisture from space

As a result, scientists have turned to satellites for global SM monitoring, primarily utilizing different parts of the electromagnetic spectrum: MW, as well as the visible and near-infrared (VIS-NIR) and thermal infrared (TIR) bands. Despite recent advances in SM retrievals derived from VIS-NIR and TIR, these methods are affected by atmospheric conditions like cloud cover and vegetation cover opacity and only provide information on a very thin layer of the air-soil interface. In contrast, MW sensors provide information at a depth of 5–10 cm (Ambrosone et al., 2020; Babaeian et al., 2018; Sadeghi et al., 2017; Ulaby, 1974). Moreover, it has been shown that MW observations are more sensitive to water content compared to VIS-NIR and TIR observations (Li et al., 2021). Analogous to ground-based gravimetric measurements, time-variable gravity measurements from satellites, such as the The Gravity Recovery and Climate Experiment (GRACE) mission, can also be used to estimate temporal changes in land water storage, which can then be related to SM (Abelen & Seitz, 2013). However, accurate quantification of mass variations has been shown to be challenging due to the coarse spatial resolution (~300 km) and limited accuracy (Chen et al., 2022). Therefore, in this section, emphasis will be placed on global passive and active MW SM retrieval products, discussing their theories, specifications, advantages, and disadvantages.

MW sensors are categorized into two types: passive radiometers and active radars. Passive MW radiometers can measure the TB emitted from the soil surface, which is the product of its temperature and emissivity (Schmugge et al., 1974). Active radars transmit their own energy and measure the reflected backscatter, which is governed by the surface geometry and dielectric properties of the observed surface (Ulaby, 1974). As the dielectric properties of soil are

highly dependent on SM due to the difference between the dielectric constant of water (~ 80) and dry soil ($\sim 3-4$), SM influences the emitted TB and reflected backscatter of the observed soil (Schmugge, 1978). Since SM variations can affect the soil dielectric conductivity and thus the emitted TB and backscatter from the soil, MW observations can be used to retrieve SM information.

Currently, arguably, the most frequently used SM retrieval products from TB observations utilize the Land Parameter Retrieval Model (LPRM) algorithm (Meesters et al., 2005; Owe et al., 2001), while products from backscatter observations mainly utilize the Vienna University of Technology (TU Wien) Change Detection algorithm (Wagner et al., 1999). However, it should be noted that there are many others apart from these two models. LPRM is a method built upon RTM (i.e., model to convert geophysical variables into satellite observed radiance) for simulating brightness temperatures over vegetation-covered fields (Mo et al., 1982). The TU Wien Change Detection method attributes changes in the observed backscatter to changes in SM, assuming that changes in vegetation and surface roughness conditions are negligible between two consecutive observations (Bauer-Marschallinger et al., 2019).

LPRM has proven its capability to retrieve SM estimates globally from TB observations from TRMM Microwave Imager (TMI) (de Jeu, 2013c), Windsat/Coriolis (de Jeu, 2014), The Advanced Microwave Scanning Radiometer-Earth Observation System (AMSR-E) and The Advanced Microwave Scanning Radiometer 2 (AMSR2) (de Jeu, 2013a, 2013b). These products' specifications are summarized in Table 2.1.

Another difference between active and passive sensors is that active sensors are highly subjected to backscatter variations due to their higher sensitivity to the geometric distribution of scatterers (e.g., soil surface, leaves, vegetation); therefore, they are more affected by the presence of vegetation canopy compared to passive sensors (Kerr, 2007). While passive sensors are also affected by vegetation properties, they may not be as susceptible to changes in vegetation structure as active sensors because they rely on natural radiation rather than geometry (Kerr, 2007).

As can be seen in Table 2.1, several bands, including L-band (0.5–1.5 GHz), C-band (4–8 GHz), and X-band (8–12 GHz), have been utilized to retrieve SM information from satellite sensors. However, preliminary studies during ground and airborne measurements have indicated that L-band proves to be the most efficient radiometry band for retrieving SM (Schmugge et al., 1988). This is because the sensitivity of C- and X-bands to changes in SM diminishes at a maximum vegetation water content of 1.5 kg/m^2 compared to limit of 5 kg/m^2 of L-band (Li et al., 2021). However, as depicted in Table 2.1, early missions extensively employed C- and X-bands until SMOS became the first satellite with passive L-band. This was due to the technical limitations that hindered the construction of an antenna of approximately 8 meters in diameter to achieve the required spatial resolution from an altitude of 750km (Kerr, 2007).

Table 2.1: Specifications of global SM retrieval products.

Name	Type	Band	Spatial resolution	Data availability	Reference
The Tropical Rainfall Measuring Mission (TRMM)/TMI	Passive	X	45km	1997–2015	de Jeu (2013c)
Windsat/Coriolis	Passive	C–X–Ku–K	25km	2003–2012	de Jeu (2014)
AMSR-E	Passive	C–X	56km & 38km	2002–2011	de Jeu (2013a)
AMSR2	Passive	C–X	31km	2012–present	de Jeu (2013b)
SMOS	Passive	L	30km	2010–present	European Space Agency (2009)
SMAP	Passive	L	36km	2015–present	ONeill et al. (2023)
European Remote Sensing 1/2 (ERS-1/2)	Active	C	25km	1991–2011	European Space Agency (1995)
SMAP	Active	C	3km	2015–2015	Kim et al. (2016)
Soil Moisture Active Passive/Sentinel-1 (SMAP/S-1)	Active-Passive	C–L	3km	2015–present	Das et al. (2019)
ASCAT	Active	C	12.5km	2007–present	Wagner et al. (2013)

2.2 Evaporation

2.2.1 Evaporation estimation and measurements

Land surface E, or terrestrial E, is the transition of liquid water into vapor from the Earth’s surface into the atmosphere over a given time period (Brutsaert, 1982). This process occurs in three main ways: E from bare soil or open water, transpiration from plant leaves, and rainfall interception by the vegetation canopy. Bare soil E, open water E, and rainfall interception are primarily driven by meteorological conditions and water availability, constituting approximately 25% of global land surface E flux (Miralles et al., 2010). Transpiration from plant leaves is also regulated by meteorological conditions and water availability, while also being influenced by biophysical processes within leaves, accounting for the remaining 75% of global land surface E flux (Holmes, 2019). The energy required for these vaporization processes is referred to as "latent heat of E".

The Earth receives its energy from the Sun in the form of shortwave radiation. As this energy is transmitted through the atmosphere, aerosols, gases, and clouds absorb and scatter it, changing the atmospheric temperature and its emission of long-wave radiation in all directions (Rains et al., 2024). Furthermore, the shortwave radiation reaching the Earth’s surface is again reflected by the albedo effect, depending on the type of surface (Kiehl & Trenberth,

1997). Consequently, the Earth's surface also emits radiation in the form of long-wave radiation, as described by the Stefan-Boltzmann law. Net radiation, R_n , is essentially the difference between the absorbed shortwave radiation and the emitted long-wave radiation (Brutsaert, 1982), which can be written as:

$$R_n = R_s (1 - \alpha_s) + \epsilon_s R_{ld} - R_{lu} \quad (1)$$

where R_s is the incoming short-wave radiation, α_s the albedo of the surface, R_{ld} the downward long-wave (i.e., atmospheric radiation), ϵ_s the emissivity of the surface and R_{lu} the upward long-wave radiation. This R_n is partitioned between convection of sensible heat H , evaporation of water $L_e E$, and downward conduction of heat into soil G :

$$R_n = L_e E + H + G \quad (2)$$

where L_e is the latent heat of vaporization. This partitioning of energy is a primary mechanism that influences atmospheric behavior (Brutsaert, 1982).

Although "bare soil evaporation" and "transpiration" are often combined under the term *evapotranspiration* to describe total latent heat flux –first described by Thornthwaite (1948)– Brutsaert (1982), Miralles et al. (2020), and Savenije (2004) argued that the term *evaporation* can adequately describe all vaporization processes, while *evapotranspiration* often ambiguously combines different processes (evaporation, transpiration, interception) that could lead to inconclusiveness and inconsistencies. Thus, the term *evaporation* will be used in this thesis to describe all latent heat flux over land.

Land surface E plays several crucial roles in biogeochemical cycles, such as determining the availability of water resources (Ajjur & Al-Ghamdi, 2021; Dezsai et al., 2018), and controlling SM, thereby influencing the carbon and nutrient cycles through plant transpiration and photosynthesis (Gentine et al., 2019). Moreover, land surface E also plays a critical role in regulating climate through a series of land-atmosphere coupling processes that affect SM, land surface temperatures, and precipitation (Koster et al., 2006; Seneviratne et al., 2006; Shukla & Mintz, 1982), and thus also impacts hydro-climatological extremes (Miralles et al., 2014). Water, after evaporating, becomes unavailable for further human use, making quantifying E losses important for planning and managing water resources, especially in regions where available water is limited (Brutsaert, 1982). Due to these reasons, land surface E has historically been measured using ground-based methods and tools, primarily based on turbulence measurements (e.g., eddy covariance (Swinbank, 1951)), energy budget (e.g., Bowen's ratio (Bowen, 1926)), and mass budget (e.g., lysimeter).

Even though accurate quantification of E can be achieved through *in-situ* measurement methods and tools, these methods either measure only one component of land surface E or do not differentiate between the different components of E. Moreover, similar to *in-situ* SM measurements, they are confined to point-scale studies and are costly. These drawbacks created a

demand for quantifying land surface E using satellite RS for better spatial and temporal coverage, which is essential for regional, continental, and global hydrological studies.

2.2.2 Evaporation from space

In contrast to SM retrievals, E lacks the direct fingerprint that can be exploited by satellite retrievals, thus RS retrieval approaches mainly rely on meteorological and biophysical variable observations using often one of these two approaches (Holmes, 2019):

1. deriving potential E in combination with evaporative stress based on statistical parameterization and observations,
2. solving the actual E as a residual of the surface energy-balance.

Given the context of the thesis, retrieval models based on the first approach, which is deriving actual E by limiting the potential E, will be discussed. One example is the model developed by Mu et al. (2007, 2011), which underpins the Moderate Resolution Imaging Spectroradiometer (MODIS) ET product (Mu et al., 2013) and utilizes the Penman–Monteith equation (Monteith, 1965). The Penman–Monteith formulation estimates potential E by accounting for energy constraints, aerodynamic resistance, and stomatal conductance, while the parametrization of surface resistance is based on LAI and surface humidity (Cleugh et al., 2007; Holmes, 2019). Due to this, it requires a relatively large amount of meteorological input data (Miralles et al., 2016). Another method to derive actual E and its components is the PT-JPL model by Fisher et al. (2008). It calculates three components of E, namely transpiration, soil E, and rainfall interception. First, R_n is partitioned into soil and canopy using LAI. Then the calculated available energy for each component is used to derive potential E rates based on the Priestley-Taylor equations, constrained by two types of ecophysiological functions where their values range from 0 to 1. One set represents plant physiological limitations derived from vegetation indices to limit transpiration from vegetation, and the other is related to water availability for soil E calculated using vapor pressure deficit. Due to the simplicity of required parametrization, only five forcing variables are needed: net radiation, air temperature, air humidity, and vegetation characteristics.

Similarly, GLEAM, which is used in this thesis, also makes use of the Priestley-Taylor equation to derive potential E estimates but uses a running soil-water balance approach to constrain potential E, along with plant physiological limitations based on observed vegetation indices (vegetation optical depth (VOD)) (Martens et al., 2017; Miralles et al., 2011). SM conditions derived from the running soil-water balance are also updated through the DA of MW observations (Lievens et al., 2017a; Rains et al., 2022) or SM retrieval products (Koppa et al., 2022; Martens et al., 2016; Martens et al., 2017, 2018a; Miralles et al., 2010).

Thus, it can be said that for the algorithms of the top-down approaches (i.e., limiting derived potential E based on stress conditions to calculate actual E), the ability to capture the influence of irrigation on E fluxes is determined by how well stress conditions can be modeled or observed. As explained in Sections 2.1 and 2.3, the development of SM products and the increase

in the availability of MW observations at finer resolutions are quite recent. The development of SM retrievals at finer resolutions promises to enhance land surface E estimates in the future (McCabe et al., 2019).

2.3 Irrigation estimation and measurement

Irrigated agriculture is essential for food production, particularly in arid and semi-arid regions, by providing crucial water to crops during dry growing periods. Understanding the spatial and temporal patterns of irrigation practices, as well as their impact on critical hydrological variables like E and SM, is vital for effective water resources management and climate research in these areas. With the changing climate, stress on water resources in these regions is expected to increase (FAO, 2018b). Therefore, precise knowledge of irrigation amounts, timing, and spatial extent is essential for decision-makers to enhance water use efficiency, allocate water to different sectors effectively on a seasonal basis, and plan basin development (Ouaadi et al., 2021).

Despite the importance of irrigation information, there are major knowledge gaps regarding the amounts and timing of individual irrigation events. Basin authorities typically only know the water delivered through main canals, not the specific fields or their irrigation usage (Mas-sari et al., 2021; Zappa et al., 2022). Additionally, accurate *in-situ* data on irrigation extent is often lacking, with most information coming from national-scale surveys that have uncertainties (Brocca et al., 2018). These surveys often fail to account for unregulated irrigation practices, such as those using illegal wells on private lands without proper authorization, resulting in incomplete, biased, and potentially misleading assessments of irrigation coverage and quantification (OECD, 2015; Yilmaz et al., 2021).

2.3.1 Irrigation from space

To bridge the knowledge gap regarding irrigation practices, recent advances in RS are being employed to address critical questions such as where, when, and how much irrigation is occurring (McDermid et al., 2023). Optical and visible RS sensors have been extensively used to map the extent of irrigated areas at different spatial resolutions. Early examples of global land use classification studies derived irrigation extents at relatively coarse resolutions, such as utilizing SPOT 4 to develop the Global Land Cover 2000 (GLC2000) dataset (Bartholomé & Belward, 2005), United States Geological Survey (USGS) land classification from Advanced Very High Resolution Radiometer (AVHRR) (Loveland et al., 2000), and the global land cover product (GlobeCover) from The Medium Resolution Imaging Spectrometer (MERIS) (Arino et al., 2007). More recent studies have utilized higher spatial resolution optical and visible RS sensors such as MODIS (Dheeravath et al., 2010; Thenkabail et al., 2005), Sentinel-2 (Dari et al., 2024), and Landsat (Deines et al., 2019; Xie & Lark, 2021; Xie et al., 2021) to map the extent of irrigated areas on global and regional scales. Moreover, constellations of ultra-high resolution satellite missions, such as CubeSat, are also expected to provide valuable information in the future (Brocca et al., 2018; McCabe et al., 2017).

Compared to optical and visible observations for mapping the extent of irrigated areas, remotely sensed observations of SM are shown to be more suitable for quantifying the actual water used for irrigation since they can capture the temporal and spatial variations in SM which may be heavily influenced by irrigation practices over irrigated domains (Dari et al., 2023). However, SM retrievals from MW observations were previously at coarse resolutions, making it difficult to distinguish SM signals from irrigated fields, as finer resolution SM information is required due to the smaller size of irrigated croplands compared to the coarse resolution of SM retrievals (Dari et al., 2023; Ozdogan et al., 2010b; Peng et al., 2021). Due to the given challenges, most of the initial studies focused on modeling irrigation water requirements using re-analysis products (Wada et al., 2014) or coarse resolution RS observations (Hoffman et al., 1975) rather than retrieving actual irrigated water amounts using RS, as high-resolution SM observations were developed later (Brocca et al., 2018).

One of the earliest examples of testing the feasibility of retrieving irrigation amounts for large-scale applications using SM observations was conducted by Brocca et al. (2018) with coarse resolution SM retrievals from SMAP (36km), SMOS (40km), ASCAT (25km), and AMSR2 (25km) over agricultural regions in the United States, Europe, Africa, and Australia. The results demonstrated that uncertainties and errors in retrieved irrigation amounts were primarily due to coarse spatial resolution. Additionally, it is also noted that variables such as the revisit time of observations, uncertainty of retrievals, and climatic conditions of sites significantly affected the quality of irrigation amount retrievals. Another feasibility study using coarse resolution SM retrievals with AMSR2 (25km) was conducted by Jalilvand et al. (2019) over agricultural plains in Iran. This study showed that AMSR2 SM retrieval products could capture the temporal patterns of irrigation but systematically overestimated irrigation compared to *in-situ* data. Moreover, in the study by Zaussinger et al. (2019), combined coarse resolution satellite SM data from SMAP (36km), ASCAT (25km), and AMSR2 (25km) with reanalysis data The Modern-Era Retrospective analysis for Research and Applications - version 2 (MERRA-2) (Global Modeling And Assimilation Office & Pawson, 2015) was used to quantify irrigation water use over the contiguous United States for the period 2013–2016. The study found that combining RS and reanalysis products can greatly improve the accuracy of irrigation water use estimates. Another example of utilizing coarse resolution SM retrieval products from SMAP, SMOS, ASCAT, AMSR2, and European Space Agency (ESA) Climate Change Initiative (CCI) to derive irrigation amounts was conducted by Zhang et al. (2022). The main conclusion was that errors in retrieved irrigation amounts were primarily due to coarse spatial resolution, again highlighting the need for high-resolution SM products to enhance the quality of irrigation estimates.

With the availability of high-resolution MW observations from Sentinel-1, the spatial resolution of SM retrieval products has greatly improved. This advancement has led to studies exploring the feasibility of detecting the impact of irrigation on SM (without measuring irrigation amounts) using products from Sentinel-1. A pioneering study by Bauer-Marschallinger et al. (2019) demonstrated that the Sentinel-1 SM retrieval product, utilizing the TU Wien Change Detection algorithm at a 1km resolution, can effectively capture the influence of irrigation on SM in heavily irrigated areas. However, it is noted that due to the nature of SM retrieval

using high-resolution MW observations, vegetation influence is considerable, leading to a positive bias in SM estimates during vegetated periods compared to earlier coarse-resolution SM retrievals, especially over irrigated croplands. Consequently, a study by Quast et al. (2023) investigated the use of another algorithm, First-Order Radiative Transfer Model (RT1) (Quast et al., 2019), to retrieve SM from Sentinel-1, aiming to minimize the effects induced by the seasonal variability of the covering vegetation layer at a 1km resolution. The results demonstrated that the RT1 algorithm performs well in retrieving SM across various land cover types, including irrigated croplands. Another evaluation study by Jalilvand et al. (2021) tested the detection of irrigation impact on SM using SM retrieval algorithms at finer resolutions with SMAP (9km) and SMAP/S-1 (1 and 3km), where the SMAP/S-1 SM retrieval is a product of an active-passive algorithm that disaggregates low-resolution TB from SMAP using Sentinel-1 SAR data to retrieve high-resolution SM from the disaggregated TB (Das et al., 2019). This study demonstrated that the higher spatial resolution from SMAP/S-1 could more effectively capture the variability in SM over agricultural domains compared to the 9km version of the SMAP SM product.

Algorithms that combine high-resolution data with coarse resolution SM products are also used to improve the spatial resolution of SM derived from coarse resolution MW observations. One such algorithm is DISaggregation based on a Physical And Theoretical scale CHange (DISPATCH), a deterministic approach to downscale coarse-resolution SM retrieval products by leveraging physical relationships between finer-scale soil evaporative efficiency data from MODIS and SMOS (Merlin et al., 2008). It has been applied to both SMOS and SMAP SM products, resulting in high-resolution SM products over the Ebro Basin (Merlin et al., 2013; Ojha et al., 2021). Building on these advances in retrieving SM at finer spatial resolutions and enhancing the spatial resolution of coarse SM retrievals, several studies have investigated utilizing SM retrieval products from Sentinel-1, SMAP/S-1, and SMOS/SMAP DISPATCH for retrieving irrigation amounts over irrigated domains.

Dari et al. (2020) demonstrated the use of SMOS and SMAP DISPATCH products to retrieve irrigation amounts over the northeast of the Iberian Peninsula using the SM2RAIN algorithm (Brocca et al., 2014), showing that these products and the SM2RAIN algorithm can capture not only the long-term magnitudes of irrigation but also the spatial extent and timing of irrigation events. Zappa et al. (2021) utilized the Sentinel-1 SM product from the TU Wien Change Detection algorithm to derive irrigation amounts and concluded that the lack of consideration of vegetation contribution to backscatter in SM retrieval was the main cause of poor detection of irrigation events. In a modified version of this method, Zappa et al. (2022) integrated ESA CCI, Sentinel-1 TU Wien Change Detection, and SMAP SM products at the field scale, highlighting that low temporal and spatial resolution reduces the accuracy of irrigation retrieval. Another study by Dari et al. (2023) derived irrigation amounts spatio-temporally over three highly human-influenced regions: the Ebro Basin in Spain, the Po Basin in Italy, and the Murray-Darling Basin in Australia. The SM2RAIN algorithm was tested again with the Sentinel-1 SM product from the RT1 algorithm. *In-situ* validation results from the Ebro and Murray-Darling basins showed that both the timing and amounts of irrigation were satisfactorily obtained.

However, validation over the Po Valley was affected by uncertainties due to the number and size of irrigated areas. The study highlighted that the dynamic nature of irrigation extents, influenced by economic factors, climatic conditions, and crop rotation, means the proposed methodology cannot correct wrongly retrieved irrigation amounts over non-irrigated areas or false irrigation amounts during non-irrigated seasons over irrigated areas.

2.3.2 Data assimilation and irrigation

Land surface, crop, and hydrological models are shown to be effective tools for providing spatio-temporally continuous hydrological estimates based on physical laws derived from historical observations and for simulating the interactions between the Earth's land surface and the atmosphere (Lahoz & De Lannoy, 2014). Moreover, as also explained in Sections 2.1 and 2.2, RS observations have the potential to be utilized for retrieving many hydrological state variables and fluxes (Tang et al., 2009); however, they usually provide an instantaneous view of the land surface and are discrete in time and space (Lahoz & De Lannoy, 2014). Models, on the other hand, fail to account for anthropogenic processes such as irrigation and its effects on basins, such as groundwater recharge and depletion, and flux estimates like E (Kumar et al., 2015). Therefore, despite the marked growth in the availability of land surface satellite data and model sophistication arising from the dramatic growth in computational power and improved understanding of the physics and dynamics of the Earth system, neither can provide a complete picture of the hydrological cycle (De Lannoy et al., 2022; Lahoz & De Lannoy, 2014; Liu & Gupta, 2007).

To optimally merge the information from models and RS, DA theory provides methods to enhance uncertain model predictions (Liu & Gupta, 2007; Reichle et al., 2002). There are two main categories of numerical algorithms for data assimilation: variational and sequential (Lahoz & Schneider, 2014). In this section, studies focused on sequential methods will be examined, considering the content of the dissertation.

To understand the basic concept of DA, the following scalar example can be examined. To find the least-squares estimate \hat{x} , objective function J is defined to estimate the misfit between true state x and the model estimate m and observation o while considering model and observation uncertainties σ_m^2 and σ_o^2 , respectively (Reichle, 2008):

$$J = \frac{(x - m)^2}{\sigma_m^2} + \frac{(x - o)^2}{\sigma_o^2} \quad (3)$$

The objective function J is minimized when $\frac{dJ}{dx} = 0$. Solving this gives the estimate \hat{x} :

$$\hat{x} = (\sigma_o^2 + \sigma_m^2)^{-1} (\sigma_o^2 m + \sigma_m^2 o) = m + K(o - m), \quad \text{where } K = \frac{\sigma_m^2}{\sigma_m^2 + \sigma_o^2} \quad (4)$$

where $o - m$ represents the innovations (Courtier & Bouttier, 2002). In a realistic variational DA applications, model estimates m and observations o are arranged into long state vectors \mathbf{m} ,

\mathbf{o} and the scalar error covariance becomes the error covariance matrix of these model states. Due to the immense size of the vectors and matrices, variational DA algorithms minimize J using advanced numerical methods, over a specific time interval (Reichle, 2008) thus implicitly. In contrast, sequential DA algorithms explicitly consider the error covariances at each step (Kalman, 1960). Explicitly setting up \mathbf{K} differs for different sequential DA algorithms. For instance, in the EnKF approach, \mathbf{K} is calculated using an ensemble of model states from each time step to estimate the error covariances needed for Equation 4 (Evensen, 1994).

In Equation 4, it is assumed that model state variables are directly observable, thus directly comparable with the model estimates. However it is rarely the case, as satellite observations mostly come in the form of radiance (Reichle, 2008). Thus two different approaches exist: (1) converting (i.e. inverse operator) observed radiance into geophysical retrievals (e.g., SM, snow water content, vegetation) or (2) mapping the model estimates into satellite observed signals using so called forward (or observation) operators (e.g., RTMs) (De Lannoy et al., 2022).

The former option (inverse operator), usually has its own drawbacks and uncertainties associated, as it relies on a number of auxiliary data that might be inconsistent with the model simulations (Lievens et al., 2017a; Rains et al., 2022) (see Section 2.1). Additionally, using retrieval products can introduce bias in a data assimilation system (de Roos, 2023) where such problem and possible solution is illustrated in Martens et al. (2017). For the latter approach, the direct assimilation of satellite observations into models combines the strength of spatio-temporally continuous model estimates with discrete real-world observations (Lievens et al., 2017a; Rains et al., 2022), and since satellite observations provide information on multiple variables (such as SM and vegetation), they can be used to update multiple model estimates that are related to observations simultaneously (Bechtold et al., 2023; de Roos, 2023; Modanesi et al., 2022).

DA algorithms have been extensively used to improve modeled SM estimates. For instance, Rains et al. (2018) utilized the SMOS and SMAP brightness temperatures separately within the Community Land Model (Lawrence et al., 2019). The performance of DA systems improved with the addition of Sentinel-1 backscatter data. Lievens et al. (2017b) demonstrated the added value of high-resolution radar observations for DA systems. Integrating SMAP radiometer and Sentinel-1 radar observations into the NASA catchment land surface model (Li, 2018), both separately and jointly, showed that adding Sentinel-1 data increased the assimilation impact by up to 30% compared to assimilating only SMAP radiometer observations.

Although larger-scale applications that have utilized passive MW satellites are abundant, capturing the influence of irrigation on SM or quantifying irrigated water use through DA has been less explored. This is primarily because high-resolution SM observations, which have proven to be more beneficial over agricultural domains, have only recently become available (Lawston et al., 2017). One of the first studies to examine the improvement of irrigation representation in models through the assimilation of SM retrieval products is Lawston et al. (2017). This study demonstrated that an enhanced version of SMAP (ONeill et al., 2016) could detect the bulk seasonal timing and spatial signature of irrigation via elevated SM compared to

non-irrigated adjacent areas. Further exploration by Modanesi et al. (2022) and Modanesi et al. (2021) focused on optimizing the forward operator specifically over irrigated land and the benefits of assimilating Sentinel-1 backscatter to quantify irrigation. Their results highlighted the added value of DA. However, they also noted that crop rotation and the influence of crop types on backscatter observations might not be accurately represented by the calibrated WCM parameters, as a single parameter set was used for each model grid-cell, regardless of crop-type variability. Therefore, robust methodologies that can be applied in larger-scale applications to quantify irrigation and irrigation fluxes from satellite data are still needed (De Lannoy et al., 2022).

3 Materials and methods

In this section, the materials and methods used to assimilate Sentinel-1 backscatter data for incorporating irrigation into GLEAM SM and E estimates are detailed. First, the study area, the Ebro Basin, and the *in-situ* SM data are described in Section 3.1. The GLEAM algorithm is then outlined in Section 3.2. Since GLEAM does not produce backscatter, a forward operator is necessary to compare Sentinel-1 backscatter observations with simulated GLEAM backscatter; the details are provided in Section 3.4.1. Consequently, the required calibration of the forward operator for each grid-cell of GLEAM is explained in Section 3.4.2. The sequential data assimilation algorithm, EnKF, used to update the top layer GLEAM SM based on observed and simulated backscatter, is discussed in Section 3.4.3. Finally, the experiments conducted to evaluate the performance of the proposed DA approach are explained in Section 3.5.

3.1 Study area – Ebro Basin

The Ebro Basin in Spain, selected as a case study, is located in the northeast part of the Iberian Peninsula. It encompasses elevations ranging from sea level to the 2640 meters and covers an area of approximately 86,200 km² (Figure 3.1). The Central Ebro Valley lies in the depression part of the basin, surrounded by the Cantabrian and Pyrenees mountain ranges in the north and Iberian Mountain in the south. The basin's heterogeneous topographical properties, coupled with contrasting climatic influences from Mediterranean and Atlantic, as well as the influence of large scale atmospheric patterns, have an significant impact on the complex climatic conditions over the basin (Duarte et al., 2021; Vicente-Serrano & López-Moreno, 2006). Meteorological conditions vary substantially, with precipitation ranging from up to 1800 mm yr⁻¹ in the mountain ranges to only 500 mm yr⁻¹ in the Central Ebro Valley (Dari et al., 2023). Precipitation seasonality is also pronounced in the basin, where most of the precipitation falls in autumn and spring in the central part (Comin, 1999; López-Moreno et al., 2011). Maximum and minimum precipitation occur during winter and summer, respectively, in the northern and northwest regions of the basin (Comin, 1999). Moreover, due to complex topography gradients and climatic conditions mean annual temperatures ranges from almost 0 to 16.2 °C (López-Moreno et al., 2011).

Major land cover types in Ebro Basin can be seen in Figure 3.2. Based on the 2018 Coordination of Information on the Environment (CORINE) land cover dataset (European Environment Agency & European Environment Agency, 2019), 44.4% of the basin is cultivated (based on agricultural area definition in the land cover dataset) (37,946 km²) of which 18.4% of its is irrigated (based on irrigated croplands and rice fields definition in the land cover dataset). 25.1% of the basin is grassland (based on natural grassland, moors and heathland, sclerophyllous vegetation and transitional woodland/shrub definition in the land cover dataset) (21,393 km²) and 26.5% is forested areas (defined as broad-leaved forest, coniferous forest and mixed forest definition in the land cover dataset) (22,677 km²).

To assess the performance of the SM estimates after assimilating Sentinel-1 backscatter data,

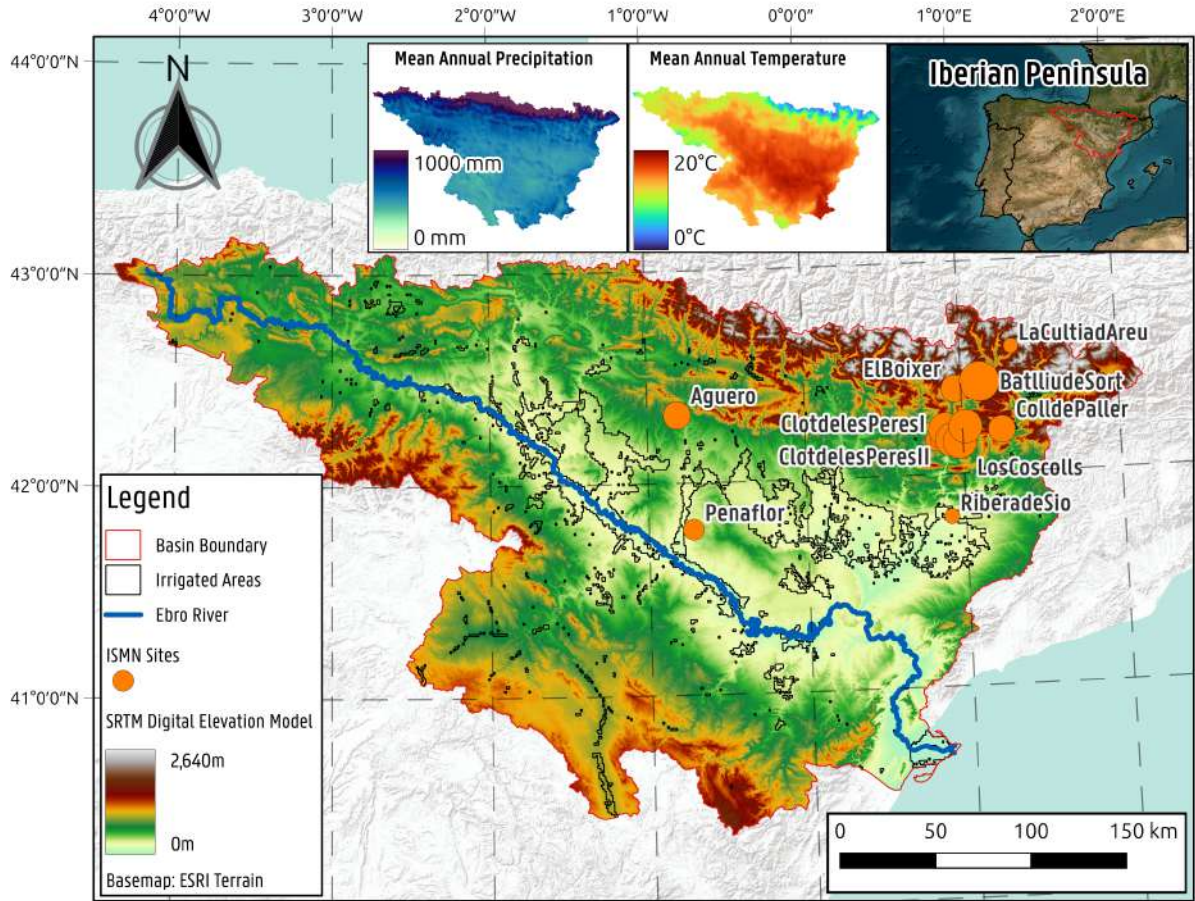


Figure 3.1: Ebro Basin boundaries, irrigated areas, Ebro river, ISMN sites, and digital elevation map. Long-term (2016–2021) mean annual precipitation and temperature values over Ebro Basin computed from forcing dataset is shown in subplots. The size of the ISMN site symbols is directly proportional to the length of the data record.

SM time series from ISMN (Dorigo et al., 2021b) stations are collected over the Ebro basin for the period 2016–2021. Firstly, the hourly *in-situ* SM data are filtered to ensure that the percentage of gaps at the hourly scale did not exceed 25%. This step was necessary to select only stations with sufficient hourly measurements to accurately represent average daily SM values. Secondly, stations with less than 365 days of daily data or with gaps exceeding 20% are excluded. This measure ensured the inclusion of only those stations with good temporal coverage across different seasons.

This process resulted in the selection of 13 stations from two different SM networks: Institut cartogràfic i Geològic de Catalunya (XMS-CAT)¹ and Instituto Pirenaico de Ecología (IPE) (Al-day et al., 2020). The summary of each station, including network, station name, land cover, location, and period of record, is shown in Table 3.1 and illustrated in Figure 3.1. Land cover classifications reported on Table 3.1 are based on the metadata associated with *in-situ* data provided by ISMN. Notably, only one station belongs to an irrigated agricultural field, while most of the stations are located in the northern part of the basin in non-irrigated areas (Figure

¹The work of Agnès Lladós and Lola Boquera as well as the XMS-CAT network team in support of the ISMN is acknowledged.

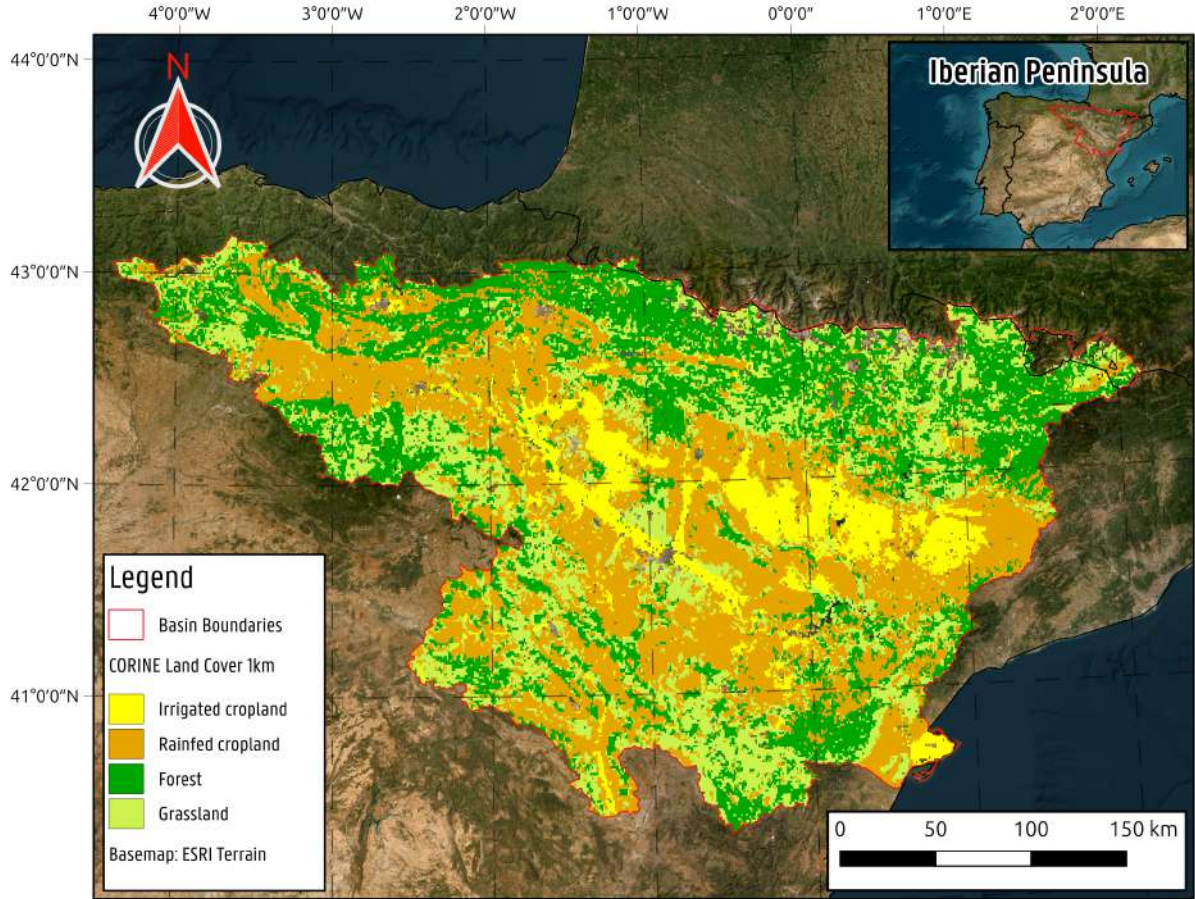


Figure 3.2: Ebro Basin CORINE land cover types.

3.1).

Despite the availability of *in-situ* SM measurements, the Ebro Basin does not have *in-situ* E data, which hinders the direct evaluation of E estimates.

3.2 Global Land Evaporation Amsterdam Model

GLEAM is a model designed to estimate daily SM and different components of terrestrial E including transpiration, interception loss, bare-soil evaporation, snow sublimation, and open-water evaporation (Martens et al., 2017; Miralles et al., 2011). Each grid-cell in GLEAM is represented by four separate land cover fractions: (1) bare soil, (2) short vegetation, (3) tall vegetation and (4) open water. One vertical layer (0–10 cm) is simulated for bare soil, two (0–10 cm and 10–100 cm) for short vegetation and three (0–10 cm, 10–100 cm and 100–250 cm) for tall vegetation fraction. The total terrestrial E is calculated separately for each land cover fraction and aggregated at the grid-cell scale based on their respective fractions.

First, potential E (mm day^{-1}) for each land cover fraction is calculated based on the Priestley-Taylor equation (Section 3.2.3). Next, the separate rainfall interception loss (mm day^{-1}), i.e., the direct vaporisation of intercepted rain by canopy, is calculated for only for the tall fraction

Table 3.1: *In-situ* soil moisture sites with their respective land cover and data availability.

Network	Station	Land Cover	Elevation (m)	Depth (m)	Period of Record
IPE	Aguero	Forest	746.35	0.06	2016-01-01/2020-02-12
	Penaflor	Shrubland	0.0	0.1	2017-06-03/2020-03-25
XMS-CAT	ClotdelesPeresI	Cropland-rainfed	604.0	0.05	2017-11-01/2020-02-12
	ClotdelesPeresII	Cropland-rainfed	602.0	0.05	2020-05-15/2021-07-19
	SerradeCostaAmpla	Cropland-rainfed	922.0	0.05	2017-03-30/2021-12-31
	RiberadeSio	Cropland-irrigated	283.0	0.05	2020-03-01/2021-12-31
	CamidelsNerets	Cropland-rainfed	487.0	0.05	2017-03-30/2021-12-31
	ElBoixer	Grassland	1217.0	0.05	2019-03-01/2021-12-31
	LosCoscolls	Cropland-rainfed	560.0	0.05	2017-11-01/2021-12-31
	Pessonada	Cropland-rainfed	911.0	0.05	2017-03-30/2021-12-31
	BatlliudeSort	Grassland	890.0	0.05	2016-08-01/2021-12-31
	ColldePaller	Cropland-rainfed	1164.0	0.05	2019-03-01/2021-12-31
	LaCultiadAreu	Grassland	1236.0	0.05	2020-03-01/2021-12-31

based on Gash’s analytical model (Gash, 1979; Gash & Stewart, 1977) (Section 3.2.1). Afterwards, a soil water balance module is applied to distribute the incoming net precipitation (precipitation minus interception) and snow-melt over different soil layers (Section 3.2.2). After deriving the SM, a third module is applied to determine the stress conditions, S , which used to limit the potential E based on available water and dynamic vegetation information from satellite-based observations (Section 3.2.4). Finally, estimates of potential E are then converted to actual E (mm day^{-1}) estimates using the stress factor, S , calculated in the previous step.

Figure 3.3 gives an overview of the different modules of GLEAM and its forcings, while Table 3.2 summarizes the sources of forcing datasets and static variables that is used in this study.

3.2.1 Interception module

The amount of water that evaporates from the canopy, i.e., rainfall interception loss, is calculated based on daily rainfall data, incorporating factors such as canopy cover, canopy storage capacity, and the average rates of rainfall and E when the canopy is wet. The separate rainfall interception module used in GLEAM is validated with *in-situ* observations of rainfall interception (Miralles et al., 2010). For further details related to the rainfall interception module, please refer to Miralles et al. (2010).

3.2.2 Soil water balance module

At each daily time step i , the water content state $w_i^{(l)}$ of the vertical layer l is calculated based on the simplified water balance, which is:

$$w_i^{(l)} = w_{i-1}^{(l)} + \frac{(F_{s,i}^{(l-1)} + F_{f,i}^{(l-1)} - E_{i-1}^{(l)} - F_{s,i}^{(l)}) \Delta t}{\Delta z^{(l)}} \quad (5)$$

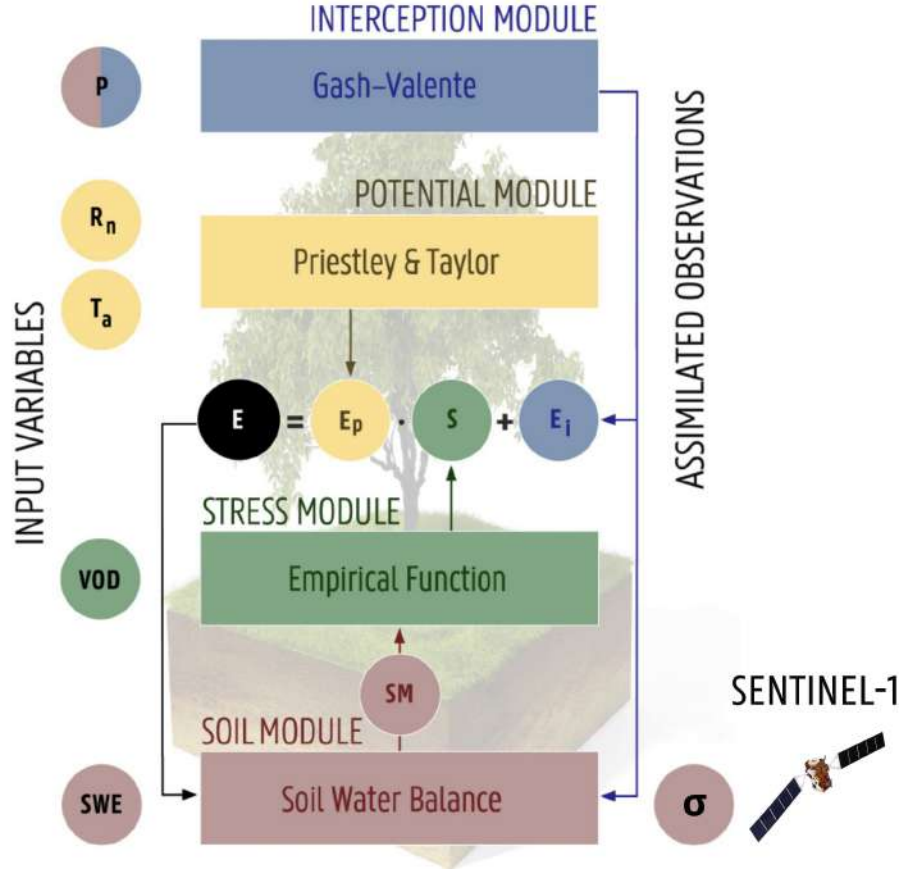


Figure 3.3: Overview of GLEAM modules and their respective forcings. Modified from Martens et al. (2017).

where $w_{i-1}^{(l)}$ (m^3m^{-3}) is the volumetric moisture content of layer l at the previous day ($i - 1$), $F_{s,i}^{(l-1)}$ (mm day^{-1}) is the slow draining flux into the layer, $F_{f,i}^{(l-1)}$ (mm day^{-1}) is the fast draining flux into the layer, $E_{i-1}^{(l)}$ (mm day^{-1}) is the E from the previous day, $F_{s,i}^{(l)}$ (mm day^{-1}) is the slow drainage of water to the deeper layer, Δt is the temporal resolution (1 day), and $\Delta z^{(l)}$ (mm) is the depth of the layer.

After calculating the interception loss, net precipitation, i.e., precipitation minus interception, is calculated at the beginning of each time step which is then partitioned between the vertical soil layers based on relative saturation of each layer to estimate the fast draining flux $F_{f,i}^{(l-1)}$. Next, the volume of water that slowly drains to the subsequent layer is estimated based on simplified Darcy's law. This involves draining a portion of the available water above the wilting point to the next layer, determined by the relative saturation of each layer and SM gradient between the layers.

3.2.3 Potential evaporation module

To derive cover fraction-dependent potential E_p (mm day^{-1}) based on air temperature and net radiation, the Priestley-Taylor equation (Priestley & Taylor, 1972) is utilized which can be written as:

$$\lambda E_p = \alpha \frac{\Delta}{\Delta + \psi} (R_n - G) \quad (6)$$

where λ (MJ kg^{-1}) is the latent heat of vaporization, Δ (kPa K^{-1}) is the slope of saturated water vapor temperature curve, ψ (kPa K^{-1}) is the psychrometric constant of air, α (-) is the Priestley and Taylor coefficient, R_n (W m^{-1}) is the net surface radiation, and G (W m^{-1}) is the ground heat flux, i.e., surface outgoing shortwave radiation. If R_n is negative, G is taken as fixed fraction depending on the cover type. α value also depends on the land cover type, where 1.26 is used for bare soil fraction based on Priestley and Taylor (1972), but relatively more conservative value 0.97 is used based on findings of Diawara et al. (1991), Eaton et al. (2001), McNaughton and Black (1973), Shuttleworth (1984), and Viswanadham et al. (1991) for tall and short vegetation fraction as several studies have highlighted conservative nature of tree stomata often results in lower rates of potential E in forested areas (Kelliher et al., 1993; Shuttleworth & Calder, 1979; Teuling et al., 2010).

3.2.4 Stress module

For most land surfaces, actual E rarely reaches the potential rate due to environmental limitations such as water availability, heat stress, and phenological constraints, which are accounted for by an empirical parameter defined as the evaporative stress factor, ranging from 0 (maximum stress) to 1 (no stress) (Miralles et al., 2011). The stress function is defined separately for each vegetation-covered fraction (Equation 7) and bare soil (Equation 8) (Martens et al., 2017) (Figure 3.4).

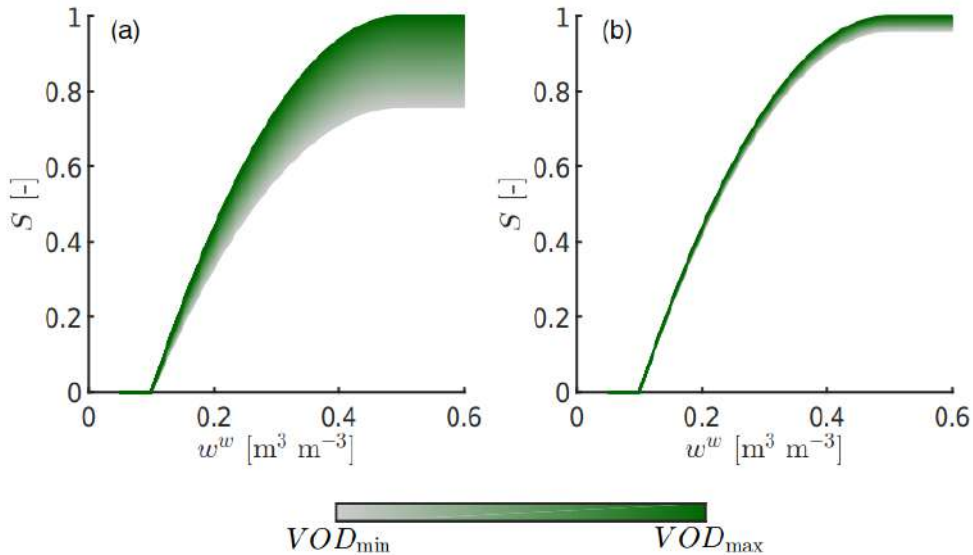


Figure 3.4: Stress function implemented in GLEAM for vegetated fractions. High range of VOD (left) [0.27-0.47]; Small range VOD (right) [0.38-0.40]. Retrieved from Martens et al. (2017).

For tall and short vegetation, the non-linear stress function is defined as:

$$S = \sqrt{\frac{VOD}{VOD_{max}}} \left(1 - \left(\frac{w_c - w^{(w)}}{w_c - w_{wp}} \right)^2 \right) \quad (7)$$

where VOD_{max} (-) is the maximum VOD, w_c ($\text{m}^3 \text{m}^{-3}$) is the critical SM, and $w^{(w)}$ ($\text{m}^3 \text{m}^{-3}$) is the SM content of the wettest layer for a specific grid-cell.

The linear stress function to limit potential E for the bare soil fraction is calculated as:

$$S = 1 - \frac{w_c - w^{(1)}}{w_c - w_r} \quad (8)$$

where w_r ($\text{m}^3 \text{m}^{-3}$) is the residual SM.

Table 3.2: GLEAM forcing datasets and their characteristics.

Variable	Type	Source	Native resolution	Reference
Radiation	Forcing	LST-Planet & LSAF	5km, 1km	Rains et al. (2024)
Precipitation	Forcing	SM2RAIN	0.01°	Brocca et al. (2014)
Air temperature	Forcing	LST-Planet & LSAF	5km	Rains et al. (2024)
Snow water equivalent	Forcing	GLOBSNOW L3v2 & NSIDC v01	25km	Armstrong et al. (2005) Luoju et al. (2013)
Vegetation optical depth	Forcing	VOD-Planet		
Cover fractions	Static	MODIS MOD44b	250m	DiMiceli et al. (2015)
Soil properties	Static	HiHydroSoil v2.0	1km	Simons et al. (2020)
Lightning frequency	Forcing	LIS/OTD	5km	Mach et al. (2007)
Leaf area index	Assimilation	MODIS MOD44Bv6.1	500m	Myneni et al. (2021)
Backscatter Coefficient	Assimilation	Sentinel-1	20m	Raml et al. (2023) Bauer-Marschallinger et al. (2019)

First, GLEAM with 1km resolution forcings is run without any Sentinel-1 DA (i.e, OL) for the spin-up period 2016–2021. GLEAM is run again for the period 2016–2021 over Ebro Basin with the initial conditions of last day of spin-up period, with the whole period also serving as DA evaluation period. In this study, a specific 1km and daily version of GLEAM originally developed for the ESA Digital Twin Earth (DTE) project, is utilized. This version of GLEAM retains the core methodology described above, with the primary modifications being the spatial resolution of the products to force the model and the assumption that land cover fractions remain constant over time (Table 3.2).

3.3 Sentinel-1 SAR backscatter

The Sentinel-1 mission consists of two polar-orbiting, sun-synchronous satellites, Sentinel-1A and Sentinel-1B, equipped with C-band (5.4 GHz) synthetic aperture radar (SAR), which allow them to collect data regardless of weather conditions (such as clouds) and time of day (Bauer-Marschallinger et al., 2021). Sentinel-1A has been operating and acquiring data since October 2014, and Sentinel-1B since October 2016. Both satellites have 12-day repeat cycles and 175 relative orbits per cycle, which are combined to achieve revisit times from 3 to 6 days over Europe. Sentinel-1 operates in four different modes, with the Interferometric Wide (IW) swath mode used in this study, capturing data over a 250km swath with a spatial resolution of 5m x 20m. Due to the failure of the power supply in its instrument electronics, Sentinel-1B is no longer active, reducing the mission's temporal resolution to that of only Sentinel-1A. However, the launch of Sentinel-1C in 2024 will re-establish full mission capacity, and the launch of Sentinel-1D in 2025 will complete the development of the first generation (ESA, 2022; Miranda et al., 2023).

Operating at a higher spatial resolution than its predecessors such as SMAP, SMOS, ASCAT, ERS-1/2, and AMSR2, Sentinel-1 is capable of retrieving SM information with greater spatial detail (Wagner et al., 2009). However, high resolution SAR observations are more sensitive to ground features like surface roughness, vegetation water content, crop row orientation, vegetation, and urban structures which makes retrieving SM from complex SAR signal harder compared to coarser spatial resolution observations (Bauer-Marschallinger et al., 2019; Wagner et al., 2009). However, the study by Bauer-Marschallinger et al. (2019) has demonstrated that when the high-resolution SAR signal is up-scaled/down-sampled to a 1km scale/500m sampling, it still retains the SM signal, while the effects of surface roughness and vegetation are minimized, assuming:

1. individual fields in the coarse grid-cell have similar SM dynamics,
2. roughness and vegetation driven signal from individual fields are mutually independent and sum up incoherently when up-scaled .

All models that explain the backscatter characteristics of soil agree that the radar backscatter coefficient increases with increasing SM due to the increase in the dielectric constant (Bahar, 1981; Ulaby et al., 1978; Wagner et al., 2022). However, ASCAT, ERS-1/2, and Sentinel-1 SAR observations have shown that under arid conditions, this relationship can become negatively correlated due to a phenomenon called subsurface scattering (Wagner et al., 2013, 2022). This occurs when the signal penetrates too deeply into the soil, causing the backscatter to increase due to reflections from the rock sublayer (Morrison & Wagner, 2020; Wagner et al., 2022). Although Wagner et al. (2022) highlighted the need for further research to improve the understanding of the impact of subsurface scattering on SM and vegetation retrievals, Raml et al. (2023) demonstrated that identifying pixels potentially affected by subsurface scattering can be achieved by temporally correlating modelled SM, e.g., ERA5-Land top layer SM, with the backscatter coefficient. By removing pixels below a certain correlation threshold, it is assumed

that pixels affected by subsurface scattering are removed.

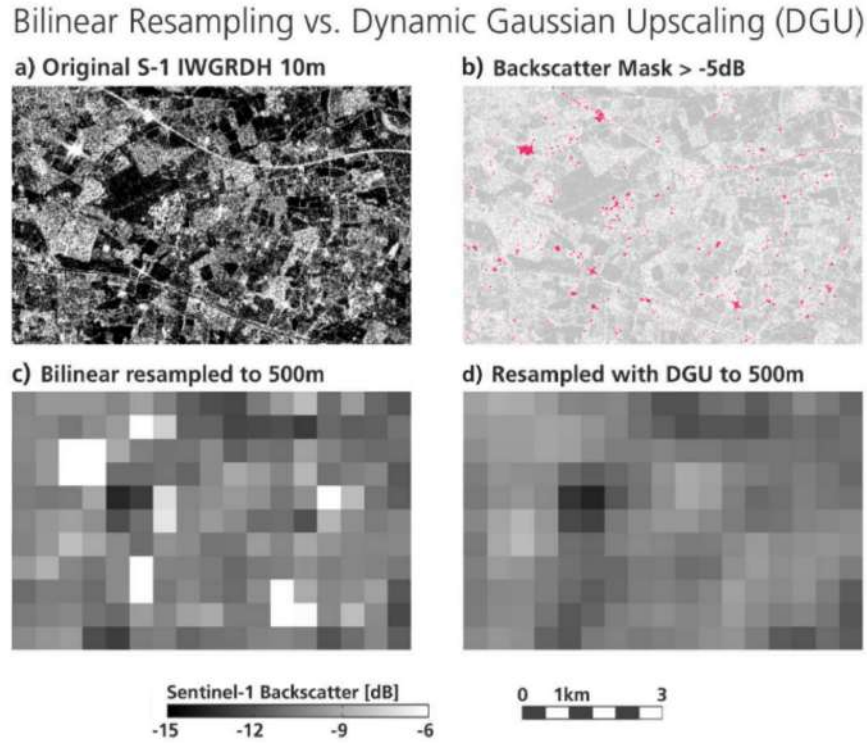


Figure 3.5: Resampling of Sentinel-1 images with simple bilinear resampling and DGU method highlighting polluted pixels over an agricultural area in England. © IEEE. Modified and reprinted from Bauer-Marschallinger et al. (2019).

Therefore, to potentially mitigate the aforementioned issues, Sentinel-1 images have undergone several preprocessing steps before their utilization in this study. Initially, Vertical-Vertical (VV)-polarised IW swath images are geocoded and radiometrically corrected using ESA Sentinel Application Platform (SNAP) software into Equi7Grid (Bauer-Marschallinger et al., 2014) spatial reference system. Subsequently, coarse resolution ECMWF ReAnalysis v5-Land (ERA5-Land) (Muñoz Sabater, 2019) top layer SM estimates are resampled and aligned with the 20m resolution Sentinel-1 backscatter data. Subsequently, snow-covered and frozen-soil grid-cells identified by ERA5-Land are masked due to the undefined relationship between backscatter and SM under such conditions (Raml et al., 2023). Then, pixels with Pearson's correlation coefficient (R) of less than 0.2 between the resampled ERA5-Land SM and Sentinel-1 backscatter are excluded. All the details of computing temporal correlations between Sentinel-1 backscatter and ERA5-Land SM are explained by Raml et al. (2023).

Next, up-scaling/down-sampling of the Sentinel-1 backscatter is performed using Dynamic Gaussian Upscaling (DGU) where the details are explained by Bauer-Marschallinger et al. (2019). Initially, very high (-5 decibel (dB)) and low (-19 dB) backscatter observations are discarded as they typically correspond to urban areas and open water surfaces, respectively, and do not hold any SM information. This dynamic masking step ensures that pixels without SM information do not contaminate the up-scaled pixels, as demonstrated in Figure 3.5b. Subsequently, pixels are spatially averaged from 10m to 500m sampling in linear scale (not in dB).

Additionally, a Gaussian filter with a 1km Full Width at Half Maximum (FWHM) is applied to the images to remove the aliasing effect, as shown in Figure 3.5d. It should be noted that all the aforementioned processes have been done by TU Wien Research Unit of Remote Sensing while the following processes after this point has been conducted by the author.

The resulting 500m-sampling images in the Equi7Grid spatial reference system, belonging to different relative orbits, undergo further processing to align with the current resolution and grid system of GLEAM. Images from different relative orbits are corrected for static bias between them as explained by Lievens et al. (2019). To achieve this, long-term backscatter values from each orbit are calculated for each pixel and then corrected with the overall mean (i.e., the entire backscatter dataset that includes all orbits). This step also helps minimizing for the effect of incidence angle differences of orbits before merging all the images from different orbits (de Roos, 2023; Lievens et al., 2019).

3.4 Data assimilation

In this section, details of the DA framework will be discussed. Section 3.4.3 covers the formulation of the EnKF, Section 3.4.1 provides details on the selected forward operator for the EnKF, and Section 3.4.4 discusses the details of ensemble generation.

3.4.1 Forward operator

Since GLEAM does not produce backscatter, a forward operator is necessary to compare Sentinel-1 backscatter observations with simulated GLEAM backscatter. The WCM is chosen as a forward operator which will transform model states (SM) and LAI observations into observation forecasts (Sentinel backscatter). The WCM, a volume scattering model representing total backscatter (σ^0) as the sum of vegetation backscatter (σ_{veg}^0) and soil backscatter (σ_{soil}^0), with soil backscatter attenuated by the vegetation layer coefficient (t^2) (Attema & Ulaby, 1978):

$$\sigma^0 = \sigma_{veg}^0 + t^2 \sigma_{soil}^0 \quad (9)$$

The vegetation attenuation parameter t^2 and vegetation backscatter σ_{veg} are defined as:

$$t^2 = \exp \frac{-2 B V_2}{\cos \theta} \quad (10)$$

$$\sigma_{veg}^0 = (1 - t^2) A V_2 \cos \theta \quad (11)$$

where θ is the incidence angle, V_1 and V_2 are bulk vegetation descriptors, A (-) is a fitting parameter controls the direct backscatter from vegetation, and B (-) is a fitting parameter drives attenuation of soil backscatter through the two way attenuation by vegetation (Equation 10). Sentinel-1 backscatter observations are not incidence angle normalized (Bauer-Marschallinger

et al., 2021), however bias correction steps, explained in Section 3.3, are excepted to minimize the effect of incidence angle differences between different relative orbits. Thus, a fixed incidence angle of 40° is assumed in line with Rains et al. (2022) for this study, which corresponds approximately to the mean incidence angle of normalized Sentinel-1 observations.

To model soil backscatter, semi-empirical and theoretical models exist (Baghdadi et al., 2015; Oh et al., 1992). However, their complex parameter requirements limit their application in large-scale studies (Lievens et al., 2017a). A simple linear approach (Equation 12) for modeling bare soil backscatter with SM has been shown to work well (De Roo et al., 2001; Geng et al., 1996; Toca et al., 2022; Wagner et al., 2008):

$$\sigma_{soil}^0 = C + D SM \quad (12)$$

where C is a fitting parameter related to surface roughness (dB), and D is a fitting parameter related to the sensitivity of backscatter to changes in SM (dB/m^3m^{-3}).

By definition, vegetation backscatter component (Equation 11) is in linear scale, while soil backscatter (Equation 12) is in dB scale. Thus to combine these two backscatter components to derive total soil backscatter in dB, bare soil backscatter (Equation 12) is first converted to linear scale before being used in Equation 9 using the following equation:

$$\sigma^0 (-) = 10^{\frac{\sigma^0 (dB)}{10}} \quad (13)$$

Since the comparison of Sentinel-1 backscatter observations and simulated backscatter is done in dB scale, Equation 9 is converted back to dB scale using the inverse of Equation 13.

Various vegetation descriptors can be used for V_1 and V_2 including LAI (Bechtold et al., 2023; Lievens et al., 2017b; Modanesi et al., 2021; Rains et al., 2022), normalized difference vegetation index (NDVI) (Rawat et al., 2022), VOD (Lievens et al., 2017a), cumulative biomass (de Roos, 2023), and vegetation water content (Park et al., 2019). In this study, LAI observations from MODIS (MOD44Bv6.1 product) are used to describe the backscatter and attenuation from the vegetation layer (Myneni et al., 2021), and top-layer GLEAM SM estimates are used to describe the backscatter from bare soil. The 4-day 500m LAI MODIS product is processed to a daily 0.01° resolution using bilinear interpolation for spatial resampling and linear interpolation for temporal resampling.

3.4.2 Calibration of Water Cloud Model

The WCM that will convert model-predicted SM forecasts to observation forecasts must be calibrated for each grid-cell. However, to have an efficient DA framework, unbiased calibration of the forward operator with unbiased observations and model states is crucial (Modanesi et al., 2022). The idea is that if unrealistic SM estimates from the OL (GLEAM SM estimates which irrigation is not accounted for) and real-world observations (Sentinel-1 σ_0 observations

which has irrigation in the signal) are used during the calibration, the calibration process will remove the systematic biases by adjusting the forward operator parameters accordingly. This will not effectively forecast the state variables into observation space, leading to unrealistic observation forecasts appearing closer to observations than they should be. This will lead to inefficient sequential update on SM due to the smaller innovations between observations and observation forecasts (see Section 2.3.2 Equation 4). Therefore, considering the assumption that Sentinel-1 backscatter observations include irrigation information but GLEAM does not, the bias during the growing period needs to be considered.

This issue was evident in the work of Modanesi et al. (2021, 2022), where Noah-MP (Niu et al., 2011) SM simulations provided unrealistic SM and LAI estimates due to the absence of irrigation. They addressed this by activating an irrigation scheme in Noah-MP (Ozdogan et al., 2010a) to minimize inconsistencies between simulated and observed backscatter during the calibration process. Similarly, de Roos (2023) demonstrated that cumulative biomass estimates in AquaCrop (Steduto et al., 2009) are not representative of Sentinel-1 backscatter observations, as there was no simulated decline in biomass following harvesting at the end of the growing season. They highlighted that adjusting the cumulative biomass description parameterization and/or excluding biased periods are effective methods for the WCM calibration process. However, few studies have focused on exploring different strategies to calibrate forward operators over irrigated areas (Modanesi et al., 2021, 2022).

Therefore, the performance of excluding OL SM during the growing season in the calibration process of WCM is explored using the The Food and Agriculture Organization of the United Nations (FAO) Crop/Pasture Phenology: Growing Seasons (1km) dataset (FAO, 2018a) and the 2018 CORINE land cover classification (European Environment Agency & European Environment Agency, 2019). These datasets are used to flag the irrigated grid-cells along with their respective growing season (Figure 3.6). Maps of the start and end of the growing seasons from the FAO Phenology dataset are categorical raster layers with a 0.008° spatial resolution. Thus, the nearest neighbor algorithm is used to match it with the GLEAM 0.01° grid. The CORINE land cover map has also been resampled from its native resolution of 100m to 0.01° using mode resampling, selecting the value which appears most often among all the sampled points. Subsequently, a binary map of irrigated areas (i.e., permanently irrigated land and rice fields) is created. Using the irrigated grid-cell, the start and end of growing season maps are converted to a spatio-temporal mask over irrigated areas representing the growing period, assuming irrigation only happens during the growing period.

Table 3.3: Water Cloud Model calibration parameter upper, lower boundary and initial values.

Variable	Unit	Initial value	Lower bound	Upper bound
A	-	0	0	5
B	-	0	0	1
C	dB	-15	-35	0
D	dB/(m ³ m ⁻³)	10	0	40

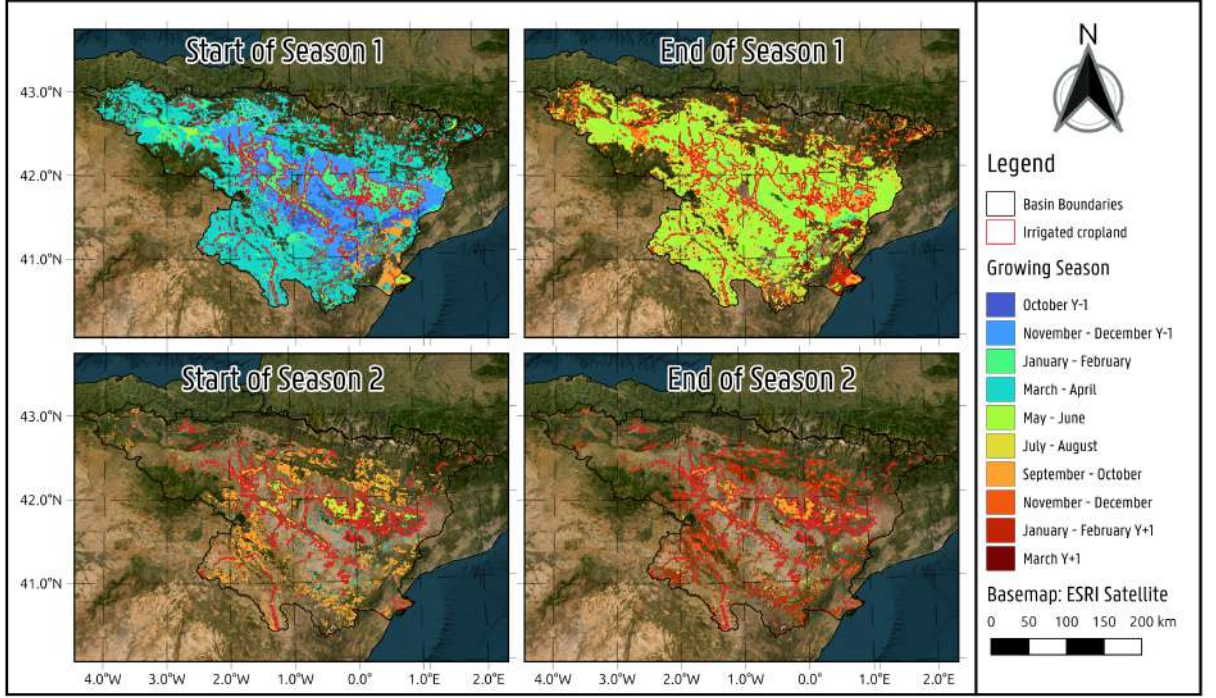


Figure 3.6: FAO Phenology Start and End of Season datasets used to flag irrigated areas with respect to their growing season. Irrigated areas are highlighted.

Calibration of WCM parameters is performed using OL GLEAM SM estimates, MODIS LAI and Sentinel-1 σ^0 observations for every individual grid-cell over the period 2016–2018 using Trust Region Reflective (TRF) least square optimization (Coleman & Li, 1996) with boundary and initial values of each parameter given in Table 3.3. Over the areas flagged as irrigated and that has a known crop calendar, two approaches have been examined to optimize the calibration of forward operator: (a) Calibrating excluding growing season, and (b) calibrating using all year round values. By employing these two different calibration methods, it is aimed to assess the performance and potential benefits of excluding the growing season during the calibration process. This comparison allows us to determine whether excluding the growing season, i.e., when irrigation considerably impacts SM, improves the DA framework.

3.4.3 Ensemble Kalman Filter

In this study, a 1-dimensional EnKF (Evensen, 1994) is used to update the GLEAM top-layer SM estimates. The 1-dimensional EnKF updates the top-layer SM in two steps: (a) forecast step, (b) analysis (i.e., update) step. First, model state ensembles, $\mathbf{x}_k^{i,f}$, are generated in the forecast step:

$$\mathbf{x}_k^{i,f} = \mathbf{SM}_1^{i,f} \quad (14)$$

where i indicates the ensemble member, f the model forecast, and k the time step. The ensemble mean of these states provides the SM estimate, and the spread of the ensemble members reflects the uncertainty associated. However, it has been shown that perturbations (Table

3.4) applied to the forcings mostly lead to the biased model estimates due to the non-linear processes involved during the calculations of SM (De Lannoy et al., 2006). The unintended perturbation bias is problematic because the model perturbations intended to generate ensemble states should ideally not impair the mean performance of the underlying model (Ryu et al., 2009). Therefore, a deterministic GLEAM (a single realization without perturbations) is calculated in parallel with the 32 realizations for every time step k to correct this unintended bias, as explained by Ryu et al. (2009). This single realization is then used to calculate the bias between deterministic state and mean ensemble states. The calculated bias is subsequently used for correcting each ensemble member ensuring the mean performance of the model is preserved.

$$\delta_t = \frac{1}{n} \sum_{i=1}^n (\mathbf{x}_k^{i,f} - \mathbf{x}_k^d) \quad (15)$$

where δ_t is the bias introduced by perturbation and \mathbf{x}_k^d is the deterministic SM state variable at time step k . Consequently, the bias introduced by perturbation in the ensemble members are corrected using δ_t as:

$$\tilde{\mathbf{x}}_k^{i,f} = \mathbf{x}_k^{i,f} - \delta_t \quad (16)$$

where $\tilde{\cdot}$ indicates the bias-corrected state variables. Then, the forward, i.e., observation, operator \mathbf{h}_k (WCM) is applied to transform the bias-corrected model states into observation space, resulting in the observation forecasts $\mathbf{y}_k^{i,f}$.

$$\mathbf{y}_k^{i,f} = \mathbf{h}_k (\tilde{\mathbf{x}}_k^{i,f}) \quad (17)$$

In the analysis step, each ensemble member, $\tilde{\mathbf{x}}_k^{i,f}$, is updated by calculating the innovation, i.e., the difference between the actual Sentinel-1 backscatter observations \mathbf{y}_k^{obs} and the observation forecasts $\mathbf{y}_k^{i,f}$:

$$\mathbf{x}_k^{i,a} = \tilde{\mathbf{x}}_k^{i,f} + \mathbf{K}_k [\mathbf{y}_k^{obs} - \mathbf{y}_k^{i,f}] \quad (18)$$

where \mathbf{K}_k is the Kalman gain, which maps innovations from the observation domain (dB) to the model state domain (m^3m^{-3}):

$$\mathbf{K}_k = \text{Cov} (\tilde{\mathbf{x}}_k^{i,f}, \mathbf{y}_k^i) [\text{Cov} (\mathbf{y}_k^{i,f}, \mathbf{y}_k^{i,f}) + \mathbf{R}_k]^{-1} \quad (19)$$

where \mathbf{R}_k is the observation error matrix, $\text{Cov} (\tilde{\mathbf{x}}_k^{i,f}, \mathbf{y}_k^i)$ is the covariance matrix between state and observation forecasts, and $\text{Cov} (\mathbf{y}_k^{i,f}, \mathbf{y}_k^{i,f})$ is the covariance matrix between observation forecasts. The observation error matrix, \mathbf{R}_k , has two parts: the measurement and representation error (Janjić et al., 2018). In this thesis, measurement error of Sentinel-1 SAR sensor

can be taken as negligible due to the up-scaling from 20m resolution to 1km resolution. The representative error is taken as Mean Square Error (MSE) between simulated and observed backscatter during the calibration process same as Rains et al. (2022). DA is only performed during the time steps when the soil is not frozen ($T_a > 2^\circ\text{C}$) and there is no snow on the ground (snow water equivalent (SWE) = 0) for time step k .

3.4.4 Ensemble generation

To represent the forecast error covariance, 32 ensemble members are generated. Each ensemble member is obtained by perturbing daily meteorological forcing data (i.e., T_a , R_n , and P) and model state variables (top-layer SM). Specifically, T_a is perturbed additively with a normal standard deviation of 1 (mean=0). R_n and P are perturbed multiplicatively, with R_n having a normal standard deviation of 0.3, while precipitation is lognormally distributed with a standard deviation of 0.3 to ensure positive precipitation values. This approach reflects that precipitation errors tend to scale with the magnitude of precipitation (Lievens et al., 2017a). Top-layer SM estimates are perturbed additively with a normal standard deviation of 0.04 at the end of each time step before DA. The daily perturbation details are summarized in Table 3.4.

Additive perturbations involve adding random noise to the forcing data, while multiplicative perturbations involve multiplying the data by a random noise factor. Perturbations for each forcing and state variable are generated daily independently, meaning they are not physically coherent with each other and are not spatially correlated.

Table 3.4: Forcing and state variable perturbation characteristics.

Variable	Unit	Standard deviation	Distribution	Perturbation Type
Precipitation	mm/day	0.3	Lognormal	Multiplicative
Net radiation	Wm^{-2}	0.3	Normal	Multiplicative
Air temperature	$^\circ\text{C}$	1	Normal	Additive
Top layer soil moisture	m^3m^{-3}	0.04	Normal	Additive

3.5 Experiment setups

To evaluate the ability of the DA procedure to account for irrigation on GLEAM SM and E estimates, three distinct experiments are designed:

1. **Control Experiment (OL):** GLEAM is run using solely P as input and no data assimilation is considered; therefore, SM and E estimates represent natural conditions without considering irrigation.
2. **Data Assimilation (DA)-A:** DA of Sentinel-1 backscatter is performed using the WCM calibrated based on OL SM estimates and LAI observations excluding the growing season, aiming to exclude potentially irrigated periods. This approach aimed to reduce the bias between GLEAM OL and Sentinel-1 backscatter that irrigation causes on SM during the growing season.

3. **Data Assimilation (DA)-B:** DA is performed using the WCM calibrated based on all-year OL SM estimates and LAI observations.

The OL run will serve as the control, providing a baseline for natural conditions without any DA while DA-A and DA-B experiments will be compared with OL to determine the improvements in SM and E estimates after DA. Moreover, outputs of DA-A and DA-B will be also inter-compared to evaluate the forward operator calibration optimization, providing insights into the effective calibration strategy for forward operators over irrigated areas.

In-situ SM time series will be used to evaluate the ability of the DA procedure to account for irrigation on SM estimates while the evaluation of E estimates will be relied on inter-comparison between three experiment due to the scarcity of *in-situ* E data over irrigated land (see Section 3.1).

4 Results and discussion

4.1 Evaluation of the forward operator

4.1.1 Calibration of Water Cloud Model

The boxplots in Figure 4.1 illustrate the calibrated parameters for different land cover types (based on CORINE land use classification of GLEAM grid-cell), specifically croplands, grasslands, and forests, while the spatial distribution of these calibrated parameters is shown in Figure 4.2. The land cover class "Irrigated cropland (A)" represents the calibrated WCM parameters when excluding the growing season, while "Irrigated cropland (B)" includes values from the calibrated parameters throughout the entire year.

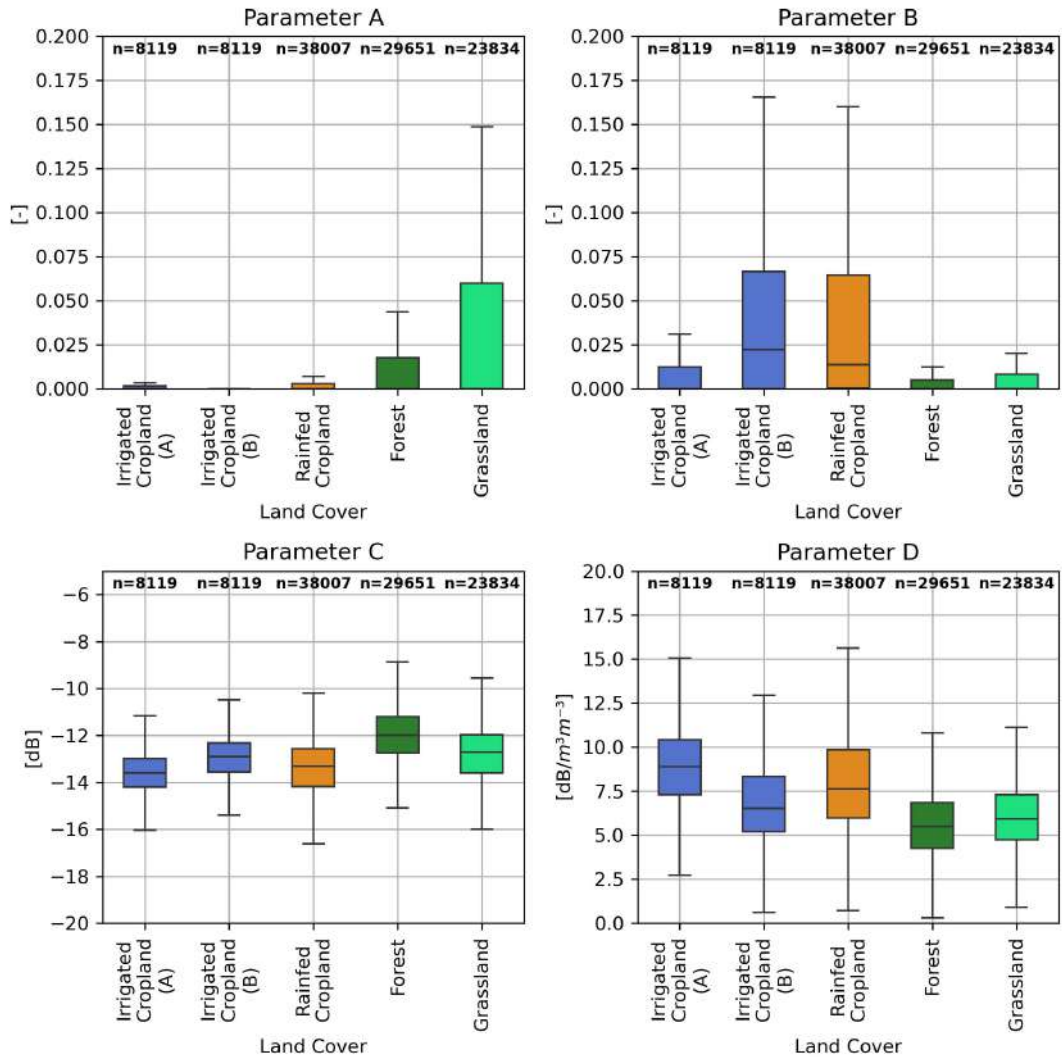


Figure 4.1: Fitted WCM parameter boxplots based on land cover type. The boxes represent the first (Q1) and third (Q3) quartiles, while the solid line within the box represents the median (second quartile; Q2). The whiskers of the boxplots represent values within the interquartile range (IQR; Q3–Q1) between Q1–1.5IQR and Q3+1.5IQR. Outliers are not shown. The number of grid-cell belonging to each land cover type is indicated at the top of the boxplots.

Parameter A , representing direct backscatter from the vegetation layer, remains close to 0.0 for all cropland types and is relatively higher for forests and grasslands, with values ranging from 0.0 (Q1) to 0.06 (Q3). The two different calibration strategies did not noticeably affect parameter A over irrigated areas. A notable difference among the land cover types is that parameter A tends to be skewed towards the lower boundary for forests and croplands, while it is more sparsely distributed for grasslands. Despite this sparse distribution for grasslands, the median for all land cover types remains close to 0.0.

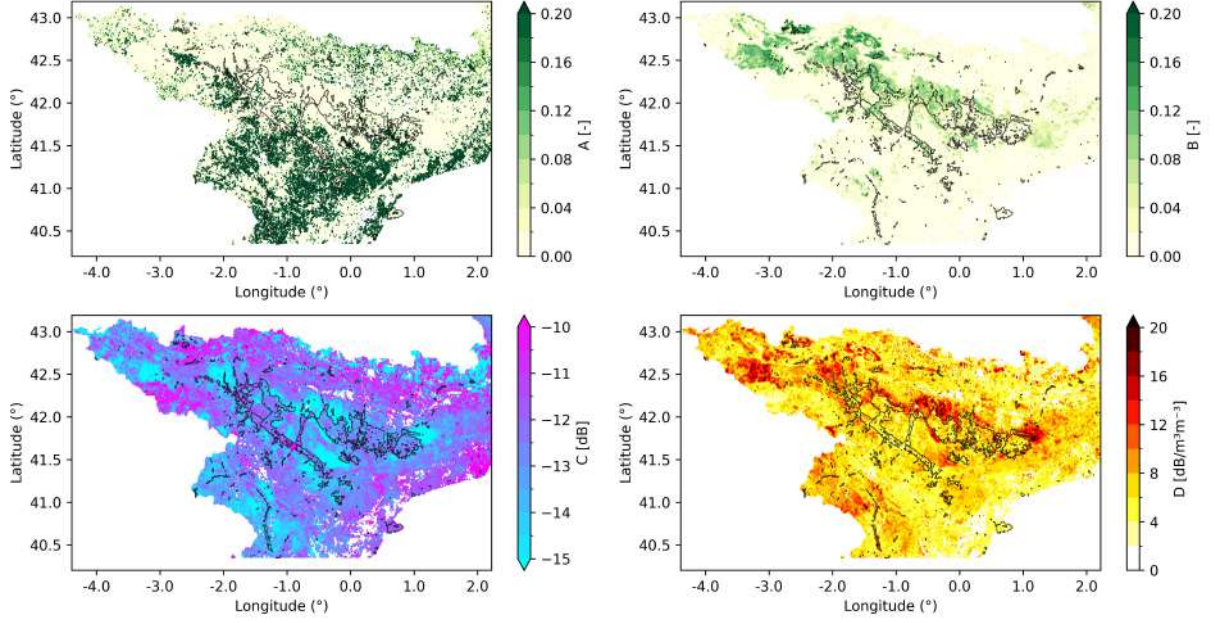


Figure 4.2: Fitted WCM parameters over the Ebro Basin. Highlighted areas represent irrigated croplands. Case B is shown for the highlighted areas.

Despite the fact that the temporal backscatter signature of cultivated crops is heavily influenced by the incidence angle of observations, the crop type, the crop growth stage, and the ground conditions (i.e., plowing, seeding, smoothing of the soil surface) (Veloso et al., 2017; Zhao et al., 2024), it can be said that attenuation by the vegetation layer is the dominant scattering mechanism over croplands (Arias Cuenca, 2023). Thus, the contribution to the total backscatter of the direct vegetation is either low or canceled out by the attenuation of soil backscatter over agricultural lands (Mattia et al., 2003), which may explain the low A parameter values. Moreover, croplands typically have a vegetation layer only during the growing season, while the off-season is usually characterized by bare soil due to harvesting. Consequently, the observed backscatter in croplands during the off-season is expected to be explained solely by bare soil scattering parameters, as vegetation simply does not exist for a considerable amount of time during the year. In contrast, forests and grasslands maintain a vegetation layer throughout the year, substantially influencing the observed backscatter and resulting in higher values for parameter A (Liu & Shi, 2016).

In contrast to parameter A , parameter B , representing the backscatter attenuation by the vegetation layer, varied substantially for both calibration strategies and across different land cover types. While parameter A was higher over forests and grasslands compared to croplands, the

attenuation parameter B is higher over croplands. The influence of excluding the growing season over irrigated areas can also be seen in parameter B . Excluding the growing season signals during calibration resulted in lower values close to 0.0, whereas including the growing season resulted in relatively higher values (median = 0.022). It is also noted that including the growing season for irrigated cropland yielded parameter B values similar to those of rainfed cropland (median = 0.014). Due to the same reason explained above, the dominant role of vegetation attenuation in the scattering during the growing season is reflected with higher fitted B values over agricultural areas. This can be said to be expected as it has been shown that cultivated vegetation substantially alters backscatter during the growing season (Arias Cuenca, 2023; Yadav et al., 2019). This inference is further supported by comparing experiments that exclude the growing season, which yielded much lower (almost 0.00) values for parameter B , to those that include the growing season, where fitted parameter B values increased considerably. In conclusion, it can be said that by omitting the vegetation season during the calibration of the vegetation-related parameters (A and B), one cannot expect accurate estimates for those parameters as both parameters tend to be close to 0.0.

The parameter C , related to surface roughness, and its fitted range appear to be relatively similar across different land cover types, with higher values observed in forests (median=-11.98 dB) and the lowest values in irrigated croplands (A) (median = -13.6 dB). For the parameter D , sensitivity of backscatter to the changes in the SM, there are marked differences between land cover types. Backscatter over rainfed and irrigated croplands appears to be the most sensitive to changes in SM (rainfed cropland median=7.62 dB/m³m⁻³) compared to forest (median=5.48 dB/m³m⁻³), grassland (median=5.93 dB/m³m⁻³), and irrigated cropland (median=6.55 dB/m³m⁻³ for case (B)). Additionally, the dispersion of fitted parameters is higher in croplands compared to forests and grasslands, as observed in the interquartile range (IQR) of the box-plots. Higher sensitivity of backscatter over croplands compared to grassland and forest was not expected as it has been shown by Yadav et al. (2019), the backscatter sensitivity to SM decreases over croplands as the attenuation of the soil backscatter becomes the main scattering mechanism.

Figure 4.2 illustrates the spatial distribution of calibrated WCM parameters for case B. The spatial distribution of parameters C and D highlights a notable pattern indicating an inverse relationship: high values of parameter D are consistently found in regions where parameter C is low, and vice versa. In theory, for similar soil texture and surface roughness, similar values for C and D should be obtained over space as these account for the theoretical sensitivity of backscatter to SM (Ulaby, 1974). However, in reality, the impact of vegetation cover on backscatter should then be accounted for by parameters A and B , weighing direct vegetation scatter and attenuation. Then, regions with lower SM sensitivity due to significant vegetation cover (note the low D values over irrigated areas in Figure 4.2) often feature higher values for parameter C and low values for D .

Additionally, the spatial distribution of the differences in fitted WCM parameters for DA-A and DA-B is shown in Figure 4.3. This figure indicates that the majority of grid-cells exhibit

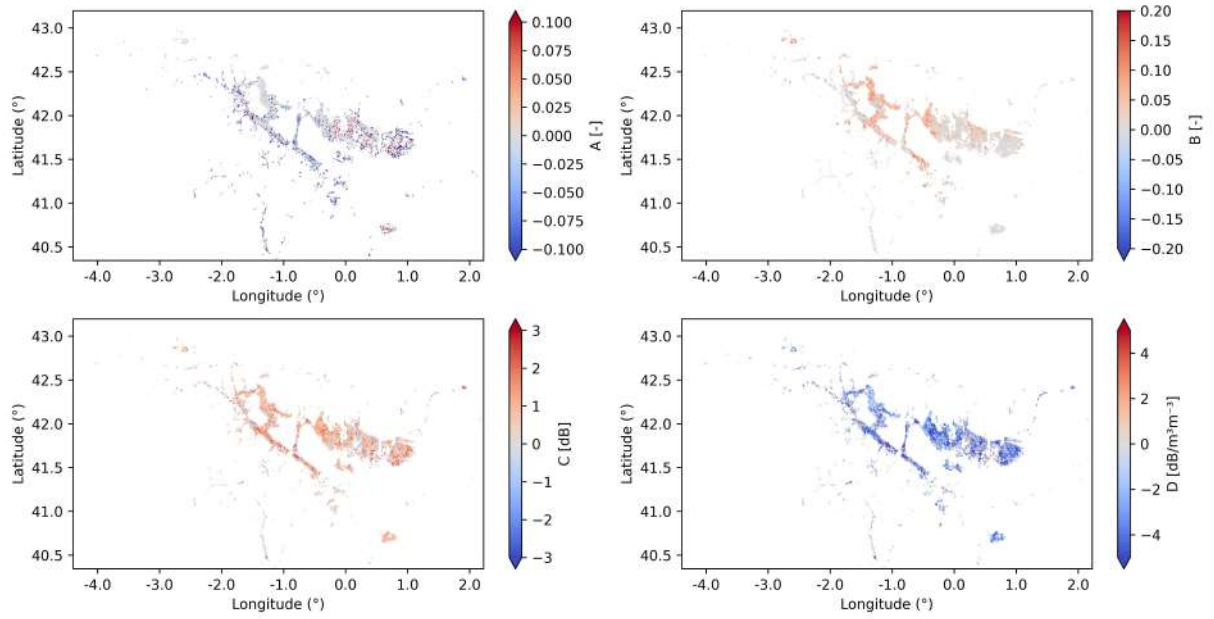


Figure 4.3: Difference in the fitted WCM parameters. The differences in parameters are presented as Case B minus Case A.

a consistent difference for C and D parameters while the differences in A and B are less noticeable.

4.1.2 Backscatter simulations

Firstly, it should be noted that the comparison between Sentinel-1 and DA backscatter is performed based on the mean ensemble values of simulated backscatter. In this study, the calibrated WCM parameters enabled the forward simulation of ensembles of backscatter, which were then used in the DA-A and DA-B experiments. The left side of Figure 4.4 demonstrates the performance of the forward operator used during the DA-B experiment, while the right-hand side illustrates the performance difference between the DA-A and DA-B experiments over the irrigated areas. The mean R over the entire study area is 0.616 for DA-A and 0.618 for DA-B, respectively, which is higher than the results of Rains et al. (2022), who obtained a mean R of 0.44 over European SM sites. Moreover, the mean Root Mean Square Error (RMSE) over the whole study area is 0.621 dB and 0.617 dB for DA-A and DA-B, respectively, which is slightly lower than the results of Rains et al. (2022), who obtained a mean RMSE of 0.73 dB over European SM sites. Pre-processing steps applied, such as filtering the pixels that are not in agreement with ERA5-Land top layer SM and the DGU method for up-scaling high-resolution Sentinel-1 backscatter data, may have contributed to the enhanced performance reported in this thesis. Furthermore, it can be seen that including the growing period during the calibration improves the performance of the forward operator, yielding a higher temporal correlation and lower RMSE between simulated and observed backscatter. The mean decrease in temporal correlation and increase in RMSE over irrigated areas are 0.027 (-) and 0.052 dB, respectively.

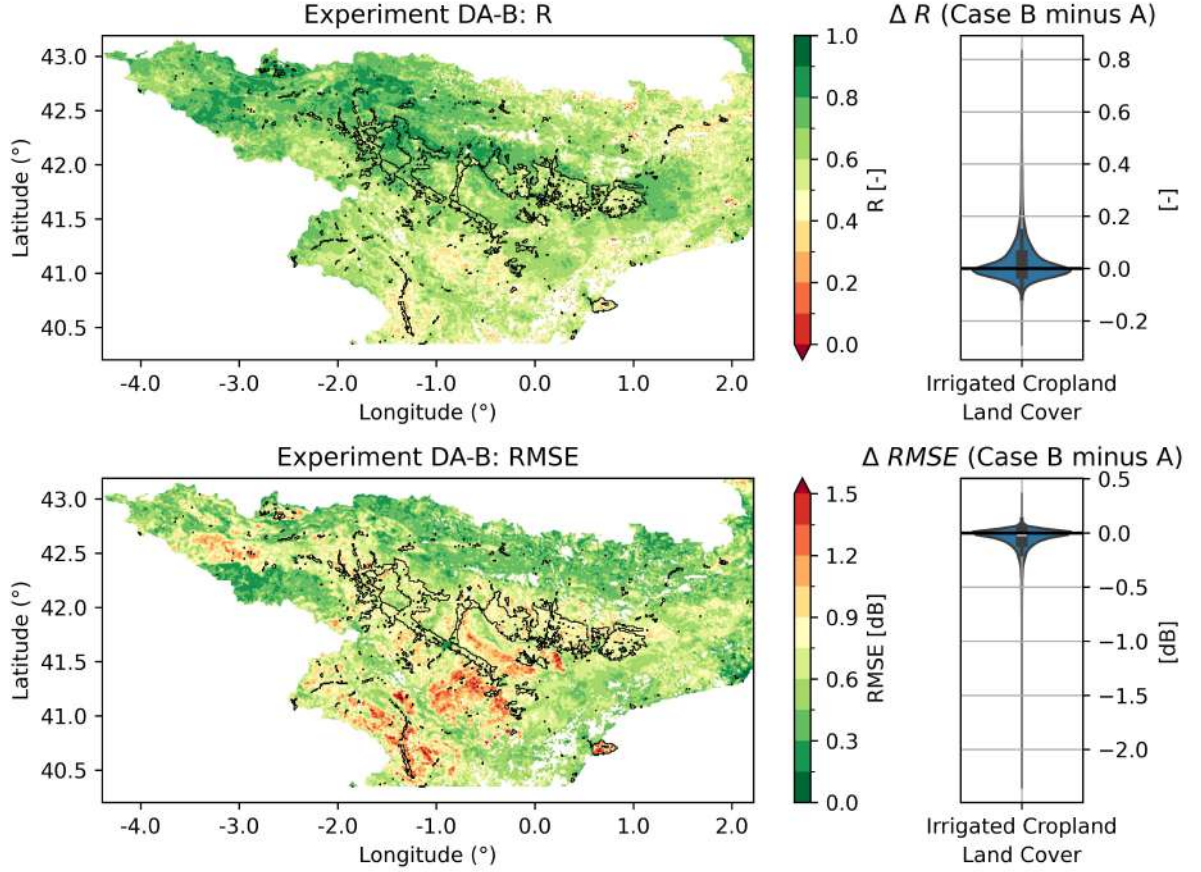


Figure 4.4: (left) Temporal correlation and RMSE of simulated backscatter over the Ebro Basin for DA-B. (right) The difference in performance between two DA experiments. Irrigated areas are highlighted.

A detailed comparison between land cover types and a summary of the backscatter simulation evaluation can be seen in Table 4.1 and Figure 4.5, and it can be seen that temporal correlations also vary between land cover types. The highest RMSE values are associated with croplands (rainfed cropland mean RMSE = 0.75 dB), while the lowest RMSE values correspond to forests (mean RMSE = 0.46 dB). Additionally, rainfed croplands show higher correlation with a mean R of 0.65, and forested areas show the lowest values with a mean R of 0.59 for the assimilation period 2016–2021. Previous studies have highlighted that backscatter over densely forested areas tends to saturate over time due to small changes in vegetation conditions, leading to low signal variability and thus easier to model mathematically (indicated by lower RMSE over forested areas) (Arellano et al., 2019; Lievens et al., 2017a). The mechanism behind this is usually that the model fits a good C with low D and A parameters, which lowers the RMSE between simulated and observed backscatter (see Appendix A). Furthermore, low R values over forested areas may indicate that the forward operator cannot reproduce the vegetation component of the backscatter as well as the soil backscatter part, despite the constant stable backscatter (compared to more complex $\sigma^0 = \sigma_{veg}^0 + t^2 \sigma_{soil}^0$).

The long-term mean of observed and simulated backscatter over the Ebro Basin and the difference between simulated backscatter from two DA experiments for the evaluation period

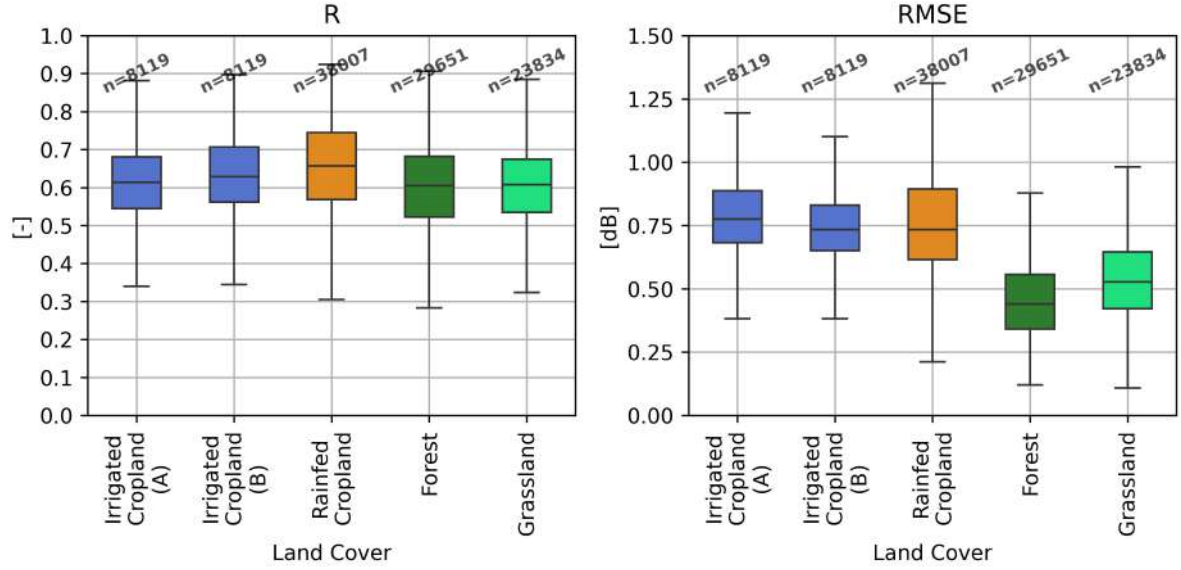


Figure 4.5: Boxplots of temporal correlation and RMSE between simulated and observed backscatter by land cover type. The number of grid-cells belonging to each land cover type is indicated at the top of the boxplots.

Table 4.1: Detailed comparison of backscatter simulations over different land cover types.

Land Cover	Mean R [-]	Mean RMSE [dB]
Irrigated Cropland (A)	0.60	0.80
Irrigated Cropland (B)	0.63	0.75
Rainfed Cropland	0.65	0.77
Forest	0.59	0.46
Grassland	0.60	0.55

2016–2021 is given in Figure 4.6. It should be noted that plotted simulated long term mean backscatter is calculated only using time steps that DA took place. The overall bias (Sentinel-1 observations minus WCM forecasts, also called increments) for experiment DA-A and DA-B is -0.094 dB and 0.002 dB over irrigated areas, respectively. This indicates that excluding the growing season during the calibration of the forward operator yields a more biased DA output for simulated backscatter. The difference plot has also highlighted the spatial distribution of the bias of DA-A over irrigated areas, indicating DA-A is mostly biased positively (the difference between DA-B and DA-A is negative, meaning higher backscatter values for DA-A, given the relatively unbiased DA-B).

Moreover, Figure 4.7 illustrates the spatial distribution of the ensemble standard deviations averaged over the period 2016–2021 (i.e., an indicator of observation forecast variability) for DA-B. Table 4.2 presents observation forecast variability based on different land cover types. A detailed analysis based on land cover reveals differences between land cover types, with forests and grasslands associated with lower forecast variability (0.16 and 0.18 dB, respectively), while irrigated and rainfed croplands have higher forecast variability (mean = 0.22 and 0.26 dB, respectively). In a previous study by Lievens et al. (2017a), where GLEAM was coupled with

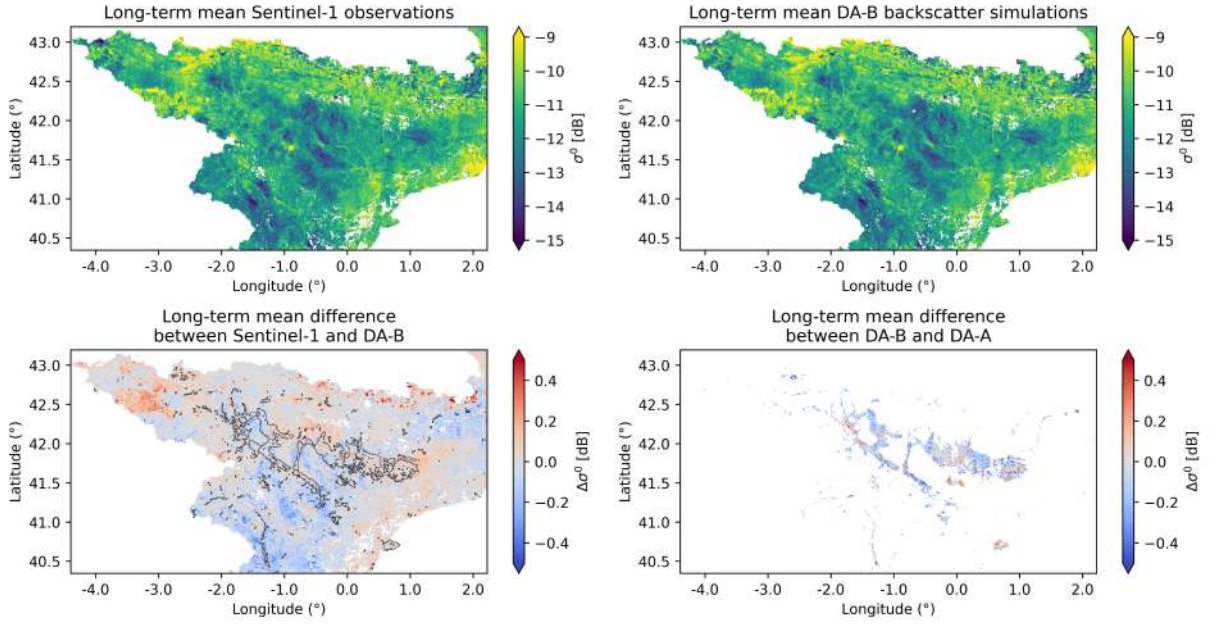


Figure 4.6: Long-term mean Sentinel-1 observations and DA-B simulations over the Ebro Basin, as well as the difference between them. The difference between simulated backscatter from the two DA experiments is also provided.

WCM to simulate ASCAT σ^0 , the variability associated with σ^0 forecasts was fairly homogeneous over vegetated parts of the globe, around 0.3–0.4 dB. However, it should be noted that the differences in forecast variability between the studies may be influenced by how the forcings and state variables are perturbed, which ultimately affects the model state estimates and thus the observation forecasts. In the study by Lievens et al. (2017a), LAI observations were perturbed daily, whereas in this study, top layer SM estimates were perturbed daily (See Table 3.4). Specifically, perturbing LAI observations may be the reason for the higher variability over vegetated areas in the study by Lievens et al. (2017a) compared to this study.

Table 4.2: Detailed comparison of the observation forecast variability for different land covers.

Land Use	Observation forecast variability [dB]
Irrigated Cropland (DA-A)	0.27
Irrigated Cropland (DA-B)	0.22
Rainfed Cropland	0.26
Forest	0.16
Grassland	0.18

4.2 Evaluation of data assimilation impact on soil moisture and evaporation estimates

Firstly, it should be noted that the comparison between *in-situ* SM, OL, DA-A, and DA-B experiments is performed based on mean ensemble values of E and SM. In presenting the results, it's important to note that both DA experiments (DA-A and DA-B) yielded identical outcomes

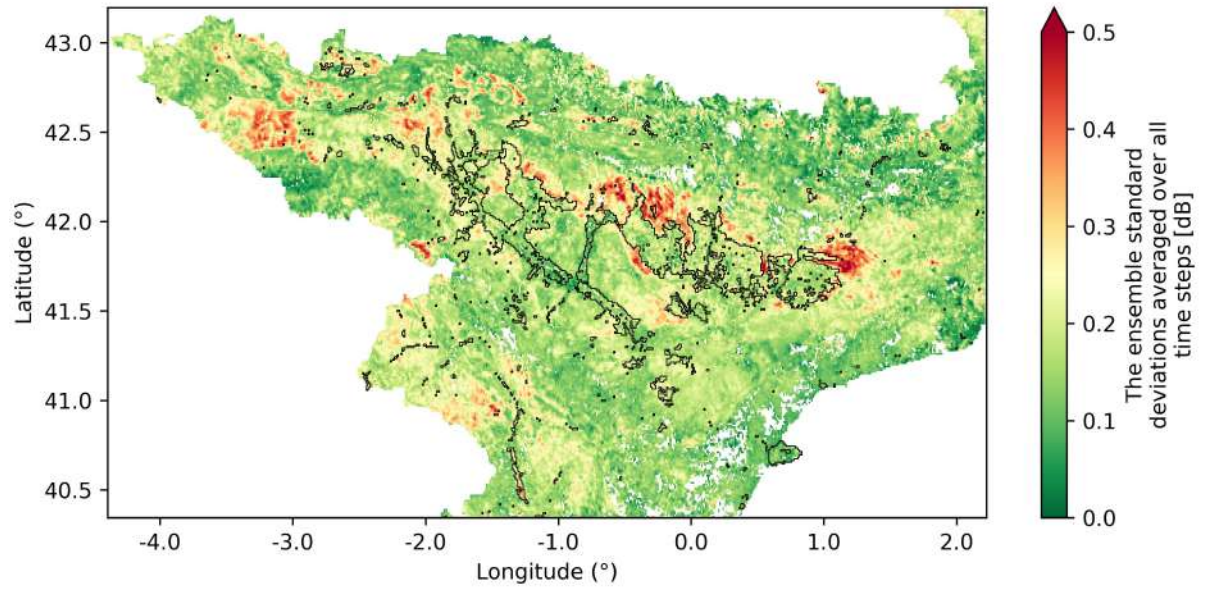


Figure 4.7: Spatial distribution of ensemble standard deviations averaged over the period 2016–2021 for DA-B. Irrigated areas are highlighted.

across grasslands, forest, and rainfed cropland, thus distinctions between the experiments will only be specified for irrigated cropland (as DA-A and DA-B).

4.2.1 Basin-scale soil moisture and evaporation simulations

The top panel of Figure 4.8 illustrates long-term (2016–2021) seasonal potential E estimates for the Ebro Basin, calculated using the Priestley-Taylor equation from GLEAM. The bottom panel presents boxplots highlighting the long-term seasonal differences in evaporative demand. It is evident that the JJA (June-July-August) and MAM (March-April-May) seasons are characterized by high evaporative demand, whereas the DJF (December-January-February) and SON (September-October-November) seasons exhibit low evaporative demand.

Figure 4.9 illustrates the long-term SM and E estimates from the OL and DA-B experiments, with the irrigated areas contoured in black on the maps (see Appendix B for DA-A). The left side of the figure shows the long-term SM and E estimates, while the right side displays the long-term DA SM and E anomalies relative to OL (for DA-B). Over the central part of the Ebro Basin, characterized by dry climatic conditions (see Section 3.1), SM anomalies are generally positive, indicating wetter soil compared to OL natural conditions (derived using solely precipitation). In contrast, the mountainous areas surrounding the central valley exhibit drier average SM conditions in the DA experiment compared to OL conditions, indicated by negative anomalies. Positive SM anomalies in the central part of the valley are also reflected in the total annual E estimates, with differences reaching up to $+60 \text{ mm year}^{-1}$. However, areas with negative SM anomalies do not show a substantial decrease in total annual E. The highlighted irrigated areas demonstrate that SM conditions, derived solely from precipitation in the OL experiment, are dry. In contrast, the DA experiment reveals wetter SM conditions in these areas.

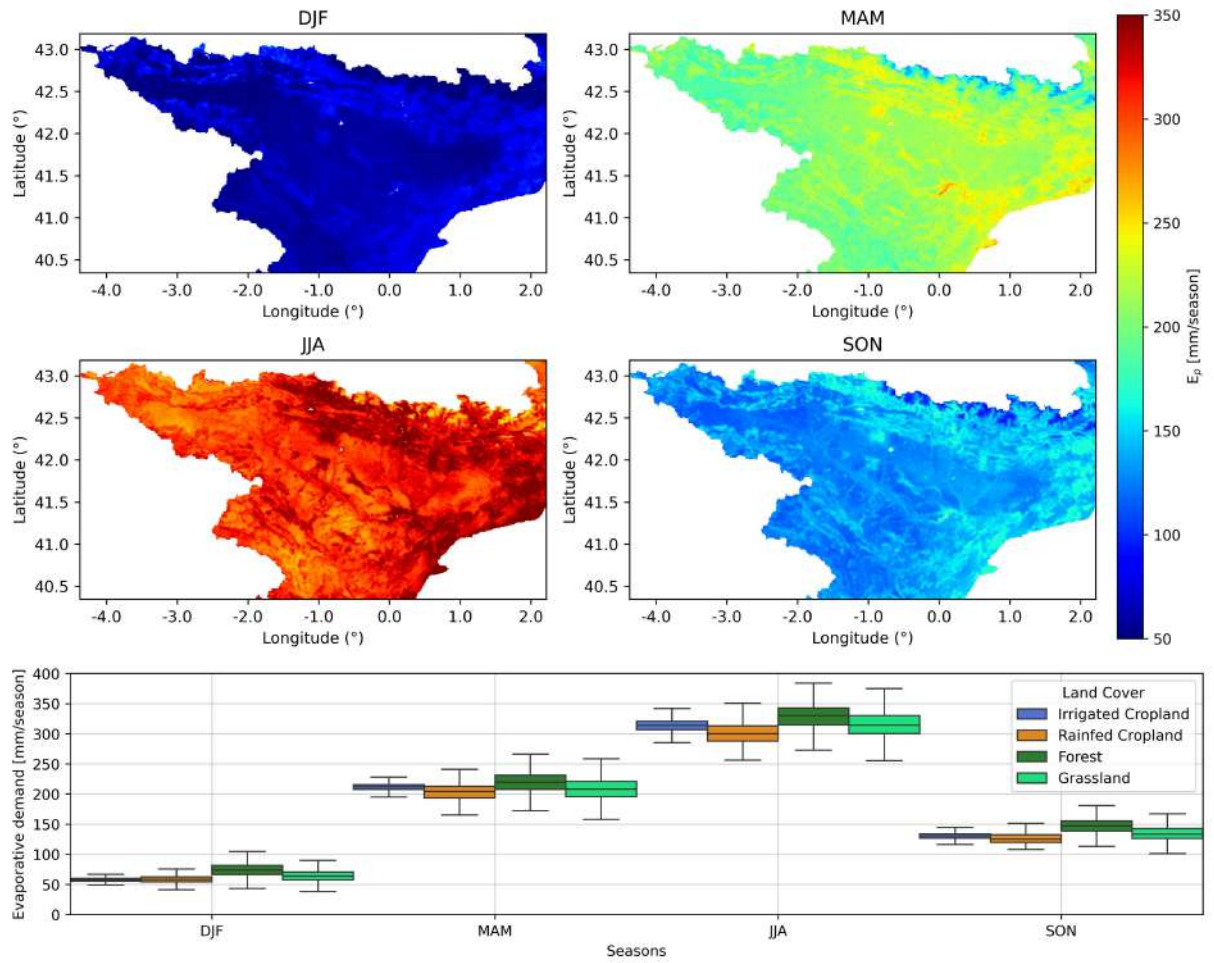


Figure 4.8: (top) Long-term (2016–2021) seasonal E_p estimates over the Ebro Basin as derived from GLEAM, (bottom) boxplots of long-term (2016–2021) seasonal evaporative demand estimates categorized by land cover type.

Figure 4.10 depicts the boxplots of total simulated E estimates for OL, DA experiments. The bottom panel of Figure 4.10 shows that forest land cover types have the highest total annual E (OL mean: 610 mm year^{-1} , DA mean: 625 mm year^{-1}), while irrigated croplands have the lowest (OL mean: 475 mm year^{-1} , DA-B mean: 505 mm year^{-1}). For all land cover types, DA increased the total annual E . The annual impact is higher for irrigated areas (case B) with a 5.9% increase (mean increase of 28.2 mm/year), compared to forested areas with only a 2.4% increase (mean increase of 14.4 mm/year). Despite both DA experiments resulting in an increase in total annual E over irrigated areas, the increase in the DA-B experiment is more pronounced compared to the DA-A experiment (mean increase DA-B: $28.2 \text{ mm year}^{-1}$, mean increase DA-A: $18.6 \text{ mm year}^{-1}$). The decreased impact of DA-A can be attributed to the low performance of the WCM used in the experiment (see Section 4.1.2), with further details will be inspected in the following parts of this section.

The top row of Figure 4.11 illustrates the differences in SM (m^3m^{-3}), while the bottom row shows the differences in daily E (mm day^{-1}) between experiments (DA minus OL estimates). Moreover, Figure 4.12 highlights the difference between the DA impact on SM and E for JJA

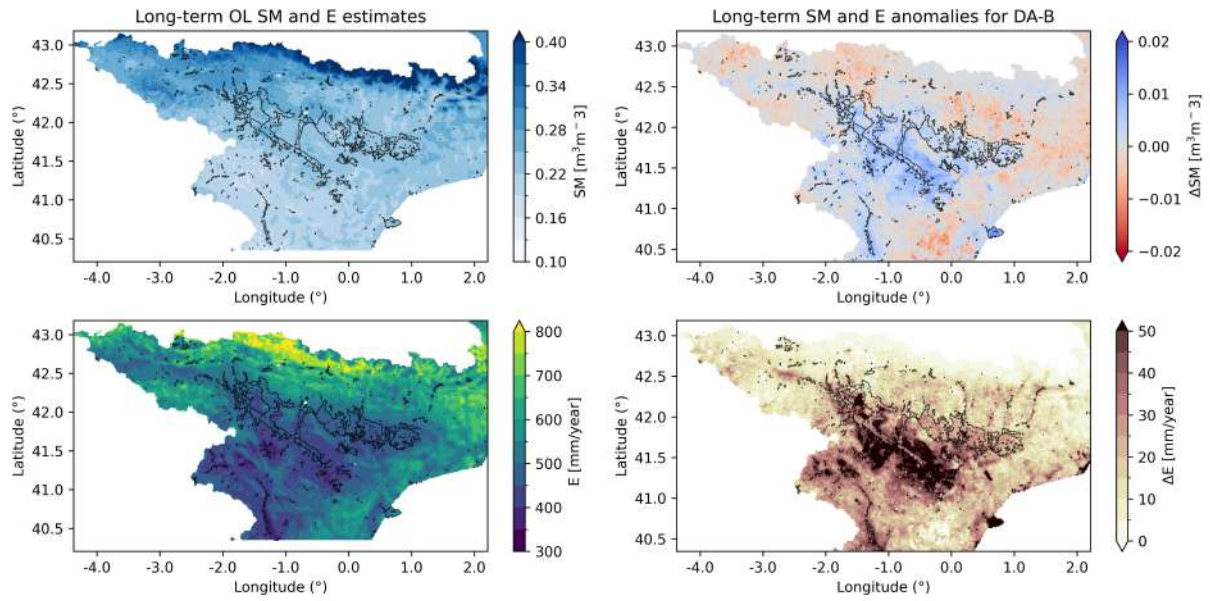


Figure 4.9: (left) Long-term (2016–2021) mean SM and total annual E estimates over the Ebro Basin from GLEAM OL run, (right) long-term (2016–2021) anomalies of DA-B with respect to OL run. Irrigated areas are highlighted.

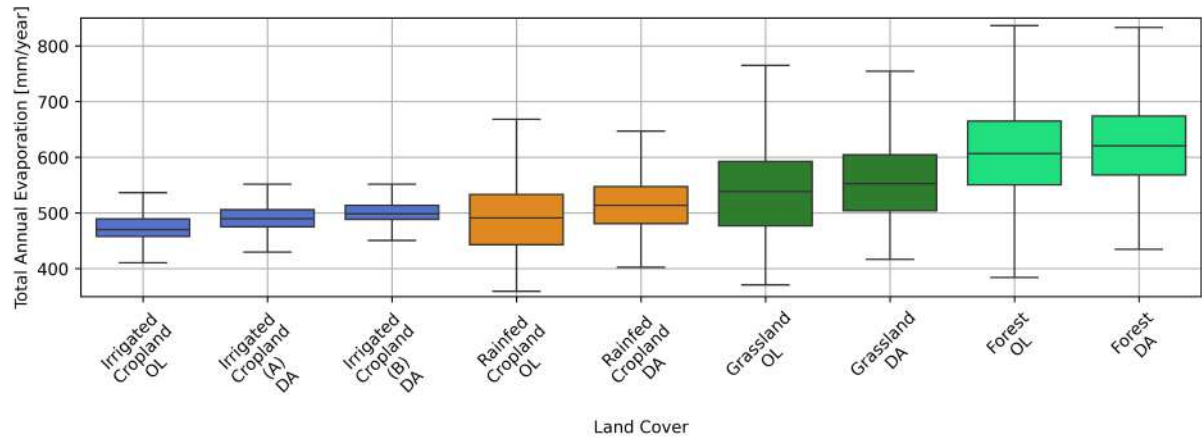


Figure 4.10: Simulated GLEAM total annual E boxplots from different experiments based on land cover type.

and MAM. It can be seen from Figure 4.12 that during MAM, the DA impact on SM is more towards drier soil, while the impact in JJA is more toward wetter soil for most of the basin. This difference also alters the total seasonal E in JJA, while the influence on E during the MAM months is low.

A detailed analysis per land cover type in Figure 4.11 also reveals that forest land cover type SM anomalies is closer to OL conditions for all seasons compared to other land cover types. This difference in SM anomalies based on the land cover type is also reflected in the total annual E estimates where DA for forest areas resulted in the smallest mean increase of $14.44 \text{ mm year}^{-1}$ or 2.37% compared to OL experiment. Notably, Figure 4.12 and Figure 4.11 highlight that during JJA (June-July-August), the differences in SM between DA and OL are more pronounced over all land cover types, with DA exhibiting higher values than OL compared to other seasons. This is also reflected in the difference in modelled daily and seasonal E DA-experiments, which are

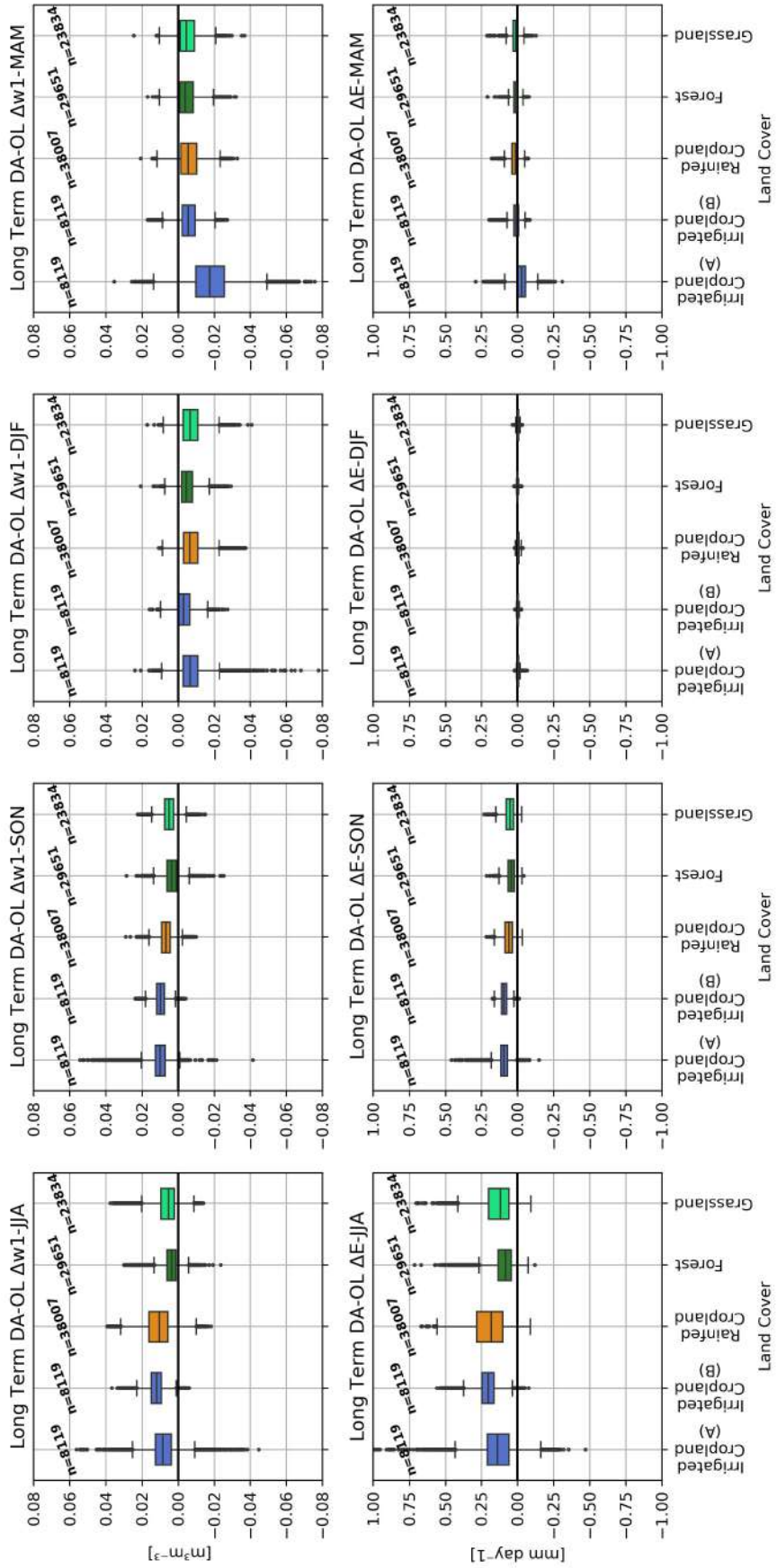


Figure 4.11: DA impact on SM and E estimates with respect to OL. Outliers are shown. The number of grid-cells that belongs to each land cover is indicated on top of the boxplots.

consistently higher for all land cover types during JJA compared to the OL run. Although the anomalies in SON (September-October-November) are positive, the impact on E estimates are relatively less pronounced. In contrast to JJA and SON, during DJF and MAM, the anomalies are generally negative for all land covers. However, this is not reflected in the E estimates, as these months are typically characterized by limited energy availability rather than water availability, which constrains E processes externally and SM conditions are not main driver of E (see Figure 4.8).

The encircled area in Figure 4.12 corresponds to the Ebro Delta, where rice cultivation predominates. During JJA, the Ebro Delta receives minimal precipitation (4–58 mm), coinciding with the most water-demanding phase of the rice growth cycle, necessitating substantial irrigation by farmers (Gómez de Barreda et al., 2021). The OL estimates, shown in the left panels, reflect dry SM conditions and low total seasonal E. In contrast, the right panels illustrate the substantial impact of DA during these months (for the case of DA-B), with cumulative JJA E reaching up to +60 mm.

Another interesting observation extracted from Figure 4.11 is the pronounced difference in DA impact between DA-A and DA-B during the MAM season over irrigated areas, coinciding with the growing season cycle (see Figure 3.6). To evaluate the differences between the two DA approaches, mean SM and daily E differences were calculated over each irrigated grid-cell's respective growing season which is shown in Figure 4.13. During the growing season, it is assumed that farmers irrigate, leading to higher SM estimates in reality compared to the OL run, which represents solely natural conditions. Thus, DA with Sentinel-1 should increase SM values by capturing the influence of irrigation. The results highlight that SM and daily E estimates are higher during the growing season, suggesting that the DA-B approach captures more effectively the influence of irrigation on SM and E compared to the DA-A approach. Therefore, it can be said that the potential benefit of excluding the growing season is not there (see Section 3.4.2), due to errors in the calibration of vegetation influences in WCM.

To showcase why DA-A yielded worse performance than expected (See Section 3.4.2), the time series of a selected irrigated cropland grid-cell with a defined growing season is plotted in Figure 4.14. The illustration of WCM function for the two sets of parameters is shown in Figure 4.15. It can be from Figure 4.15 that excluding the growing season during the calibration ended up with higher vegetation backscatter parameter A and lower attenuation parameter B for this particular grid-cell. from Figure 4.14. This means that increase in LAI will increase the simulated backscatter as vegetation backscatter component (σ_{veg}^0) will be more substantial than vegetation attenuation (t^2) as can be seen from Figure 4.15. However, it should be noted that the quality of the calibrated A and B parameters for the experiment without the growing season can be questionable as there might be few data points with vegetation for model to learn vegetation behaviour properly.

It can be seen from Figure 4.14, LAI observations increase due to the increase in vegetation at the beginning of each growing season. Overall, the SM and E estimates from different DA and OL experiments generally follow the same pattern except during the growing season and

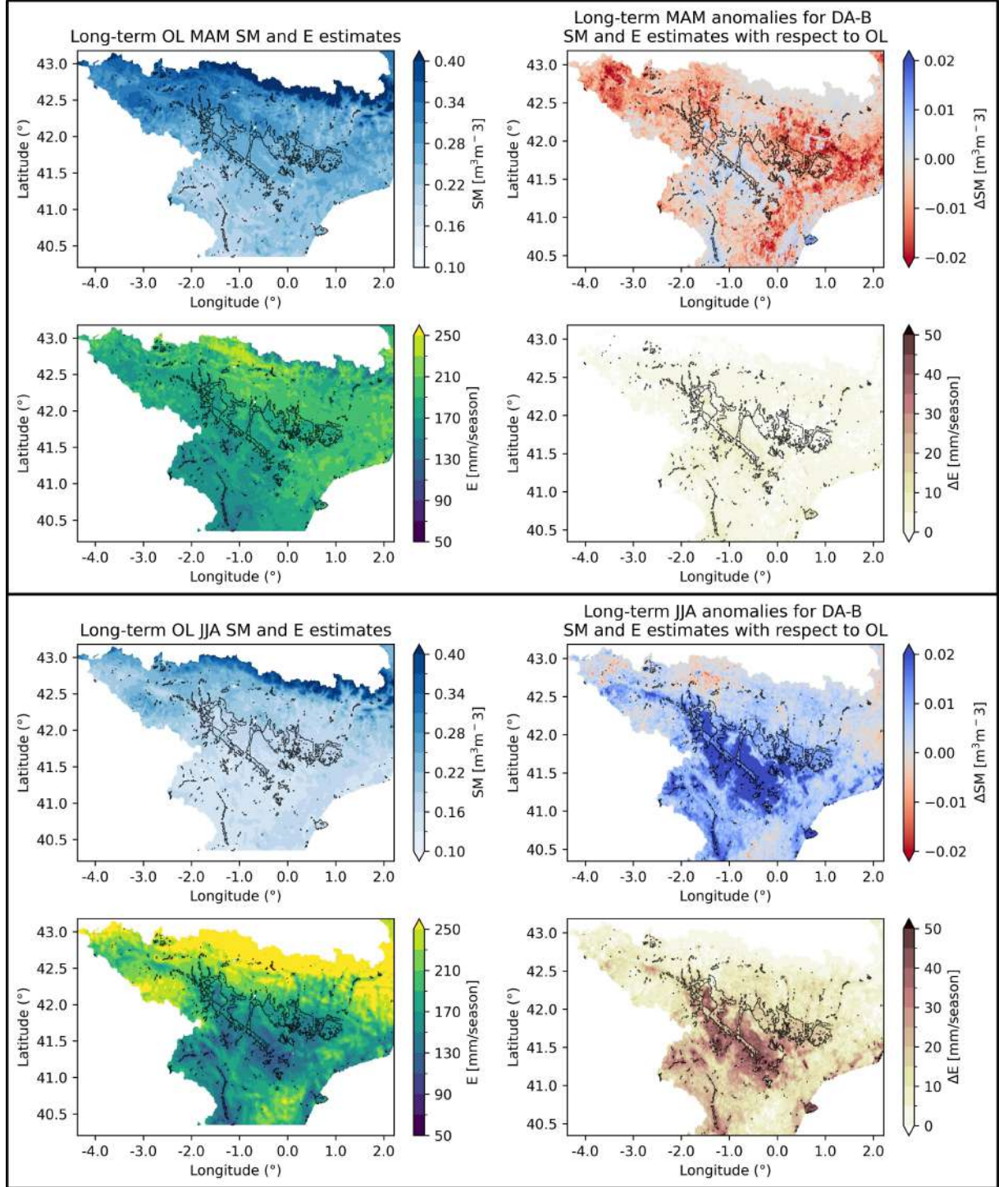


Figure 4.12: (top) MAM season, (bottom) JJA season, (left) GLEAM OL SM and E estimates, (right) DA-B anomalies with respect OL run. Irrigated areas are highlighted.

JJA season. Both DA experiments show continuously wetter SM conditions during the summer, with DA-B showing wetter SM conditions compared to DA-A during the growing season. As seen in Figure 4.14, LAI observations start to increase at the beginning of each growing season due to changing vegetation conditions. The difference between the two approaches is that DA-A's WCM attributes the increase in LAI to direct vegetation scatter (σ_{veg}^0), while DA-B's WCM attributes the increase in LAI to the attenuation parameter (t^2) to suppress the soil

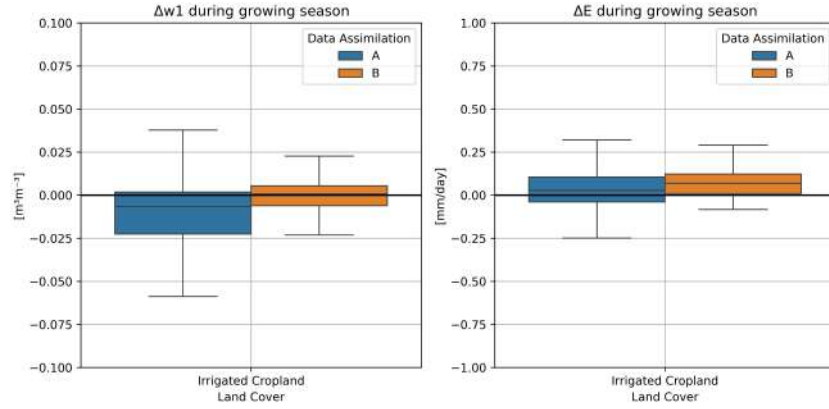


Figure 4.13: DA and OL difference on SM and E estimates during growing season over irrigated areas.

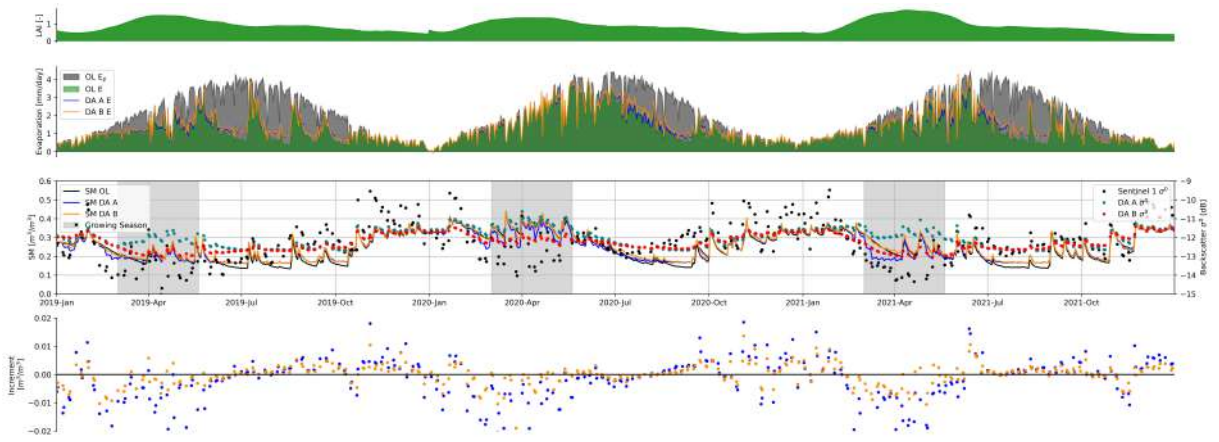


Figure 4.14: Example time series (2019–2021) from an irrigated grid-cell. (top) LAI observations, (middle) OL and DA SM and daily E estimates as well as the the simulated and observed backscatter, (bottom) daily SM increments to the GLEAM top layer soil moisture. Selected grid-cell longitude: -1.21 latitude: 41.85

backscatter (σ_{soil}^0) which lead to increase in simulated σ^0 for DA-A and decreased σ^0 fro DA-B. This difference leads to a difference between observed and simulated σ^0 for DA-A, causing increasingly negative increments to daily SM conditions as can be observed in the bottom panel of Figure 4.14. It should also be noted that this selected grid-cell is atypical case considering the trend that is observed in difference in fitting parameters in Figure 4.3. More specifically, it was shown that exclusion of growing season mostly yielded to a lower vegetation attenuation parameter B which is not the case for this case.

An another interesting time series of a selected irrigated cropland grid-cell with a defined growing season is presented in Figure 4.16. The illustration of WCM function for the two sets of parameters is shown in Figure 4.17. It can be seen that including the growing season during the calibration (DA-B) decreased the backscatter sensitivity to the SM parameter D substantially. This can be explained by the fact that if the growing season is included in the calibration, there will be a substantial number of data points that soil backscatter is attenuated by the crop as attenuation is the mostly the main scattering mechanism during the growing period. Thus, the calibration of the D parameter will yield to a lower value. Especially, the difference between the fitted value of D for two calibration approaches is high for this particular grid cell

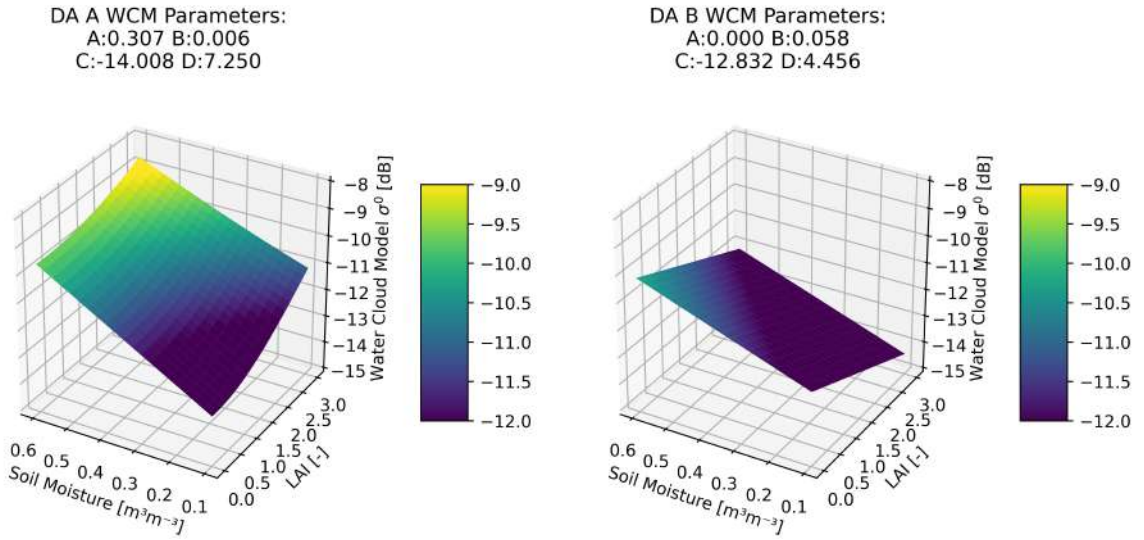


Figure 4.15: Relationship of SM and LAI with simulated backscatter based on different WCM parameterization. Parameters are from the same grid-cell in Figure 4.14. Selected grid-cell longitude: -1.21 latitude: 41.85

(see Figure 4.3) as it has two growing seasons, so most of the data points were masked during the calibration of WCM-A. High sensitivity to SM for the case DA-A then resulted in higher increments during the growing season. It is demonstrated that excluding the growing season led to incorrect vegetation parameters, A and D , and DA-A also led to more biased DA output. We can see that especially during the growing season, when vegetation dominates the scattering mechanism, SM estimates from DA-A experiments deviate notably compared to OL and DA-B experiments. It can also be seen that the DA impact on SM during the two growing periods (in the same year) is different: during the first growing season, SM increments are mostly negative, while during the second growing season, increments are mostly positive. Even though more detailed analyses are required to determine whether this is related to real SM conditions, irrigation practices, or poor parametrization of the vegetation component of WCM, it can be said that the DA-B approach is less subjected to potentially incorrect increments.

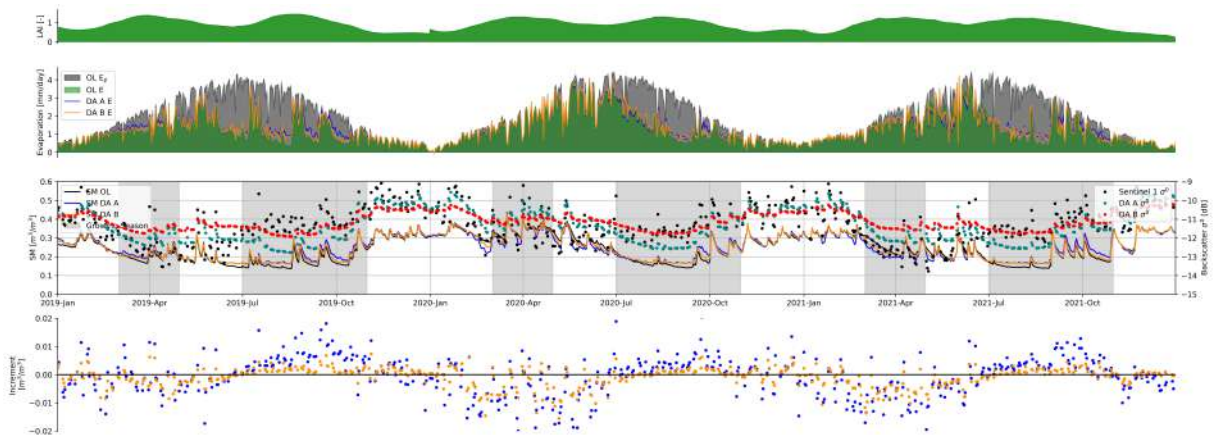


Figure 4.16: Example time series (2019–2021) from an irrigated grid-cell. (top) LAI observations, (middle) OL and DA SM and daily E estimates as well as the the simulated and observed backscatter, (bottom) daily SM increments to the GLEAM top layer soil moisture. Selected grid-cell longitude: -1.45 latitude: 41.96

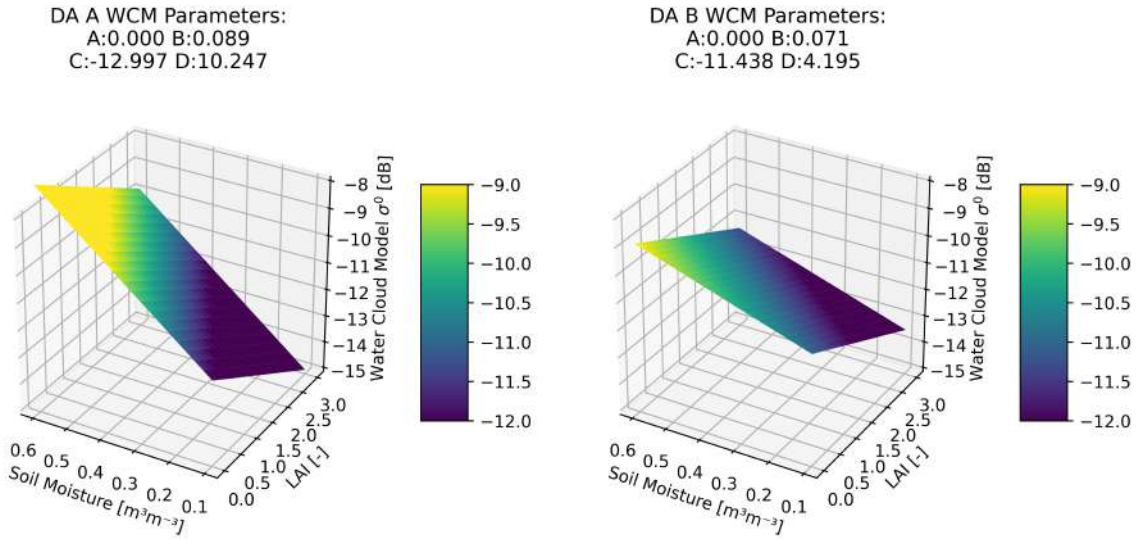


Figure 4.17: Relationship of SM and LAI with simulated backscatter based on different WCM parameterization. Parameters are from the same grid-cell in Figure 4.16. Selected grid-cell longitude: -1.45 latitude: 41.96

4.2.2 In-situ comparison

The DA impact of Sentinel-1 backscatter into GLEAM to improve the SM and E estimates is assessed by comparing the daily *in-situ* SM time series with OL and DA runs. The details of the results of both OL and DA is presented in Table 4.3.

Table 4.3: Temporal correlation of daily *in-situ* SM with OL and DA experiment SM estimates.

Network	Station	Land Cover	Depth(m)	R OL [-]	R DA [-]	ΔR [-]
IPE	Aguero	Forest	0.06	0.783	0.795	0.013
	Penaflor	Shrubland	0.10	0.681	0.653	-0.028
XMS-CAT	ClotdelesPeresI	Cropland-rainfed	0.05	0.818	0.794	-0.025
	ClotdelesPeresII	Cropland-rainfed	0.05	0.844	0.869	0.025
	SerradeCostaAmpla	Cropland-rainfed	0.05	0.737	0.742	0.005
	RiberadeSio	Cropland-irrigated	0.05	0.797	0.807	0.010
	CamidelsNerets	Cropland-rainfed	0.05	0.812	0.845	0.033
	ElBoixer	Grassland	0.05	0.724	0.763	0.039
	LosCoscolls	Cropland-rainfed	0.05	0.846	0.821	-0.025
	Pessonada	Cropland-rainfed	0.05	0.785	0.781	-0.004
	BatliliudeSort	Grassland	0.05	0.607	0.621	0.014
	ColldePaller	Cropland-rainfed	0.05	0.760	0.769	0.009
	LaCultiadAreu	Grassland	0.05	0.859	0.861	0.003
Average				0.773	0.778	0.005

Both DA experiments have yielded the same results for all sites as none of them belong to irrigated cropland grid-cells according to the CORINE land cover dataset. In general, temporal correlation with *in-situ* ranges from 0.607 to 0.859 for OL experiments. However, the lowest and highest temporal correlations with DA experiments are 0.621 and 0.869, respectively, indicating that the worst-performing sites exhibit better performance with DA. Out of 13 stations, only 4 stations show a reduction in terms of temporal correlation with DA compared to OL.

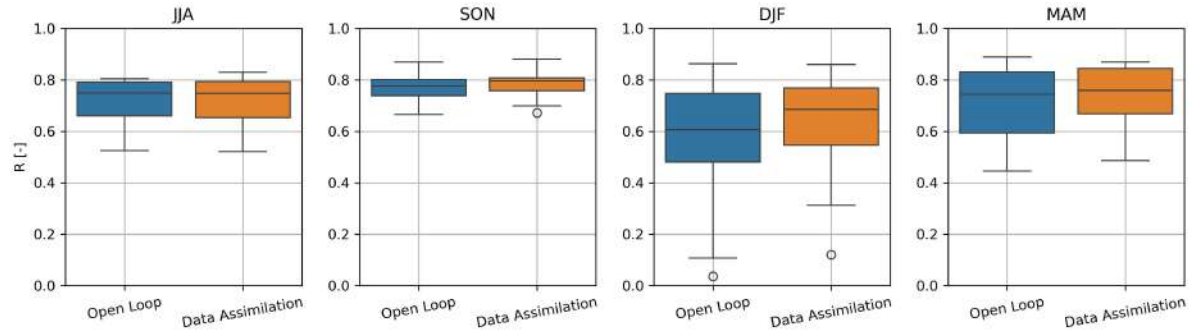


Figure 4.18: Temporal correlation between daily *in-situ* SM and GLEAM first layer SM.

Mean temporal correlation for all stations is 0.773 and 0.778 for OL and DA experiments, respectively. The mean increase in correlations is 0.005, which is lower than the results of Rains et al. (2022), who obtained a mean increase of 0.037 over 139 European SM sites.

Figure 4.18 presents the temporal correlation between daily *in-situ* SM measurements and different experiments of GLEAM. What is notable is that, OL experiment results shows that GLEAM performs relatively well in JJA, SON, and MAM compared to DJF months. It should be noted that GLEAM is run with 1km forcings, which may have led to the low representativeness of point-scale site measurements with respect to the observations and model estimates, which was also reported in the study of Rains et al. (2022).

5 Conclusion and future research perspectives

5.1 Conclusion

This study aimed to address the limitations of capturing the influence of irrigation on SM and E estimates through combining modeling and RS techniques. By setting two key objectives – enabling forward simulation of Sentinel-1 backscatter through coupling RTM, GLEAM, and LAI observations, and developing a DA method using WCM and EnKF – the study sought to generate high-resolution (1km) daily SM and E estimates including influence of irrigation over the Ebro Basin in Spain, thereby providing valuable insights for agricultural and water management applications.

The evaluation of two different strategies to calibrate the WCM revealed the importance of including vegetation information during this process. The results have shown that vegetation plays a crucial role in the scattering mechanism over cultivated and vegetated areas. Backscatter observations and simulations were compared, and the results showed overall satisfactory performance (mean $R = 0.616$ for DA-A and 0.618 for DA-B and mean RMSE = 0.621 dB for DA-A and 0.617 for DA-B), with the best performance found over rainfed croplands (mean $R = 0.65$, and mean RMSE = 0.77 dB). However, over irrigated areas, forward simulation with poorly calibrated WCM parameters (i.e., the calibration DA-A, which excluded the growing season) led to biased backscatter simulation outputs compared to WCM calibrated with all-year-round values over irrigated areas. Comparing the irrigated and rainfed croplands, the results demonstrated that the performance of forward simulations over rainfed croplands is slightly higher, as expected, due to the consideration discussed in Section 3.4.2, i.e., the importance of calibration of the forward operator with unbiased SM estimates and the satellite observations to realistically update SM estimates.

The forward simulations of Sentinel-1 were then used to update the GLEAM top layer SM to improve SM estimates and, through the propagation of the updated SM conditions, the E estimates. Total annual E estimates are shown to increase after the DA of Sentinel-1 for all land cover types. A detailed comparison between daily and seasonal DA impacts has highlighted the seasonal differences in potential E and how SM impacts E estimates. For the summer months, when evaporative demand is high, E estimates increase with DA as these months are characterized by limited water rather than limited energy. However, the DA impact on E is shown to be small during the other seasons.

The comparison of the two different calibration approaches tested in this study also revealed that biased backscatter simulations degrade the performance of the DA scheme over irrigated areas. It is expected that assimilating Sentinel-1 backscatter should increase SM values over irrigated areas as it includes irrigation-related information in its signal. The comparison between the two DA experiments has shown that during the growing season, increments for the DA-A case are smaller compared to those of DA-B, indicating that the expected benefit of excluding the growing season during the calibration of WCM is not realized. In the Ebro Basin, agricultural practices include crop rotation, which causes intra-annual variability in

the backscatter characteristics of specific grid-cells that have two growing seasons in a given year. Additionally, inter-annual crop rotations may occur due to economic and climatic factors specific to a certain year. Therefore, using a single set of WCM parameters for each grid-cell can lead to unrealistic observation forecasts and thus increments, ultimately degrading model performance. Nonetheless, comparing *in-situ* SM time series with modeled SM estimates has demonstrated that data assimilation of Sentinel-1 enhances SM estimates across various land cover types (average daily SM correlation $R = 0.778$) even though the overall improvement is small (mean $\Delta R = +0.005$). Lack of *in-situ* SM and E measurement over agricultural domains hindered the validation of the derived estimates, however the resulting 1km daily SM and E GLEAM dataset has the potential to be used for water and agricultural management applications.

5.2 Future research perspectives

For future research perspectives, several suggestions can be made. Firstly, investigating the DA experiment results more in-depth could reveal additional insights. For instance, a comparison with the previous study by Lievens et al. (2017a) in the context of observation forecast variability has shown that perturbations applied to forcings, observations, and state variables may dominate observation forecast variability. However, more in-depth analyses should be conducted to test this hypothesis. Additionally, determining whether the positive SM increments result from poor vegetation simulations or capturing the influence of irrigation on SM can provide more insight into the performance of the proposed DA scheme. Moreover, investigating the results based on not only land cover but also different regional characteristics (e.g., different climatic conditions, intensity of irrigation practiced) can provide a more comprehensive understanding of the performance of GLEAM and DA approaches. Moreover, the impact of pre-processing steps applied to Sentinel-1 backscatter observations, namely masking the pixels that have low correlation with ERA5-Land SM, might have also filtered out pixels that are heavily irrigated, given that ERA5-Land does not consider irrigation in its estimates. This step may have excluded some irrigation signals before the resampling to a 1km resolution.

Other possible improvements to account for irrigation in GLEAM SM and E can be considered. High-resolution SM retrieval products, such as SMAP DISPATCH (Ojha et al., 2021), SMOS DISPATCH (Merlin et al., 2013), SMAP/S-1 (Das et al., 2019), and Sentinel-1 RT1 (Quast et al., 2023), have shown the ability to capture irrigation in their retrievals (Dari et al., 2020, 2023; Jalilvand et al., 2021; Zappa et al., 2021, 2022) and can be assimilated with direct data assimilation of SM. Direct assimilation of retrievals can also reduce computational efforts compared to the EnKF approach, which may be more suitable for larger-scale applications.

Additionally, adding a simple irrigation module to GLEAM and re-calibrating the WCM using year-round backscatter data along with the OL run of GLEAM to obtain an unbiased system, in a manner similar to Modanesi et al. (2022), can be beneficial. Finally, using VOD as a vegetation descriptor in the WCM and jointly updating SM and VOD based on Sentinel-1 observations

can improve the vegetation backscatter component of the WCM, which has been shown to perform poorly in this study over vegetated areas. Additionally, the SM2RAIN algorithm that was already tested by Brocca et al. (2018) and Dari et al. (2023) to quantify irrigation amounts, can be integrated into GLEAM to deterministically derive irrigation amounts without the need to run GLEAM in ensemble mode.

References

- Abelen, S., & Seitz, F. (2013). Relating satellite gravimetry data to global soil moisture products via data harmonization and correlation analysis. *Remote Sensing of Environment*, 136, 89–98. <https://doi.org/10.1016/j.rse.2013.04.012>
- Ajjur, S. B., & Al-Ghamdi, S. G. (2021). Evapotranspiration and water availability response to climate change in the Middle East and North Africa. *Climatic Change*, 166(3), 28. <https://doi.org/10.1007/s10584-021-03122-z>
- Alday, J. G., Camarero, J. J., Revilla, J., & Resco De Dios, V. (2020). Similar diurnal, seasonal and annual rhythms in radial root expansion across two coexisting Mediterranean oak species (D. Epron, Ed.). *Tree Physiology*, 40(7), 956–968. <https://doi.org/10.1093/treephys/tpaa041>
- Alter, R. E., Im, E.-S., & Eltahir, E. A. B. (2015). Rainfall consistently enhanced around the Gezira Scheme in East Africa due to irrigation. *Nature Geoscience*, 8(10), 763–767. <https://doi.org/10.1038/ngeo2514>
- Ambrosone, M., Matese, A., Di Gennaro, S. F., Gioli, B., Tudoroiu, M., Genesio, L., Miglietta, F., Baronti, S., Maienza, A., Ungaro, F., & Toscano, P. (2020). Retrieving soil moisture in rainfed and irrigated fields using Sentinel-2 observations and a modified OPTRAM approach. *International Journal of Applied Earth Observation and Geoinformation*, 89, 102113. <https://doi.org/10.1016/j.jag.2020.102113>
- Arellano, C. M., Maralit, A. A., Paringit, E. C., Sarmiento, C. J., Faelga, R. A., Tandoc, F. A., Viñad, C., Lopez, R., & Pamittan, F. J. (2019). Multi-Temporal Analysis of Dense and Sparse Forest's Radar Backscatter Using Sentinel-1A Collection in Google Earth Engine. *The International Archives of the Photogrammetry, Remote Sensing and Spatial Information Sciences*, XLII-4/W19, 23–30. <https://doi.org/10.5194/isprs-archives-XLII-4-W19-23-2019>
- Arias Cuenca, M. (2023, April). *Sentinel-1 time series applications over agricultural fields: Proposal, evaluation and comparison of different methodologies* [Doctoral dissertation, Universidad Pública de Navarra]. Retrieved May 9, 2024, from <https://hdl.handle.net/2454/45156>
- Arino, O., Gross, D., Ranera, F., Leroy, M., Bicheron, P., Brockman, C., Defourny, P., Vancutsem, C., Achard, F., Durieux, L., Bourg, L., Latham, J., Di Gregorio, A., Witt, R., Herold, M., Sambale, J., Plummer, S., & Weber, J.-L. (2007). GlobCover: ESA service for global land cover from MERIS [ISSN: 2153-7003]. *2007 IEEE International Geoscience and Remote Sensing Symposium*, 2412–2415. <https://doi.org/10.1109/IGARSS.2007.4423328>
- Armstrong, R., Brodzik, M. J., Knowles, K., & Savoie, M. (2005). Global Monthly EASE-Grid Snow Water Equivalent Climatology, Version 1. <https://doi.org/10.5067/KJVERY3MIBPS>
- Attema, E. P. W., & Ulaby, F. T. (1978). Vegetation modeled as a water cloud. *Radio Science*, 13(2), 357–364. <https://doi.org/10.1029/RS013i002p00357>
- Babaeian, E., Sadeghi, M., Franz, T. E., Jones, S., & Tuller, M. (2018). Mapping soil moisture with the Optical TRapezoid Model (OPTRAM) based on long-term MODIS observations. *Remote Sensing of Environment*, 211, 425–440. <https://doi.org/10.1016/j.rse.2018.04.029>

- Bağçacı, S. Ç., Yucel, I., Duzenli, E., & Yilmaz, M. T. (2021). Intercomparison of the expected change in the temperature and the precipitation retrieved from CMIP6 and CMIP5 climate projections: A Mediterranean hot spot case, Turkey. *Atmospheric Research*, 256, 105576. <https://doi.org/10.1016/j.atmosres.2021.105576>
- Baghdadi, N., Zribi, M., Paloscia, S., Verhoest, N. E. C., Lievens, H., Baup, F., & Mattia, F. (2015). Semi-Empirical Calibration of the Integral Equation Model for Co-Polarized L-Band Backscattering. *Remote Sensing*, 7(10), 13626–13640. <https://doi.org/10.3390/rs71013626>
- Bahar, E. (1981). Scattering cross sections for composite random surfaces: Full wave analysis. *Radio Science*, 16(6), 1327–1335. <https://doi.org/10.1029/RS016i006p01327>
- Barriopedro, D., García-Herrera, R., Ordóñez, C., Miralles, D. G., & Salcedo-Sanz, S. (2023). Heat Waves: Physical Understanding and Scientific Challenges. *Reviews of Geophysics*, 61(2), e2022RG000780. <https://doi.org/10.1029/2022RG000780>
- Bartholomé, E., & Belward, A. S. (2005). GLC2000: A new approach to global land cover mapping from Earth observation data. *International Journal of Remote Sensing*, 26(9), 1959–1977. <https://doi.org/10.1080/01431160412331291297>
- Bauer-Marschallinger, B., Cao, S., Navacchi, C., Freeman, V., Reuß, F., Geudtner, D., Rommen, B., Vega, F. C., Snoeij, P., Attema, E., Reimer, C., & Wagner, W. (2021). The normalised Sentinel-1 Global Backscatter Model, mapping Earth's land surface with C-band microwaves. *Scientific Data*, 8(1), 277. <https://doi.org/10.1038/s41597-021-01059-7>
- Bauer-Marschallinger, B., Freeman, V., Cao, S., Paulik, C., Schaufler, S., Stachl, T., Modanesi, S., Massari, C., Ciabatta, L., Brocca, L., & Wagner, W. (2019). Toward Global Soil Moisture Monitoring With Sentinel-1: Harnessing Assets and Overcoming Obstacles. *IEEE Transactions on Geoscience and Remote Sensing*, 57(1), 520–539. <https://doi.org/10.1109/TGRS.2018.2858004>
- Bauer-Marschallinger, B., Sabel, D., & Wagner, W. (2014). Optimisation of global grids for high-resolution remote sensing data. *Computers & Geosciences*, 72, 84–93. <https://doi.org/10.1016/j.cageo.2014.07.005>
- Bechtold, M., Modanesi, S., Lievens, H., Baguis, P., Brangers, I., Carrassi, A., Getirana, A., Gruber, A., Heyvaert, Z., Massari, C., Scherrer, S., Vannitsem, S., & De Lannoy, G. (2023). Assimilation of Sentinel-1 Backscatter into a Land Surface Model with River Routing and Its Impact on Streamflow Simulations in Two Belgian Catchments. *Journal of Hydrometeorology*, 24(12), 2389–2408. <https://doi.org/10.1175/JHM-D-22-0198.1>
- Bowen, I. S. (1926). The Ratio of Heat Losses by Conduction and by Evaporation from any Water Surface. *Physical Review*, 27(6), 779–787. <https://doi.org/10.1103/PhysRev.27.779>
- Brocca, L., Ciabatta, L., Massari, C., Moramarco, T., Hahn, S., Hasenauer, S., Kidd, R., Dorigo, W., Wagner, W., & Levizzani, V. (2014). Soil as a natural rain gauge: Estimating global rainfall from satellite soil moisture data. *Journal of Geophysical Research: Atmospheres*, 119(9), 5128–5141. <https://doi.org/10.1002/2014JD021489>
- Brocca, L., Tarpanelli, A., Filippucci, P., Dorigo, W., Zaussinger, F., Gruber, A., & Fernández-Prieto, D. (2018). How much water is used for irrigation? A new approach exploiting coarse resolution satellite soil moisture products. *International Journal of Applied Earth Observation and Geoinformation*, 73, 752–766. <https://doi.org/10.1016/j.jag.2018.08.023>

- Brutsaert, W. (1982). *Evaporation into the Atmosphere*. Springer Netherlands. <https://doi.org/10.1007/978-94-017-1497-6>
- Chen, J., Cazenave, A., Dahle, C., Llovel, W., Panet, I., Pfeffer, J., & Moreira, L. (2022). Applications and Challenges of GRACE and GRACE Follow-On Satellite Gravimetry. *Surveys in Geophysics*, 43(1), 305–345. <https://doi.org/10.1007/s10712-021-09685-x>
- Cleugh, H. A., Leuning, R., Mu, Q., & Running, S. W. (2007). Regional evaporation estimates from flux tower and MODIS satellite data. *Remote Sensing of Environment*, 106(3), 285–304. <https://doi.org/10.1016/j.rse.2006.07.007>
- Coleman, T. F., & Li, Y. (1996). An Interior Trust Region Approach for Nonlinear Minimization Subject to Bounds. *SIAM Journal on Optimization*, 6(2), 418–445. <https://doi.org/10.1137/0806023>
- Comin, F. A. (1999). Management of The Ebro River Basin: Past, present and future. *Water Science and Technology*, 40(10). [https://doi.org/10.1016/S0273-1223\(99\)00672-1](https://doi.org/10.1016/S0273-1223(99)00672-1)
- Courtier, P., & Bouttier. (2002). Data Assimilation Concepts and Methods. <https://www.ecmwf.int/sites/default/files/elibrary/2002/16928-data-assimilation-concepts-and-methods.pdf>
- Dari, J., Brocca, L., Modanesi, S., Massari, C., Tarpanelli, A., Barbetta, S., Quast, R., Vreugdenhil, M., Freeman, V., Barella-Ortiz, A., Quintana-Seguí, P., Bretreger, D., & Volden, E. (2023). Regional data sets of high-resolution (1 and 6 km) irrigation estimates from space. *Earth System Science Data*, 15(4), 1555–1575. <https://doi.org/10.5194/essd-15-1555-2023>
- Dari, J., Brocca, L., Quintana-Seguí, P., Escorihuela, M. J., Stefan, V., & Morbidelli, R. (2020). Exploiting High-Resolution Remote Sensing Soil Moisture to Estimate Irrigation Water Amounts over a Mediterranean Region. *Remote Sensing*, 12(16), 2593. <https://doi.org/10.3390/rs12162593>
- Dari, J., Morbidelli, R., Quintana-Seguí, P., & Brocca, L. (2024). The Temporal-Stability-Based Irrigation MAPping (TSIMAP) Method: A Virtuous Trade-Off between Accuracy, Flexibility, and Facility for End-Users. *Water*, 16(5), 644. <https://doi.org/10.3390/w16050644>
- Dari, J., Quintana-Seguí, P., Morbidelli, R., Saltalippi, C., Flammini, A., Giugliarelli, E., Escorihuela, M. J., Stefan, V., & Brocca, L. (2022). Irrigation estimates from space: Implementation of different approaches to model the evapotranspiration contribution within a soil-moisture-based inversion algorithm. *Agricultural Water Management*, 265, 107537. <https://doi.org/10.1016/j.agwat.2022.107537>
- Das, N. N., Entekhabi, D., Dunbar, R. S., Chaubell, M. J., Colliander, A., Yueh, S., Jagdhuber, T., Chen, F., Crow, W., O'Neill, P. E., Walker, J. P., Berg, A., Bosch, D. D., Caldwell, T., Cosh, M. H., Collins, C. H., Lopez-Baeza, E., & Thibeault, M. (2019). The SMAP and Copernicus Sentinel 1A/B microwave active-passive high resolution surface soil moisture product. *Remote Sensing of Environment*, 233, 111380. <https://doi.org/10.1016/j.rse.2019.111380>
- De Lannoy, G. J. M., Bechtold, M., Albergel, C., Brocca, L., Calvet, J.-C., Carrassi, A., Crow, W. T., de Rosnay, P., Durand, M., Forman, B., Geppert, G., Giroto, M., Hendricks Franssen, H.-J., Jonas, T., Kumar, S., Lievens, H., Lu, Y., Massari, C., Pauwels, V. R. N., ... Steele-Dunne, S. (2022). Perspective on satellite-based land data assimilation to estimate water

- cycle components in an era of advanced data availability and model sophistication. *Frontiers in Water*, 4. <https://doi.org/10.3389/frwa.2022.981745>
- De Lannoy, G. J. M., Houser, P. R., Pauwels, V. R. N., & Verhoest, N. E. C. (2006). Assessment of model uncertainty for soil moisture through ensemble verification. *Journal of Geophysical Research: Atmospheres*, 111(D10), 2005JD006367. <https://doi.org/10.1029/2005JD006367>
- De Roo, R., Yang Du, Ulaby, F., & Dobson, M. (2001). A semi-empirical backscattering model at L-band and C-band for a soybean canopy with soil moisture inversion. *IEEE Transactions on Geoscience and Remote Sensing*, 39(4), 864–872. <https://doi.org/10.1109/36.917912>
- Deines, J. M., Kendall, A. D., Crowley, M. A., Rapp, J., Cardille, J. A., & Hyndman, D. W. (2019). Mapping three decades of annual irrigation across the US High Plains Aquifer using Landsat and Google Earth Engine. *Remote Sensing of Environment*, 233, 111400. <https://doi.org/10.1016/j.rse.2019.111400>
- de Jeu, R. (2013a). AMSR-E/Aqua surface soil moisture (LPRM) L2B V002. <https://doi.org/10.5067/WLVYB96A3GEA>
- de Jeu, R. (2013b). AMSR2/GCOM-W1 surface soil moisture (LPRM) L2B V001. <https://doi.org/10.5067/3P8SQ4KBWVFI>
- de Jeu, R. (2013c). TMI/TRMM surface soil moisture (LPRM) L2 V001. <https://doi.org/10.5067/DE73VGBNS01H>
- de Jeu, R. (2014). WindSat/Coriolis surface soil moisture (LPRM) L2 V001. <https://doi.org/10.5067/LITMC9T7LZSN>
- de Roos, S. (2023). *Assimilation of microwave backscatter data into a regional crop model: Estimating soil moisture and biomass over European croplands* [Doctoral dissertation, KU Leuven]. Retrieved February 28, 2024, from <https://lirias.kuleuven.be/4099406&lang=en>
- Dezsi, Ş., Mîndrescu, M., Petrea, D., Rai, P. K., Hamann, A., & Nistor, M.-M. (2018). High-resolution projections of evapotranspiration and water availability for Europe under climate change. *International Journal of Climatology*, 38(10), 3832–3841. <https://doi.org/10.1002/joc.5537>
- Dheeravath, V., Thenkabail, P. S., Chandrakantha, G., Noojipady, P., Reddy, G. P. O., Biradar, C. M., Gumma, M. K., & Velpuri, M. (2010). Irrigated areas of India derived using MODIS 500 m time series for the years 2001–2003. *ISPRS Journal of Photogrammetry and Remote Sensing*, 65(1), 42–59. <https://doi.org/10.1016/j.isprsjprs.2009.08.004>
- Diawara, A., Loustau, D., & Berbigier, P. (1991). Comparison of two methods for estimating the evaporation of a Pinus pinaster (Ait.) stand: Sap flow and energy balance with sensible heat flux measurements by an eddy covariance method. *Agricultural and Forest Meteorology*, 54(1), 49–66. [https://doi.org/10.1016/0168-1923\(91\)90040-W](https://doi.org/10.1016/0168-1923(91)90040-W)
- DiMiceli, C., Carroll, M., Sohlberg, R., Kim, D.-H., Kelly, M., & Townshend, J. (2015). MOD44B MODIS/Terra Vegetation Continuous Fields Yearly L3 Global 250m SIN Grid V006. <https://doi.org/10.5067/MODIS/MOD44B.006>

- Dorigo, W., Dietrich, S., Aires, F., Brocca, L., Carter, S., Cretaux, J.-F., Dunkerley, D., Enomoto, H., Forsberg, R., Güntner, A., Hegglin, M. I., Hollmann, R., Hurst, D. F., Johannessen, J. A., Kummerow, C., Lee, T., Luojus, K., Looser, U., Miralles, D. G., ... Aich, V. (2021a). Closing the Water Cycle from Observations across Scales: Where Do We Stand? *Bulletin of the American Meteorological Society*, 102(10), E1897–E1935. <https://doi.org/10.1175/BAMS-D-19-0316.1>
- Dorigo, W., Himmelbauer, I., Aberer, D., Schremmer, L., Petrakovic, I., Zappa, L., Preimesberger, W., Xaver, A., Annor, F., Ardö, J., Baldocchi, D., Bitelli, M., Blöschl, G., Bogen, H., Brocca, L., Calvet, J.-C., Camarero, J. J., Capello, G., Choi, M., ... Sabia, R. (2021b). The International Soil Moisture Network: Serving Earth system science for over a decade. *Hydrology and Earth System Sciences*, 25(11), 5749–5804. <https://doi.org/10.5194/hess-25-5749-2021>
- Dorigo, W., Wagner, W., Albergel, C., Albrecht, F., Balsamo, G., Brocca, L., Chung, D., Ertl, M., Forkel, M., Gruber, A., Haas, E., Hamer, P. D., Hirschi, M., Ikonen, J., de Jeu, R., Kidd, R., Lahoz, W., Liu, Y. Y., Miralles, D., ... Lecomte, P. (2017). ESA CCI Soil Moisture for improved Earth system understanding: State-of-the art and future directions. *Remote Sensing of Environment*, 203, 185–215. <https://doi.org/10.1016/j.rse.2017.07.001>
- Duarte, R., Pinilla, V., & Serrano, A. (2021). The globalization of Mediterranean agriculture: A long-term view of the impact on water consumption. *Ecological Economics*, 183, 106964. <https://doi.org/10.1016/j.ecolecon.2021.106964>
- Eaton, A. K., Rouse, W. R., Lafleur, P. M., Marsh, P., & Blanken, P. D. (2001). Surface Energy Balance of the Western and Central Canadian Subarctic: Variations in the Energy Balance among Five Major Terrain Types. *Journal of Climate*, 14(17), 3692–3703. [https://doi.org/10.1175/1520-0442\(2001\)014<3692:SEBOTW>2.0.CO;2](https://doi.org/10.1175/1520-0442(2001)014<3692:SEBOTW>2.0.CO;2)
- Elnashar, W., & Elyamany, A. (2023). Managing Risks of Climate Change on Irrigation Water in Arid Regions. *Water Resources Management*, 37(6), 2429–2446. <https://doi.org/10.1007/s11269-022-03267-1>
- ESA. (2022, August). Mission ends for Copernicus Sentinel-1B satellite. Retrieved May 15, 2024, from https://www.esa.int/Applications/Observing_the_Earth/Copernicus/Sentinel-1/Mission_ends_for_Copernicus_Sentinel-1B_satellite
- European Environment Agency & European Environment Agency. (2019). CORINE Land Cover 2018 (raster 100 m), Europe, 6-yearly - version 2020_20u1, May 2020. <https://doi.org/10.2909/960998C1-1870-4E82-8051-6485205EBBAC>
- European Space Agency. (1995). ERS-2 SCATTEROMETER Surface Soil Moisture Time Series and Orbit product in High and Nominal Resolution [SSM.H/N.TS - SSM.H/N]. <https://doi.org/10.57780/ERS-2607327>
- European Space Agency. (2009). SMOS L2 OS V700. <https://doi.org/10.57780/SM1-294CB1B>
- Evensen, G. (1994). Sequential data assimilation with a nonlinear quasi-geostrophic model using Monte Carlo methods to forecast error statistics. *Journal of Geophysical Research: Oceans*, 99(C5), 10143–10162. <https://doi.org/10.1029/94JC00572>
- Fader, M., Shi, S., Von Bloh, W., Bondeau, A., & Cramer, W. (2016). Mediterranean irrigation under climate change: More efficient irrigation needed to compensate for increases

- in irrigation water requirements. *Hydrology and Earth System Sciences*, 20(2), 953–973. <https://doi.org/10.5194/hess-20-953-2016>
- FAO. (2018a). Crop/Pasture Phenology: Growing Seasons (Global - 1Km). <https://data.apps.fao.org/catalog/dataset/3b298f15-b1db-4472-9584-10222a6c88ca>
- FAO. (2018b). *The future of food and agriculture – Alternative pathways to 2050. Summary Version*.
- FAO. (2022). *The State of the World's Land and Water Resources for Food and Agriculture 2021 – Systems at breaking point*. <https://doi.org/10.4060/cb9910en>
- FAO. (2023). *Land statistics and indicators 2000–2021*. <https://doi.org/10.4060/cc6907en>
- Fisher, J. B., Tu, K. P., & Baldocchi, D. D. (2008). Global estimates of the land–atmosphere water flux based on monthly AVHRR and ISLSCP-II data, validated at 16 FLUXNET sites. *Remote Sensing of Environment*, 112(3), 901–919. <https://doi.org/10.1016/j.rse.2007.06.025>
- Gardner, W. H. (2018, September). Water Content. In *Methods of Soil Analysis: Part 1 Physical and Mineralogical Methods* (pp. 493–544). Soil Science Society of America, American Society of Agronomy. <https://doi.org/10.2136/sssabookser5.1.2ed.c21>
- Gash, J. H. C. (1979). An analytical model of rainfall interception by forests. *Quarterly Journal of the Royal Meteorological Society*, 105(443), 43–55. <https://doi.org/10.1002/qj.49710544304>
- Gash, J. H. C., & Stewart, J. B. (1977). The evaporation from Thetford Forest during 1975. *Journal of Hydrology*, 35(3), 385–396. [https://doi.org/10.1016/0022-1694\(77\)90014-2](https://doi.org/10.1016/0022-1694(77)90014-2)
- Geng, H., Gwyn, Q. H. J., Brisco, B., Boisvert, J., & Brown, R. (1996). Mapping of Soil Moisture from C-Band Radar Images. *Canadian Journal of Remote Sensing*, 22(1), 117–126. <https://doi.org/10.1080/07038992.1996.10874642>
- Gentine, P., Green, J. K., Guérin, M., Humphrey, V., Seneviratne, S. I., Zhang, Y., & Zhou, S. (2019). Coupling between the terrestrial carbon and water cycles—a review. *Environmental Research Letters*, 14(8), 083003. <https://doi.org/10.1088/1748-9326/ab22d6>
- Global Modeling And Assimilation Office & Pawson, S. (2015). MERRA-2 tavg1_2d_slv_nx: 2d,1-Hourly,Time-Averaged,Single-Level,Assimilation,Single-Level Diagnostics V5.12.4. <https://doi.org/10.5067/VJAFPLI1CSIV>
- Gómez de Barreda, D., Pardo, G., Osca, J. M., Catala-Forner, M., Consola, S., Garnica, I., López-Martínez, N., Palmerín, J. A., & Osuna, M. D. (2021). An Overview of Rice Cultivation in Spain and the Management of Herbicide-Resistant Weeds. *Agronomy*, 11(6), 1095. <https://doi.org/10.3390/agronomy11061095>
- Gruber, A., Wagner, W., Hegyiova, A., Greifeneder, F., & Schlaffer, S. (2013). Potential of Sentinel-1 for high-resolution soil moisture monitoring. *2013 IEEE International Geoscience and Remote Sensing Symposium - IGARSS*, 4030–4033. <https://doi.org/10.1109/IGARSS.2013.6723717>
- Hoffman, R., Edwards, D., Wallin, G., & Burton, T. (1975). Remote sensing instrumentation and methods used for identifying center pivot sprinkler irrigation systems and estimating crop water use. *Proceedings of the international seminar and exposition on water resources instrumentation*.

- Holmes, T. R. (2019). Remote sensing techniques for estimating evaporation. In *Extreme Hydroclimatic Events and Multivariate Hazards in a Changing Environment* (pp. 129–143). Elsevier. <https://doi.org/10.1016/B978-0-12-814899-0.00005-5>
- Iglesias, A., Mougou, R., Moneo, M., & Quiroga, S. (2011). Towards adaptation of agriculture to climate change in the Mediterranean. *Regional Environmental Change*, 11(1), 159–166. <https://doi.org/10.1007/s10113-010-0187-4>
- IPCC. (2014). *Climate Change 2014: Impacts, Adaptation and Vulnerability: Working Group II Contribution to the IPCC Fifth Assessment Report of the Intergovernmental Panel on Climate Change* (V. R. Barros, C. B. Field, D. J. Dokken, M. D. Mastrandrea, & K. J. Mach, Eds.). Cambridge University Press. <https://doi.org/10.1017/CBO9781107415386>
- Jahromi, M. N., Miralles, D., Koppa, A., Rains, D., Zand-Parsa, S., Mosaffa, H., & Jamshidi, S. (2022). Ten Years of GLEAM: A Review of Scientific Advances and Applications. In O. Bozorg-Haddad & B. Zolghadr-Asli (Eds.), *Computational Intelligence for Water and Environmental Sciences* (pp. 525–540, Vol. 1043). Springer Nature Singapore. Retrieved May 9, 2024, from https://link.springer.com/10.1007/978-981-19-2519-1_25
- Jalilvand, E., Abolafia-Rosenzweig, R., Tajrishy, M., & Das, N. (2021). Evaluation of SMAP/Sentinel 1 High-Resolution Soil Moisture Data to Detect Irrigation Over Agricultural Domain. *IEEE Journal of Selected Topics in Applied Earth Observations and Remote Sensing*, 14, 10733–10747. <https://doi.org/10.1109/JSTARS.2021.3119228>
- Jalilvand, E., Tajrishy, M., Ghazi Zadeh Hashemi, S. A., & Brocca, L. (2019). Quantification of irrigation water using remote sensing of soil moisture in a semi-arid region. *Remote Sensing of Environment*, 231, 111226. <https://doi.org/10.1016/j.rse.2019.111226>
- Janjić, T., Bormann, N., Bocquet, M., Carton, J. A., Cohn, S. E., Dance, S. L., Losa, S. N., Nichols, N. K., Potthast, R., Waller, J. A., & Weston, P. (2018). On the representation error in data assimilation. *Quarterly Journal of the Royal Meteorological Society*, 144(713), 1257–1278. <https://doi.org/10.1002/qj.3130>
- Jeppesen, E., Beklioglu, M., Özkan, K., & Akyürek, Z. (2020). Salinization Increase due to Climate Change Will Have Substantial Negative Effects on Inland Waters: A Call for Multifaceted Research at the Local and Global Scale. *The Innovation*, 1(2). <https://doi.org/10.1016/j.xinn.2020.100030>
- Kalman, R. E. (1960). A New Approach to Linear Filtering and Prediction Problems. *Journal of Basic Engineering*, 82(1), 35–45. <https://doi.org/10.1115/1.3662552>
- Kelliher, F. M., Leuning, R., & Schulze, E. D. (1993). Evaporation and canopy characteristics of coniferous forests and grasslands. *Oecologia*, 95(2), 153–163. <https://doi.org/10.1007/BF00323485>
- Kerr, Y. H. (2007). Soil moisture from space: Where are we? *Hydrogeology Journal*, 15(1), 117–120. <https://doi.org/10.1007/s10040-006-0095-3>
- Kiehl, J. T., & Trenberth, K. E. (1997). Earth's Annual Global Mean Energy Budget. *Bulletin of the American Meteorological Society*, 78(2), 197–208. [https://doi.org/10.1175/1520-0477\(1997\)078<0197:EAGMEB>2.0.CO;2](https://doi.org/10.1175/1520-0477(1997)078<0197:EAGMEB>2.0.CO;2)

- Kim, S.-b., Zyl, J. v., Dunbar, S., Njoku, E., Johnson, J., Moghaddam, M., Shi, J., & Tsang, L. (2016). SMAP L2 Radar Half-Orbit 3 km EASE-Grid Soil Moisture, Version 3. <https://doi.org/10.5067/J8SGO1E0Y9XZ>
- Kodama, M., Kudo, S., & Kosuge, T. (1985). Application of Atmospheric Neutrons to Soil Moisture Measurement. *Soil Science*, 140(4), 237–242. <https://doi.org/10.1097/00010694-198510000-00001>
- Koppa, A., Rains, D., Hulsman, P., Poyatos, R., & Miralles, D. G. (2022). A deep learning-based hybrid model of global terrestrial evaporation. *Nature Communications*, 13(1), 1912. <https://doi.org/10.1038/s41467-022-29543-7>
- Koster, R. D., Sud, Y. C., Guo, Z., Dirmeyer, P. A., Bonan, G., Oleson, K. W., Chan, E., Verseghy, D., Cox, P., Davies, H., Kowalczyk, E., Gordon, C. T., Kanae, S., Lawrence, D., Liu, P., Mocko, D., Lu, C.-H., Mitchell, K., Malyshev, S., ... Xue, Y. (2006). GLACE: The Global Land–Atmosphere Coupling Experiment. Part I: Overview. *Journal of Hydrometeorology*, 7(4), 590–610. <https://doi.org/10.1175/JHM510.1>
- Kumar, S. V., Peters-Lidard, C. D., Santanello, J. A., Reichle, R. H., Draper, C. S., Koster, R. D., Nearing, G., & Jasinski, M. F. (2015). Evaluating the utility of satellite soil moisture retrievals over irrigated areas and the ability of land data assimilation methods to correct for unmodeled processes. *Hydrology and Earth System Sciences*, 19(11), 4463–4478. <https://doi.org/10.5194/hess-19-4463-2015>
- Lahoz, W. A., & De Lannoy, G. J. M. (2014). Closing the Gaps in Our Knowledge of the Hydrological Cycle over Land: Conceptual Problems. *Surveys in Geophysics*, 35(3), 623–660. <https://doi.org/10.1007/s10712-013-9221-7>
- Lahoz, W. A., & Schneider, P. (2014). Data assimilation: Making sense of Earth Observation. *Frontiers in Environmental Science*, 2. <https://doi.org/10.3389/fenvs.2014.00016>
- Lawrence, D. M., Fisher, R. A., Koven, C. D., Oleson, K. W., Swenson, S. C., Bonan, G., Collier, N., Ghimire, B., van Kampenhout, L., Kennedy, D., Kluzek, E., Lawrence, P. J., Li, F., Li, H., Lombardozzi, D., Riley, W. J., Sacks, W. J., Shi, M., Vertenstein, M., ... Zeng, X. (2019). The Community Land Model Version 5: Description of New Features, Benchmarking, and Impact of Forcing Uncertainty. *Journal of Advances in Modeling Earth Systems*, 11(12), 4245–4287. <https://doi.org/10.1029/2018MS001583>
- Lawston, P. M., Santanello Jr, J. A., & Kumar, S. V. (2017). Irrigation Signals Detected From SMAP Soil Moisture Retrievals. *Geophysical Research Letters*, 44(23), 11, 860–11, 867. <https://doi.org/10.1002/2017GL075733>
- Li, B. (2018). GLDAS Catchment Land Surface Model L4 daily 0.25 x 0.25 degree, Version 2.0. <https://doi.org/10.5067/LYHA9088MFWQ>
- Li, Z.-L., Leng, P., Zhou, C., Chen, K.-S., Zhou, F.-C., & Shang, G.-F. (2021). Soil moisture retrieval from remote sensing measurements: Current knowledge and directions for the future. *Earth-Science Reviews*, 218, 103673. <https://doi.org/10.1016/j.earscirev.2021.103673>
- Lievens, H., Martens, B., Verhoest, N., Hahn, S., Reichle, R., & Miralles, D. (2017a). Assimilation of global radar backscatter and radiometer brightness temperature observations to

- improve soil moisture and land evaporation estimates. *Remote Sensing of Environment*, 189, 194–210. <https://doi.org/10.1016/j.rse.2016.11.022>
- Lievens, H., Reichle, R. H., Liu, Q., De Lannoy, G. J. M., Dunbar, R. S., Kim, S. B., Das, N. N., Cosh, M., Walker, J. P., & Wagner, W. (2017b). Joint Sentinel-1 and SMAP data assimilation to improve soil moisture estimates. *Geophysical Research Letters*, 44(12), 6145–6153. <https://doi.org/10.1002/2017GL073904>
- Lievens, H., Demuzere, M., Marshall, H.-P., Reichle, R. H., Brucker, L., Brangers, I., De Rosnay, P., Dumont, M., Girotto, M., Immerzeel, W. W., Jonas, T., Kim, E. J., Koch, I., Marty, C., Saloranta, T., Schöber, J., & De Lannoy, G. J. M. (2019). Snow depth variability in the Northern Hemisphere mountains observed from space. *Nature Communications*, 10(1), 4629. <https://doi.org/10.1038/s41467-019-12566-y>
- Liu, C., & Shi, J. (2016). Estimation of Vegetation Parameters of Water Cloud Model for Global Soil Moisture Retrieval Using Time-Series L-Band Aquarius Observations. *IEEE Journal of Selected Topics in Applied Earth Observations and Remote Sensing*, 9(12), 5621–5633. <https://doi.org/10.1109/JSTARS.2016.2596541>
- Liu, Y., & Gupta, H. V. (2007). Uncertainty in hydrologic modeling: Toward an integrated data assimilation framework. *Water Resources Research*, 43(7). <https://doi.org/10.1029/2006WR005756>
- López-Moreno, J. I., Vicente-Serrano, S. M., Moran-Tejeda, E., Zabalza, J., Lorenzo-Lacruz, J., & García-Ruiz, J. M. (2011). Impact of climate evolution and land use changes on water yield in the ebro basin. *Hydrology and Earth System Sciences*, 15(1), 311–322. <https://doi.org/10.5194/hess-15-311-2011>
- Loveland, T. R., Reed, B. C., Brown, J. F., Ohlen, D. O., Zhu, Z., Yang, L., & Merchant, J. W. (2000). Development of a global land cover characteristics database and IGBP DISCover from 1 km AVHRR data. *International Journal of Remote Sensing*, 21(6-7), 1303–1330. <https://doi.org/10.1080/014311600210191>
- Luoju, K., Pulliainen, J., Takala, M., Lemmetyinen, J., Kangwa, M., Smolander, T., & Derksen, C. (2013). *Global snow monitoring for climate research: Algorithm theoretical basis document (ATBD) - SWE-algorithm* (tech. rep. No. 1.0).
- Mach, D. M., Christian, H. J., Blakeslee, R. J., Boccippio, D. J., Goodman, S. J., & Boeck, W. L. (2007). Performance assessment of the Optical Transient Detector and Lightning Imaging Sensor. *Journal of Geophysical Research: Atmospheres*, 112(D9). <https://doi.org/10.1029/2006JD007787>
- Mane, S., Das, N., Singh, G., Cosh, M., & Dong, Y. (2024). Advancements in dielectric soil moisture sensor Calibration: A comprehensive review of methods and techniques. *Computers and Electronics in Agriculture*, 218, 108686. <https://doi.org/10.1016/j.compag.2024.108686>
- Martens, B., Miralles, D., Lievens, H., Fernández-Prieto, D., & Verhoest, N. (2016). Improving terrestrial evaporation estimates over continental Australia through assimilation of SMOS soil moisture. *International Journal of Applied Earth Observation and Geoinformation*, 48, 146–162. <https://doi.org/10.1016/j.jag.2015.09.012>

- Martens, B., De Jeu, R., Verhoest, N., Schuurmans, H., Kleijer, J., & Miralles, D. (2018a). Towards Estimating Land Evaporation at Field Scales Using GLEAM. *Remote Sensing*, 10(11), 1720. <https://doi.org/10.3390/rs10111720>
- Martens, B., Miralles, D. G., Lievens, H., van der Schalie, R., de Jeu, R. A. M., Fernández-Prieto, D., Beck, H. E., Dorigo, W. A., & Verhoest, N. E. C. (2017). GLEAM v3: Satellite-based land evaporation and root-zone soil moisture. *Geoscientific Model Development*, 10(5), 1903–1925. <https://doi.org/10.5194/gmd-10-1903-2017>
- Martens, B., Waegeman, W., Dorigo, W. A., Verhoest, N. E. C., & Miralles, D. G. (2018b). Terrestrial evaporation response to modes of climate variability. *npj Climate and Atmospheric Science*, 1(1), 1–7. <https://doi.org/10.1038/s41612-018-0053-5>
- Massari, C., Modanesi, S., Dari, J., Gruber, A., De Lannoy, G. J. M., Girotto, M., Quintana-Seguí, P., Le Page, M., Jarlan, L., Zribi, M., Ouaadi, N., Vreugdenhil, M., Zappa, L., Dorigo, W., Wagner, W., Brombacher, J., Pelgrum, H., Jaquot, P., Freeman, V., ... Brocca, L. (2021). A Review of Irrigation Information Retrievals from Space and Their Utility for Users. *Remote Sensing*, 13(20), 4112. <https://doi.org/10.3390/rs13204112>
- Mattia, F., Le Toan, T., Picard, G., Posa, F., D'Alessio, A., Notarnicola, C., Gatti, A., Rinaldi, M., Satalino, G., & Pasquariello, G. (2003). Multitemporal C-band radar measurements on wheat fields. *IEEE Transactions on Geoscience and Remote Sensing*, 41(7), 1551–1560. <https://doi.org/10.1109/TGRS.2003.813531>
- McCabe, M. F., Aragon, B., Houborg, R., & Mascaro, J. (2017). CubeSats in Hydrology: Ultrahigh-Resolution Insights Into Vegetation Dynamics and Terrestrial Evaporation. *Water Resources Research*, 53(12), 10017–10024. <https://doi.org/10.1002/2017WR022240>
- McCabe, M. F., Miralles, D. G., Holmes, T. R. H., & Fisher, J. B. (2019). Advances in the Remote Sensing of Terrestrial Evaporation. *Remote Sensing*, 11(9), 1138. <https://doi.org/10.3390/rs11091138>
- McDermid, S., Nocco, M., Lawston-Parker, P., Keune, J., Pokhrel, Y., Jain, M., Jägermeyr, J., Brocca, L., Massari, C., Jones, A. D., Vahmani, P., Thiery, W., Yao, Y., Bell, A., Chen, L., Dorigo, W., Hanasaki, N., Jasechko, S., Lo, M.-H., ... Yokohata, T. (2023). Irrigation in the Earth system. *Nature Reviews Earth & Environment*, 4(7), 435–453. <https://doi.org/10.1038/s43017-023-00438-5>
- McNaughton, K. G., & Black, T. A. (1973). A study of evapotranspiration from a Douglas fir forest using the energy balance approach. *Water Resources Research*, 9(6), 1579–1590. <https://doi.org/10.1029/WR009i006p01579>
- Meesters, A., De Jeu, R., & Owe, M. (2005). Analytical derivation of the vegetation optical depth from the microwave polarization difference index. *IEEE Geoscience and Remote Sensing Letters*, 2(2), 121–123. <https://doi.org/10.1109/LGRS.2005.843983>
- Merlin, O., Walker, J., Chehbouni, A., & Kerr, Y. (2008). Towards deterministic downscaling of SMOS soil moisture using MODIS derived soil evaporative efficiency. *Remote Sensing of Environment*, 112(10), 3935–3946. <https://doi.org/10.1016/j.rse.2008.06.012>
- Merlin, O., Escorihuela, M. J., Mayoral, M. A., Hagolle, O., Al Bitar, A., & Kerr, Y. (2013). Self-calibrated evaporation-based disaggregation of SMOS soil moisture: An evaluation

- study at 3 km and 100 m resolution in Catalunya, Spain. *Remote Sensing of Environment*, 130, 25–38. <https://doi.org/10.1016/j.rse.2012.11.008>
- Miralles, D. G., Brutsaert, W., Dolman, A. J., & Gash, J. H. (2020). On the Use of the Term “Evapotranspiration”. *Water Resources Research*, 56(11), e2020WR028055. <https://doi.org/10.1029/2020WR028055>
- Miralles, D. G., Holmes, T. R. H., De Jeu, R. a. M., Gash, J. H., Meesters, A. G. C. A., & Dolman, A. J. (2011). Global land-surface evaporation estimated from satellite-based observations. *Hydrology and Earth System Sciences*, 15(2), 453–469. <https://doi.org/10.5194/hess-15-453-2011>
- Miralles, D. G., Jiménez, C., Jung, M., Michel, D., Ershadi, A., McCabe, M. F., Hirschi, M., Martens, B., Dolman, A. J., Fisher, J. B., Mu, Q., Seneviratne, S. I., Wood, E. F., & Fernández-Prieto, D. (2016). The WACMOS-ET project – Part 2: Evaluation of global terrestrial evaporation data sets. *Hydrology and Earth System Sciences*, 20(2), 823–842. <https://doi.org/10.5194/hess-20-823-2016>
- Miralles, D. G., Gash, J. H., Holmes, T. R. H., De Jeu, R. A. M., & Dolman, A. J. (2010). Global canopy interception from satellite observations. *Journal of Geophysical Research: Atmospheres*, 115(D16), 2009JD013530. <https://doi.org/10.1029/2009JD013530>
- Miralles, D. G., Teuling, A. J., van Heerwaarden, C. C., & Vilà-Guerau de Arellano, J. (2014). Mega-heatwave temperatures due to combined soil desiccation and atmospheric heat accumulation. *Nature Geoscience*, 7(5), 345–349. <https://doi.org/10.1038/ngeo2141>
- Miranda, N., Torres, R., Geudtner, D., Pinheiro, M., Potin, P., Gratadour, J.-B., O’Connell, A., Bibby, D., Navas-Traver, I., & Cossu, M. (2023). Sentinel-1 First Generation Status, Past and Future. *IGARSS 2023 - 2023 IEEE International Geoscience and Remote Sensing Symposium*, 4560–4563. <https://doi.org/10.1109/IGARSS52108.2023.10281990>
- Mo, T., Choudhury, B. J., Schmugge, T. J., Wang, J. R., & Jackson, T. J. (1982). A model for microwave emission from vegetation-covered fields. *Journal of Geophysical Research: Oceans*, 87(C13), 11229–11237. <https://doi.org/10.1029/JC087iC13p11229>
- Modanesi, S., Massari, C., Bechtold, M., Lievens, H., Tarpanelli, A., Brocca, L., Zappa, L., & De Lannoy, G. J. M. (2022). Challenges and benefits of quantifying irrigation through the assimilation of Sentinel-1 backscatter observations into Noah-MP. *Hydrology and Earth System Sciences*, 26(18), 4685–4706. <https://doi.org/10.5194/hess-26-4685-2022>
- Modanesi, S., Massari, C., Gruber, A., Lievens, H., Tarpanelli, A., Morbidelli, R., & De Lannoy, G. J. M. (2021). Optimizing a backscatter forward operator using Sentinel-1 data over irrigated land. *Hydrology and Earth System Sciences*, 25(12), 6283–6307. <https://doi.org/10.5194/hess-25-6283-2021>
- Monteith, J. L. (1965). Evaporation and environment. *Symposia of the Society for Experimental Biology*, 19, 205–234. Retrieved May 30, 2024, from <https://repository.rothamsted.ac.uk/item/8v5v7/evaporation-and-environment>
- Morrison, K., & Wagner, W. (2020). Explaining Anomalies in SAR and Scatterometer Soil Moisture Retrievals From Dry Soils With Subsurface Scattering. *IEEE Transactions on Geoscience and Remote Sensing*, 58(3), 2190–2197. <https://doi.org/10.1109/TGRS.2019.2954771>

- Mu, Q., Heinsch, F. A., Zhao, M., & Running, S. W. (2007). Development of a global evapotranspiration algorithm based on MODIS and global meteorology data. *Remote Sensing of Environment*, 111(4), 519–536. <https://doi.org/10.1016/j.rse.2007.04.015>
- Mu, Q., Zhao, M., & Running, S. W. (2011). Improvements to a MODIS global terrestrial evapotranspiration algorithm. *Remote Sensing of Environment*, 115(8), 1781–1800. <https://doi.org/10.1016/j.rse.2011.02.019>
- Mu, Q., Zhao, M., & Running, S. W. (2013, November). *MODIS Global Terrestrial Evapotranspiration (ET) Product (NASA MOD16A2/A3) Algorithm Theoretical Basis Document* (tech. rep. No. 5). NASA Headquarters. https://lpdaac.usgs.gov/documents/93/MOD16_ATBD.pdf
- Muñoz Sabater, J. (2019). ERA5-Land monthly averaged data from 1950 to present. <https://doi.org/10.24381/CDS.68D2BB30>
- Myneni, R., Knyazikhin, Y., & Park, T. (2021). MODIS/Terra+Aqua Leaf Area Index/FPAR 4-Day L4 Global 500m SIN Grid V061. <https://doi.org/10.5067/MODIS/MCD15A3H.061>
- Niu, G.-Y., Yang, Z.-L., Mitchell, K. E., Chen, F., Ek, M. B., Barlage, M., Kumar, A., Manning, K., Niyogi, D., Rosero, E., Tewari, M., & Xia, Y. (2011). The community Noah land surface model with multiparameterization options (Noah-MP): 1. Model description and evaluation with local-scale measurements. *Journal of Geophysical Research*, 116(D12), D12109. <https://doi.org/10.1029/2010JD015139>
- OECD. (2015, September). *Drying Wells, Rising Stakes: Towards Sustainable Agricultural Groundwater Use*. <https://doi.org/10.1787/9789264238701-en>
- Oh, Y., Sarabandi, K., & Ulaby, F. (1992). An empirical model and an inversion technique for radar scattering from bare soil surfaces. *IEEE Transactions on Geoscience and Remote Sensing*, 30(2), 370–381. <https://doi.org/10.1109/36.134086>
- Ojha, N., Merlin, O., Suere, C., & Escorihuela, M. J. (2021). Extending the Spatio-Temporal Applicability of DISPATCH Soil Moisture Downscaling Algorithm: A Study Case Using SMAP, MODIS and Sentinel-3 Data. *Frontiers in Environmental Science*, 9. <https://doi.org/10.3389/fenvs.2021.555216>
- ONEill, P. E., Chan, S., Njoku, E., Jackson, T., Bindlish, R., & Chaubell, M. (2023). SMAP L2 Radiometer Half-Orbit 36 km EASE-Grid Soil Moisture, Version 9. <https://doi.org/10.5067/K7Y2D8QQVZ4L>
- ONEill, P. E., Chan, S., Njoku, E. G., & Jackson, T. (2016). SMAP Enhanced L3 Radiometer Global Daily 9 km EASE-Grid Soil Moisture, Version 1. <https://doi.org/10.5067/ZRO7EXJ8O3XI>
- Ouaadi, N., Jarlan, L., Khabba, S., Ezzahar, J., Le Page, M., & Merlin, O. (2021). Irrigation Amounts and Timing Retrieval through Data Assimilation of Surface Soil Moisture into the FAO-56 Approach in the South Mediterranean Region. *Remote Sensing*, 13(14), 2667. <https://doi.org/10.3390/rs13142667>
- Owe, M., De Jeu, R., & Walker, J. (2001). A methodology for surface soil moisture and vegetation optical depth retrieval using the microwave polarization difference index. *IEEE Transactions on Geoscience and Remote Sensing*, 39(8), 1643–1654. <https://doi.org/10.1109/36.942542>

- Ozdogan, M., Rodell, M., Beaudoin, H. K., & Toll, D. L. (2010a). Simulating the Effects of Irrigation over the United States in a Land Surface Model Based on Satellite-Derived Agricultural Data. *Journal of Hydrometeorology*, 11(1), 171–184. <https://doi.org/10.1175/2009JHM1116.1>
- Ozdogan, M., Yang, Y., Allez, G., & Cervantes, C. (2010b). Remote Sensing of Irrigated Agriculture: Opportunities and Challenges. *Remote Sensing*, 2(9), 2274–2304. <https://doi.org/10.3390/rs2092274>
- Park, S.-E., Jung, Y. T., Cho, J.-H., Moon, H., & Han, S.-h. (2019). Theoretical Evaluation of Water Cloud Model Vegetation Parameters. *Remote Sensing*, 11(8), 894. <https://doi.org/10.3390/rs11080894>
- Pastorello, G., Trotta, C., Canfora, E., Chu, H., Christianson, D., Cheah, Y.-W., Poindexter, C., Chen, J., Elbashandy, A., Humphrey, M., Isaac, P., Polidori, D., Reichstein, M., Ribeca, A., Van Ingen, C., Vuichard, N., Zhang, L., Amiro, B., Ammann, C., ... Papale, D. (2020). The FLUXNET2015 dataset and the ONEFlux processing pipeline for eddy covariance data. *Scientific Data*, 7(1), 225. <https://doi.org/10.1038/s41597-020-0534-3>
- Peng, J., Albergel, C., Balenzano, A., Brocca, L., Cartus, O., Cosh, M. H., Crow, W. T., Dabrowska-Zielinska, K., Dadson, S., Davidson, M. W., De Rosnay, P., Dorigo, W., Gruber, A., Hagemann, S., Hirschi, M., Kerr, Y. H., Lovergine, F., Mahecha, M. D., Marzahn, P., ... Loew, A. (2021). A roadmap for high-resolution satellite soil moisture applications – confronting product characteristics with user requirements. *Remote Sensing of Environment*, 252, 112162. <https://doi.org/10.1016/j.rse.2020.112162>
- Piecuch, J., & Paluch, Ł. (2016). Importance of Agriculture Within the Structure of Employment and Production in the Mediterranean Countries. *Journal of Agribusiness and Rural Development*, 10(1). <https://doi.org/10.17306/JARD.2016.19>
- Priestley, C. H. B., & Taylor, R. J. (1972). On the Assessment of Surface Heat Flux and Evaporation Using Large-Scale Parameters. *Monthly Weather Review*, 100(2), 81–92. [https://doi.org/10.1175/1520-0493\(1972\)100<0081:OTAOSH>2.3.CO;2](https://doi.org/10.1175/1520-0493(1972)100<0081:OTAOSH>2.3.CO;2)
- Qing, Y., Wang, S., Yang, Z.-L., & Gentine, P. (2023). Soil moisture–atmosphere feedbacks have triggered the shifts from drought to pluvial conditions since 1980. *Communications Earth & Environment*, 4(1), 1–10. <https://doi.org/10.1038/s43247-023-00922-2>
- Quast, R., Albergel, C., Calvet, J.-C., & Wagner, W. (2019). A Generic First-Order Radiative Transfer Modelling Approach for the Inversion of Soil and Vegetation Parameters from Scatterometer Observations. *Remote Sensing*, 11(3), 285. <https://doi.org/10.3390/rs11030285>
- Quast, R., Wagner, W., Bauer-Marschallinger, B., & Vreugdenhil, M. (2023). Soil moisture retrieval from Sentinel-1 using a first-order radiative transfer model—A case-study over the Po-Valley. *Remote Sensing of Environment*, 295, 113651. <https://doi.org/10.1016/j.rse.2023.113651>
- Quesada, B., Vautard, R., Yiou, P., Hirschi, M., & Seneviratne, S. I. (2012). Asymmetric European summer heat predictability from wet and dry southern winters and springs. *Nature Climate Change*, 2(10), 736–741. <https://doi.org/10.1038/nclimate1536>

- Rains, D., De Lannoy, G. J. M., Lievens, H., Walker, J. P., & Verhoest, N. E. C. (2018). SMOS and SMAP Brightness Temperature Assimilation Over the Murrumbidgee Basin. *IEEE Geoscience and Remote Sensing Letters*, 15(11), 1652–1656. <https://doi.org/10.1109/LGRS.2018.2855188>
- Rains, D., Lievens, H., De Lannoy, G. J. M., McCabe, M. F., De Jeu, R. A. M., & Miralles, D. G. (2022). Sentinel-1 Backscatter Assimilation Using Support Vector Regression or the Water Cloud Model at European Soil Moisture Sites. *IEEE Geoscience and Remote Sensing Letters*, 19, 1–5. <https://doi.org/10.1109/LGRS.2021.3073484>
- Rains, D., Trigo, I., Dutra, E., Ermida, S., Ghent, D., Hulsman, P., Gómez-Dans, J., & Miralles, D. G. (2024). High-resolution (1 km) all-sky net radiation over Europe enabled by the merging of land surface temperature retrievals from geostationary and polar-orbiting satellites. *Earth System Science Data*, 16(1), 567–593. <https://doi.org/10.5194/essd-16-567-2024>
- Raml, B., Vreugdenhil, M., Massart, S. J. A., Navacchi, C., & Wagner, W. (2023). Enabling global scale Sentinel-1 time series analysis through streaming. <https://doi.org/10.34726/5308>
- Rawat, K. S., Singh, S. K., Ray, R. L., & Szabo, S. (2022). Parameterization of the modified water cloud model (MWCM) using normalized difference vegetation index (NDVI) for winter wheat crop: A case study from Punjab, India. *Geocarto International*, 37(6), 1560–1573. <https://doi.org/10.1080/10106049.2020.1783579>
- Reichle, R. H. (2008). Data assimilation methods in the Earth sciences. *Advances in Water Resources*, 31(11), 1411–1418. <https://doi.org/10.1016/j.advwatres.2008.01.001>
- Reichle, R. H., McLaughlin, D. B., & Entekhabi, D. (2002). Hydrologic Data Assimilation with the Ensemble Kalman Filter. *Monthly Weather Review*, 130(1), 103–114. [https://doi.org/10.1175/1520-0493\(2002\)130<0103:HDAWTE>2.0.CO;2](https://doi.org/10.1175/1520-0493(2002)130<0103:HDAWTE>2.0.CO;2)
- Ryu, D., Crow, W. T., Zhan, X., & Jackson, T. J. (2009). Correcting Unintended Perturbation Biases in Hydrologic Data Assimilation. *Journal of Hydrometeorology*, 10(3), 734–750. <https://doi.org/10.1175/2008JHM1038.1>
- Sadeghi, M., Babaeian, E., Tuller, M., & Jones, S. B. (2017). The optical trapezoid model: A novel approach to remote sensing of soil moisture applied to Sentinel-2 and Landsat-8 observations. *Remote Sensing of Environment*, 198, 52–68. <https://doi.org/10.1016/j.rse.2017.05.041>
- Savenije, H. H. G. (2004). The importance of interception and why we should delete the term evapotranspiration from our vocabulary. *Hydrological Processes*, 18(8), 1507–1511. <https://doi.org/10.1002/hyp.5563>
- Schmugge, T. (1978). Remote Sensing of Surface Soil Moisture. *Journal of Applied Meteorology and Climatology*, 17(10), 1549–1557. [https://doi.org/10.1175/1520-0450\(1978\)017<1549:RSOSSM>2.0.CO;2](https://doi.org/10.1175/1520-0450(1978)017<1549:RSOSSM>2.0.CO;2)
- Schmugge, T., Gloersen, P., Wilheit, T., & Geiger, F. (1974). Remote sensing of soil moisture with microwave radiometers. *Journal of Geophysical Research*, 79(2), 317–323. <https://doi.org/10.1029/JB079i002p00317>

- Schmugge, T., Wang, J., & Asrar, G. (1988). Results from the Push Broom Microwave Radiometer flights over the Konza Prairie in 1985. *IEEE Transactions on Geoscience and Remote Sensing*, 26(5), 590–596. <https://doi.org/10.1109/36.7684>
- Seneviratne, S. I., Lüthi, D., Litschi, M., & Schär, C. (2006). Land–atmosphere coupling and climate change in Europe. *Nature*, 443(7108), 205–209. <https://doi.org/10.1038/nature05095>
- Shiklomanov, I. A. (1998). World Water Resources: A New Appraisal and Assessment for the 21st Century. Retrieved May 10, 2024, from <https://www.caee.utexas.edu/prof/mckinney/ce385d/papers/Shiklomanov.pdf>
- Shukla, J., & Mintz, Y. (1982). Influence of Land-Surface Evapotranspiration on the Earth's Climate. *Science*, 215(4539), 1498–1501. <https://doi.org/10.1126/science.215.4539.1498>
- Shuttleworth, W. J. (1984). Observations of radiation exchange above and below Amazonian forest. *Quarterly Journal of the Royal Meteorological Society*, 110(466), 1163–1169. <https://doi.org/10.1002/qj.49711046623>
- Shuttleworth, W. J., & Calder, I. R. (1979). Has the Priestley-Taylor Equation Any Relevance to Forest Evaporation? *Journal of Applied Meteorology and Climatology*, 18(5), 639–646. [https://doi.org/10.1175/1520-0450\(1979\)018<0639:HTPTEA>2.0.CO;2](https://doi.org/10.1175/1520-0450(1979)018<0639:HTPTEA>2.0.CO;2)
- Simons, G., Koster, R., & Droogers, P. (2020). *HiHydroSoil v2.0 - A high resolution soil map of global hydraulic properties* (tech. rep. No. 134). Wageningen, The Netherlands.
- Smith, A. B., Walker, J. P., Western, A. W., Young, R. I., Ellett, K. M., Pipunic, R. C., Grayson, R. B., Siriwardena, L., Chiew, F. H. S., & Richter, H. (2012). The Murrumbidgee soil moisture monitoring network data set. *Water Resources Research*, 48(7), 2012WR011976. <https://doi.org/10.1029/2012WR011976>
- Steduto, P., Hsiao, T. C., Raes, D., & Fereres, E. (2009). AquaCrop—The FAO Crop Model to Simulate Yield Response to Water: I. Concepts and Underlying Principles. *Agronomy Journal*, 101(3), 426–437. <https://doi.org/10.2134/agronj2008.0139s>
- Swinbank, W. C. (1951). The Measurement of Vertical Transfer of Heat and Water Vapor by Eddies in the Lower Atmosphere. *Journal of Meteorology*, 8(3), 135–145. [https://doi.org/10.1175/1520-0469\(1951\)008<0135:TMOVTO>2.0.CO;2](https://doi.org/10.1175/1520-0469(1951)008<0135:TMOVTO>2.0.CO;2)
- Tang, Q., Gao, H., Lu, H., & Lettenmaier, D. P. (2009). Remote sensing: Hydrology. *Progress in Physical Geography: Earth and Environment*, 33(4), 490–509. <https://doi.org/10.1177/0309133309346650>
- Teuling, A. J., Seneviratne, S. I., Stöckli, R., Reichstein, M., Moors, E., Ciais, P., Luyssaert, S., van den Hurk, B., Ammann, C., Bernhofer, C., Dellwik, E., Gianelle, D., Gielen, B., Grünwald, T., Klumpp, K., Montagnani, L., Moureaux, C., Sottocornola, M., & Wohlfahrt, G. (2010). Contrasting response of European forest and grassland energy exchange to heatwaves. *Nature Geoscience*, 3(10), 722–727. <https://doi.org/10.1038/ngeo950>
- Thenkabail, P. S., Schull, M., & Turrall, H. (2005). Ganges and Indus river basin land use/land cover (LULC) and irrigated area mapping using continuous streams of MODIS data. *Remote Sensing of Environment*, 95(3), 317–341. <https://doi.org/10.1016/j.rse.2004.12.018>

- Thornthwaite, C. W. (1948). An Approach Toward a Rational Classification of Climate. *Soil Science*, 66(1), 77. Retrieved May 29, 2024, from https://journals.lww.com/soilsci/Citation/1948/07000/An_Approach_Toward_a_Rational_Classification_of.7.aspx
- Tilman, D., Cassman, K. G., Matson, P. A., Naylor, R., & Polasky, S. (2002). Agricultural sustainability and intensive production practices. *Nature*, 418(6898), 671–677. <https://doi.org/10.1038/nature01014>
- Toca, L., Morrison, K., Artz, R., Gimona, A., & Quaife, T. (2022). High resolution C-band SAR backscatter response to peatland water table depth and soil moisture: A laboratory experiment. *International Journal of Remote Sensing*, 43(14), 5231–5251. <https://doi.org/10.1080/01431161.2022.2131478>
- Twele, A., Cao, W., Plank, S., & Martinis, S. (2016). Sentinel-1-based flood mapping: A fully automated processing chain. *International Journal of Remote Sensing*, 37(13), 2990–3004. <https://doi.org/10.1080/01431161.2016.1192304>
- Uddin, K., Matin, M. A., & Meyer, F. J. (2019). Operational Flood Mapping Using Multi-Temporal Sentinel-1 SAR Images: A Case Study from Bangladesh. *Remote Sensing*, 11(13), 1581. <https://doi.org/10.3390/rs11131581>
- Ulaby, F. (1974). Radar measurement of soil moisture content. *IEEE Transactions on Antennas and Propagation*, 22(2), 257–265. <https://doi.org/10.1109/TAP.1974.1140761>
- Ulaby, F. T., Batlivala, P. P., & Dobson, M. C. (1978). Microwave Backscatter Dependence on Surface Roughness, Soil Moisture, and Soil Texture: Part I-Bare Soil. *IEEE Transactions on Geoscience Electronics*, 16(4), 286–295. <https://doi.org/10.1109/TGE.1978.294586>
- United Nations. (2022, August). *World Population Prospects 2022: Summary of Results*. <https://doi.org/10.18356/9789210014380>
- Veloso, A., Mermoz, S., Bouvet, A., Le Toan, T., Planells, M., Dejoux, J.-F., & Ceschia, E. (2017). Understanding the temporal behavior of crops using Sentinel-1 and Sentinel-2-like data for agricultural applications. *Remote Sensing of Environment*, 199, 415–426. <https://doi.org/10.1016/j.rse.2017.07.015>
- Vicente-Serrano, S. M., & López-Moreno, J. I. (2006). The influence of atmospheric circulation at different spatial scales on winter drought variability through a semi-arid climatic gradient in Northeast Spain. *International Journal of Climatology*, 26(11), 1427–1453. <https://doi.org/10.1002/joc.1387>
- Viswanadham, Y., Silva Filho, V. P., & André, R. G. B. (1991). The Priestley-Taylor parameter-alpha for the Amazon forest. *Forest Ecology and Management*, 38(3), 211–225. [https://doi.org/10.1016/0378-1127\(91\)90143-J](https://doi.org/10.1016/0378-1127(91)90143-J)
- Wada, Y., Wisser, D., & Bierkens, M. F. P. (2014). Global modeling of withdrawal, allocation and consumptive use of surface water and groundwater resources. *Earth System Dynamics*, 5(1), 15–40. <https://doi.org/10.5194/esd-5-15-2014>
- Wagner, W., Sabel, D., Doubkova, M., Bartsch, A., & Pathe, C. (2009). The Potential of Sentinel-1 for Monitoring Soil Moisture with a High Spatial Resolution at Global Scale. 674, 64. Retrieved May 9, 2024, from <https://ui.adsabs.harvard.edu/abs/2009ESASP.674E..64W>
- Wagner, W., Hahn, S., Kidd, R., Melzer, T., Bartalis, Z., Hasenauer, S., Figa-Saldaña, J., De Rosnay, P., Jann, A., Schneider, S., Komma, J., Kubu, G., Brugger, K., Aubrecht, C., Züger,

- J., Gangkofner, U., Kienberger, S., Brocca, L., Wang, Y., ... Steinnocher, K. (2013). The ASCAT Soil Moisture Product: A Review of its Specifications, Validation Results, and Emerging Applications. *Meteorologische Zeitschrift*, 22(1), 5–33. <https://doi.org/10.1127/0941-2948/2013/0399>
- Wagner, W., Lemoine, G., & Rott, H. (1999). A Method for Estimating Soil Moisture from ERS Scatterometer and Soil Data. *Remote Sensing of Environment*, 70(2), 191–207. [https://doi.org/10.1016/S0034-4257\(99\)00036-X](https://doi.org/10.1016/S0034-4257(99)00036-X)
- Wagner, W., Lindorfer, R., Melzer, T., Hahn, S., Bauer-Marschallinger, B., Morrison, K., Calvet, J.-C., Hobbs, S., Quast, R., Greimeister-Pfeil, I., & Vreugdenhil, M. (2022). Widespread occurrence of anomalous C-band backscatter signals in arid environments caused by subsurface scattering. *Remote Sensing of Environment*, 276, 113025. <https://doi.org/10.1016/j.rse.2022.113025>
- Wagner, W., Pathe, C., Doubkova, M., Sabel, D., Bartsch, A., Hasenauer, S., Blöschl, G., Scipal, K., Martínez-Fernández, J., & Löw, A. (2008). Temporal Stability of Soil Moisture and Radar Backscatter Observed by the Advanced Synthetic Aperture Radar (ASAR). *Sensors*, 8(2), 1174–1197. <https://doi.org/10.3390/s80201174>
- Xie, Y., Gibbs, H. K., & Lark, T. J. (2021). Landsat-based Irrigation Dataset (LANID): 30-m resolution maps of irrigation distribution, frequency, and change for the US, 1997–2017. *Earth System Science Data*, 13(12), 5689–5710. <https://doi.org/10.5194/essd-13-5689-2021>
- Xie, Y., & Lark, T. J. (2021). Mapping annual irrigation from Landsat imagery and environmental variables across the conterminous United States. *Remote Sensing of Environment*, 260, 112445. <https://doi.org/10.1016/j.rse.2021.112445>
- Yadav, V. P., Prasad, R., Bala, R., & Vishwakarma, A. k. (2019). Estimation of soil moisture through water cloud model using sentinel -1A SAR data [ISSN: 2153-7003]. *IGARSS 2019 - 2019 IEEE International Geoscience and Remote Sensing Symposium*, 6961–6964. <https://doi.org/10.1109/IGARSS.2019.8900203>
- Yang, Y. (2019). Remotely Sensed Evapotranspiration. In X. Li & H. Vereecken (Eds.), *Observation and Measurement of Ecohydrological Processes* (pp. 155–200, Vol. 2). Springer Berlin Heidelberg. Retrieved May 9, 2024, from http://link.springer.com/10.1007/978-3-662-48297-1_6
- Yilmaz, G., Çolak, M. A., Özgencil, İ. K., Metin, M., Korkmaz, M., Ertuğrul, S., Soyluer, M., Bucak, T., Tavşanoğlu, Ü. N., Özkan, K., Akyürek, Z., Beklioğlu, M., & Jeppesen, E. (2021). Decadal changes in size, salinity, waterbirds, and fish in lakes of the Konya Closed Basin, Turkey, associated with climate change and increasing water abstraction for agriculture. *Inland Waters*. Retrieved May 10, 2024, from <https://www.tandfonline.com/doi/abs/10.1080/20442041.2021.1924034>
- Zachariadis, T. (2016). *Climate change in Cyprus*. Springer Berlin Heidelberg. <https://doi.org/10.1007/978-3-319-29688-3>
- Zappa, L., Schlaffer, S., Bauer-Marschallinger, B., Nendel, C., Zimmerman, B., & Dorigo, W. (2021). Detection and Quantification of Irrigation Water Amounts at 500 m Using Sentinel-1 Surface Soil Moisture. *Remote Sensing*, 13(9), 1727. <https://doi.org/10.3390/rs13091727>

- Zappa, L., Schlaffer, S., Brocca, L., Vreugdenhil, M., Nendel, C., & Dorigo, W. (2022). How accurately can we retrieve irrigation timing and water amounts from (satellite) soil moisture? *International Journal of Applied Earth Observation and Geoinformation*, 113, 102979. <https://doi.org/10.1016/j.jag.2022.102979>
- Zaussinger, F., Dorigo, W., Gruber, A., Tarpanelli, A., Filippucci, P., & Brocca, L. (2019). Estimating irrigation water use over the contiguous United States by combining satellite and reanalysis soil moisture data. *Hydrology and Earth System Sciences*, 23(2), 897–923. <https://doi.org/10.5194/hess-23-897-2019>
- Zhang, K., Li, X., Zheng, D., Zhang, L., & Zhu, G. (2022). Estimation of Global Irrigation Water Use by the Integration of Multiple Satellite Observations. *Water Resources Research*, 58(3), e2021WR030031. <https://doi.org/10.1029/2021WR030031>
- Zhao, Q., Xie, Q., Peng, X., Lai, K., Wang, J., Fu, H., Zhu, J., & Song, Y. (2024). Understanding the Temporal Dynamics of Coherence and Backscattering Using Sentinel-1 Imagery for Crop-Type Mapping. *IEEE Journal of Selected Topics in Applied Earth Observations and Remote Sensing*, 17, 6875–6893. <https://doi.org/10.1109/JSTARS.2024.3373489>
- Zreda, M., Shuttleworth, W. J., Zeng, X., Zweck, C., Desilets, D., Franz, T., & Rosolem, R. (2012). COSMOS: The COsmic-ray Soil Moisture Observing System. *Hydrology and Earth System Sciences*, 16(11), 4079–4099. <https://doi.org/10.5194/hess-16-4079-2012>

A Appendix A: An example time series from a forest grid-cell

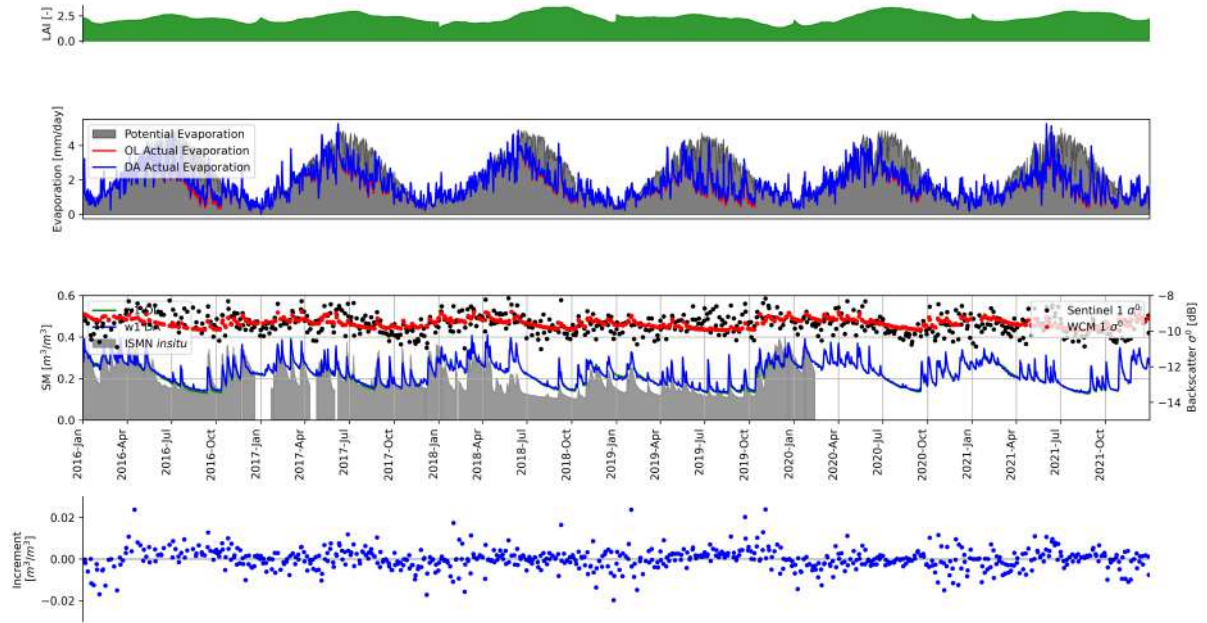


Figure A.1: Example time series (2016–2021) from a forest grid-cell. (top) LAI observations, (middle) OL and DA SM and daily E estimates as well as the the simulated and observed backscatter, (bottom) daily SM increments to the GLEAM top layer soil moisture. Selected grid-cell longitude: -0.81 latitude: 42.32. WCM Parameters: A=0.00, B=0.00, C=-10.52 dB, D=4.286 dB/m³m⁻³.

B Appendix B: Anomalies of DA-A with respect to OL run

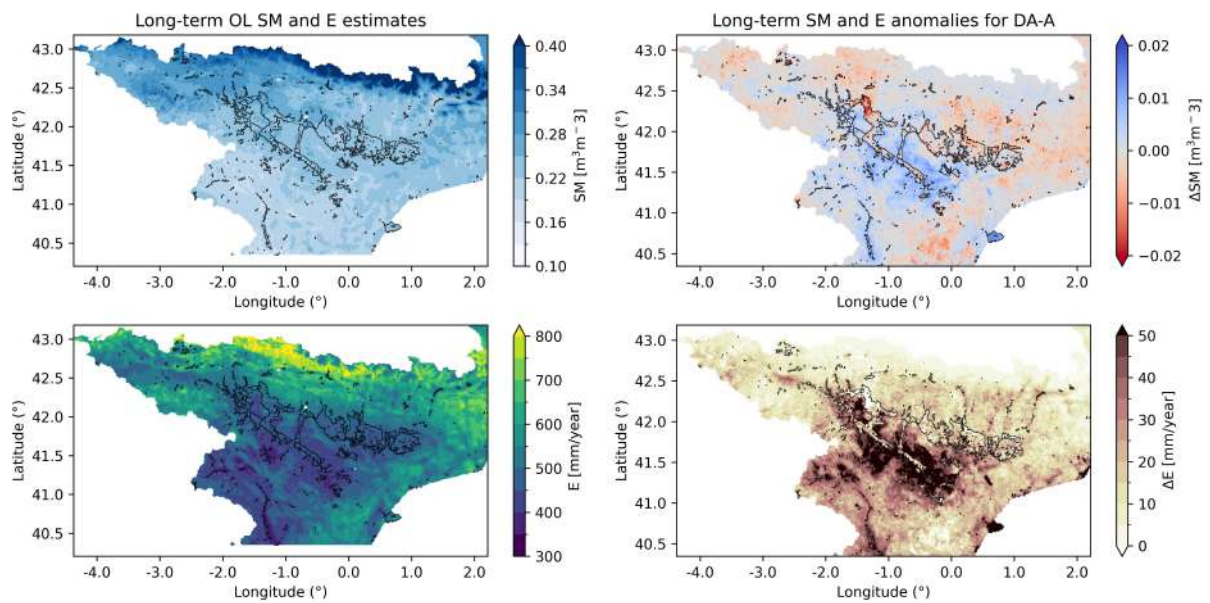


Figure B.1: (left) Long-term (2016–2021) mean SM and total annual E estimates over the Ebro Basin from GLEAM OL run, (right) long-term (2016–2021) anomalies of DA-A with respect to OL run. Irrigated areas are highlighted.